



## 저작자표시-비영리-변경금지 2.0 대한민국

이용자는 아래의 조건을 따르는 경우에 한하여 자유롭게

- 이 저작물을 복제, 배포, 전송, 전시, 공연 및 방송할 수 있습니다.

다음과 같은 조건을 따라야 합니다:



저작자표시. 귀하는 원저작자를 표시하여야 합니다.



비영리. 귀하는 이 저작물을 영리 목적으로 이용할 수 없습니다.



변경금지. 귀하는 이 저작물을 개작, 변형 또는 가공할 수 없습니다.

- 귀하는, 이 저작물의 재이용이나 배포의 경우, 이 저작물에 적용된 이용허락조건을 명확하게 나타내어야 합니다.
- 저작권자로부터 별도의 허가를 받으면 이러한 조건들은 적용되지 않습니다.

저작권법에 따른 이용자의 권리는 위의 내용에 의하여 영향을 받지 않습니다.

이것은 [이용허락규약\(Legal Code\)](#)을 이해하기 쉽게 요약한 것입니다.

[Disclaimer](#)

이학박사 학위논문

# Observations of the Near-Infrared Extragalactic Background Light

적외선 우주배경복사 관측연구

2017년 2월

서울대학교 대학원  
물리·천문학부 천문학 전공  
김 민 규



# Observations of the Near-Infrared Extragalactic Background Light

by

Min Gyu Kim  
(mgkim@astro.snu.ac.kr)

A dissertation submitted in partial fulfillment of the requirements for  
the degree of

**Doctor of Philosophy**

in

Astronomy

in

Astronomy Program, Department of Physics and Astronomy  
Seoul National University

Committee:

Professor      Myung Gyoon Lee

Professor      Hyung Mok Lee

Professor      Myungshin Im

Doctor          Woong-Seob Jeong

Doctor          Matsumoto Toshio



사랑하는 부모님께

*To my beloved parents*



# ABSTRACT

The Near-Infrared Extragalactic Background Light (NIREBL) is the integrated electromagnetic radiation over the entire cosmic history. Thus, the origin of NIREBL is an essential key to probe the formation and evolution of galaxies from the birth to present Universe. However, current technology limits us to resolve diffuse, faint, and distant objects contributing to the NIREBL brightness. We instead focus on the spatial fluctuation and spectra of the diffuse background over wide range of angular scales and wavelengths based on the data obtained by Cosmic Infrared Background ExpeRiment (CIBER) and InfraRed Telescope in Space (IRTS) to understand its nature and origin.

The CIBER is a sounding rocket mounting the spectrometers and Imagers inside a payload to study the NIREBL in both ways. By recovering the payload after each flight, it flew four times in different seasons to eliminate the issue on the strong Zodiacal Light (ZL) scattered from Interplanetary Dust Particle (IPD), where the brightness varies as Earth revolves around the Sun. Furthermore, it enable us to check any systematic errors between flights.

Using the Low Resolution Spectrometer (LRS) on the CIBER, we firstly measure the significant excess brightness at around  $1\ \mu\text{m}$  that cannot be explained with known foregrounds such as ZL, Integrated Star Light (ISL), and Diffuse Galactic Light (DGL). It connects previous measurements well towards longer wavelength ( $1.4 \sim 4.0\ \mu\text{m}$ ) and shorter wavelength ( $0.3, 0.555, 0.814\ \mu\text{m}$ ). The overall NIREBL spectrum decreases slowly towards shorter wavelength and rather rapidly towards longer wavelength with peak at  $\sim 1.5\ \mu\text{m}$ . It shows bluer than the ZL spectrum that rejects controversy in subtraction error of ZL.

While carrying out the data analysis, we found that the flux calibration performed in the laboratory for the 4th flight was contaminated by unknown reason.



We, therefore, used calibration result from the 3rd flight for the 4th flight data calibration assuming they were not changed. To validate the assumption, we examine the CIBER/LRS observed bright stars ( $J_m < 11$ ). By matching with 2MASS point source catalog, we identified 38 (2nd flight), 30 (3rd flight) and 42 (4th flight) number of bright stars. We found the flux correlation between the LRS and the 2MASS stars shows close to the unity regardless of flight number which validates our assumptions. Furthermore, one star is serendipitously observed twice from the 2nd and 4th flights. The observed stellar spectra from different flights show consistency within errors which ensures the 4th flight result.

On the other hand, fluctuations using the CIBER I- and H-band Imagers out to  $\sim 1^\circ$  were measured. The fluctuation spectra show excess ( $l < 5000$  or  $\theta > 4.3'$ ) and blue-like spectra approximately following the Rayleigh-Jeans. Three popular candidates based on the well established models are used to explain excess fluctuation. They are Direct Collapse Black Hole (DCBH), First stars, and Intra Halo Light (IHL). Nevertheless, they show different colors and amplitudes with CIBER excess and suggest necessity of new model to explain the excess fluctuation.

We notice that the CIBER fluctuation spectra still increases out to  $\sim 1^\circ$ . The excess at largest angular scale is initially interpreted as DGL without explicit measurement. Using AKARI/FIS data achieving high spatial resolution and deep pointing observation at  $90\ \mu\text{m}$ , we measure the DGL at relatively high cirrus region. The DGL fluctuation spectrum shows turnover at  $\sim 0.4^\circ$  and decreases towards large angular scales, which probes that the DGL is not the source of large angular scale. Motivated by this, we examine the power spectra above  $1^\circ$  using the IRTS which is the Japanese space infrared telescope achieved the widest sky coverage with high sensitivity. For the first time, we measure the largest angular scale power spectrum in the range  $2^\circ < \theta < 10^\circ$  for H- and K-band. Both bands show significant excess fluctuations with peak at  $\sim 1^\circ$ . The CIBER and the IRTS fluctuation spectra con-

nects well at common H-band although no measurement exists at  $\sim 1^\circ$ . To confirm the IRTS K-band result, we scaled the CIBER H-band assuming it follows Rayleigh-Jeans. Other previous measurements such as AKARI ( $2.4\ \mu\text{m}$ ), and Spitzer ( $3.6\ \mu\text{m}$ ) were also scaled in the same manner and compared. Although they are not clearly matched as H-band, we found that the K-band also shows bump at  $\sim 1^\circ$  and declines out to  $20^\circ$  which cannot be explained by currently proposed candidates and suggests necessity of new populations.

**Keywords:** cosmic background radiation — infrared: diffuse background — techniques: spectroscopic

***Student Number:*** 2011-30127



# Contents

<b>Abstract</b>	<b>i</b>
<b>List of Figures</b>	<b>x</b>
<b>List of Tables</b>	<b>xi</b>
<b>1 Introduction</b>	<b>1</b>
1.1 Extragalactic Background Light . . . . .	2
1.1.1 Cosmic backgrounds . . . . .	2
1.1.2 NIREBL detection methods . . . . .	6
1.2 Previous Studies . . . . .	7
1.2.1 NIREBL . . . . .	7
1.2.2 NIREBL candidates . . . . .	10
1.3 The purpose of this study . . . . .	15
<b>2 CIBER experiments and results</b>	<b>17</b>
2.1 Overview . . . . .	17
2.2 Instruments . . . . .	18
2.2.1 Imagers . . . . .	20
2.2.2 LRS . . . . .	21
2.2.3 NBS . . . . .	21

2.3	Laboratory experiments . . . . .	24
2.3.1	Calibration . . . . .	24
2.3.2	Flat field . . . . .	25
2.3.3	Focus test . . . . .	26
2.3.4	Stray light test . . . . .	27
2.4	Field selection . . . . .	29
2.5	Flight performance . . . . .	33
2.6	In-flight calibration from stars . . . . .	33
2.6.1	Background subtraction . . . . .	33
2.6.2	Astrometry . . . . .	37
2.6.3	Star identification . . . . .	38
2.6.4	Result and discussion . . . . .	42
2.7	Absolute brightness measurement . . . . .	45
2.7.1	LRS data analysis . . . . .	45
2.7.2	Result and discussion . . . . .	47
2.8	New insights from fluctuation measurements of the CIBER . . . . .	49
<b>3</b>	<b>Large angular scale fluctuations with IRTS data</b>	<b>57</b>
3.1	Overview . . . . .	57
3.2	IRTS instruments . . . . .	58
3.3	Observation and data reduction . . . . .	60
3.4	Data analysis . . . . .	61
3.4.1	NIRS data analysis . . . . .	62
3.4.2	Foregrounds estimation . . . . .	62
3.5	Power spectrum analysis at large angular scale . . . . .	70
3.6	Result and discussion . . . . .	75
<b>4</b>	<b>Summary and conclusions</b>	<b>83</b>

References	89
A Reflectivity measurements	95
요 약	99



# List of Figures

1.1	EBL intensities for all electromagnetic wavelengths. . . . .	4
1.2	EBL intensities for near-IR and far-IR. . . . .	5
1.3	EBL intensities for near-IR. . . . .	11
1.4	Fluctuation spectra measured from previous studies. . . . .	12
2.1	The CIBER payload and installed telescopes. . . . .	19
2.2	Optical crosssectional schematic and photograph of the Imager . . .	20
2.3	Optical crosssectional schematic and photograph of the LRS . . . .	22
2.4	Optical crosssectional schematic and photograph of the NBS . . . .	23
2.5	Schematic plot for the focus test . . . . .	28
2.6	Stray light of the CIBER/Imager. . . . .	30
2.7	An example CIBER/LRS image towards NEP field . . . . .	35
2.8	Flow chart of the background image construction . . . . .	36
2.9	The 2MASS J- and H-band fluxes as a function of the LRS bands. .	38
2.10	The LRS J-H color comparison with cross-matched 2MASS J-H color.	39
2.11	Flux ratios of all LRS stars to the matched 2MASS stars in J-band.	43
2.12	Flux ratios of all LRS stars to the matched 2MASS stars in H-band.	44
2.13	Five stars are serendipitously observed in two independent flights. Each panel shows two spectra extracted from each flight. Detailed information of each star is in Table 3 from Kim et al. (2017). . . .	46



2.14	Schematic diagram of multisampling . . . . .	48
2.15	The NIREBL spectra for the CIBER/LRS . . . . .	50
2.16	The CIBER auto- and cross- spectra with Spitzer 3.6 $\mu\text{m}$ . . . . .	52
2.17	Intensities of excess fluctuation . . . . .	53
2.18	AKARI/FIS deep pointing image at 90 $\mu\text{m}$ toward NEP field . . . . .	54
2.19	The CIBER H-band and DGL fluctuation spectra . . . . .	55
3.1	NIRS optical path . . . . .	59
3.2	IRTS observation . . . . .	61
3.3	Histogram of the NIRS pixel numbers used for each HEALPix pixel bin	63
3.4	DGL spectrum. . . . .	66
3.5	Limiting magnitudes for the 24 NIRS bands. . . . .	68
3.6	Beam transfer function of the NIRS PSF . . . . .	73
3.7	The measured foregrounds auto spectra for the NIRS . . . . .	74
3.8	H-band fluctuation errors . . . . .	76
3.9	K-band fluctuation errors . . . . .	77
3.10	The measured H-band auto spectrum for the IRTS/NIRS . . . . .	78
3.11	The measured K-band auto spectra for the IRTS/NIRS . . . . .	79
3.12	The NIRS cross spectrum . . . . .	81
3.13	The correlation diagram between the H- and K-band NIREBL surface brightness . . . . .	82
4.1	Spacecrafts for the NIREBL study . . . . .	88
A.1	Reflectance measurements of various kinds black materials . . . . .	98

# List of Tables

2.1	Coordinates and launch information of the observed fields . . . . .	32
3.1	DGL scaling factor . . . . .	67



# Chapter 1

## Introduction

The ancient people watched the stars in the night sky. They could see the Sun, the Moon, and stars shining in the universe. They tried to understand how the universe looks like. In 1610, Galileo Galilei found that the Milkyway is a composition of a large number of stars like the Sun using his own made refracting telescope. Two centuries after, William Herschel found the Uranus using reflecting telescope and extended the knowledge of the solar system. He also observed thousands of nebulae and star clusters. They debated whether the nebulae are a part or outside of our galaxy. The debate had ended since Edwin Hubble found that the Andromeda is another galaxy outside of the Milkyway in 1924. This discovery extended their knowledge on the universe that the universe is composed of a large number of galaxies.

Not only extended their knowledge into distances, they extended their views into invisible light. In 1800, William Herschel found the temperature increment of thermometer beyond the red-end of the prism when he observe the Sun. The invisible light, named infrared, has same characteristics as visible light such as reflection, transmission, and absorption. After that, they tried to observe astronomical objects in infrared. Nevertheless, the infrared astronomy did not receive much attention until Penzias and Wilson discovered Cosmic Microwave Background (CMB) using

radio telescope in 1964. The accidental discovery of CMB had recognized astronomer to explore infrared as well as other wavelengths, which associate with structure formation and evolution after the last scattering at  $z \sim 1100$ .

Now, astronomers observe the universe resolving more distance and faint objects in various wavelengths. They found the infrared also has unresolved diffuse backgrounds analogous to the CMB but has different physical mechanism. It shows excess brightness and fluctuation over the integrated light of galaxies from deep pointing observations. The origin of it is proposed by Jim Peebles that the first objects formed at early universe can be observed as background radiation. Several decades after the beginning of the infrared astronomy, we still have no clear explanation for the excess brightness. The EBL study will give us insights into galaxy formation and evolution from the early universe to the present complex structure. This dissertation is motivated by the discovery of excess emission in near-IR. Based on the EBL detections in unexplored wavelengths and angular scales, we constrain the energy needed for the EBL candidate sources and suggest necessity of new populations.

## 1.1 Extragalactic Background Light

### 1.1.1 Cosmic backgrounds

All electromagnetic radiation ranges from  $\gamma$ -ray to radio emits background in the universe. Depending on the physical properties of astronomical objects, their contributions on wavelengths are different although they show isotropic and homogeneous according to the cosmological principle. Figure 1.1 shows the brightness of extragalactic backgrounds over whole wavelength ranges. They are  $\gamma$ -ray, X-ray, ultraviolet (UV), optical, IR, microwaves, and radio in the order of frequency. UV and radio background measurements is challenging due to high-galactic background.  $\gamma$ -ray background is from the unresolved Active Galactic Nucleis (AGNs; Abdo et

al. 2010), star forming galaxies, Gamma Ray Bursts (GRBs), millisecond pulsars (Siegal-Gaskins et al. 2010), and dark matter annihilation. X-ray background is composed of AGNs hosting Super Massive Black Hole (SMBH; Hasinger 2004), undetected highly absorbed AGNs, massive X-ray binaries, supernova remnants, and hot gas in galaxy clusters. The CMB is the most energetic of all. It is the relic radiation of last scattering when the matter-radiation was decoupled. The redshifted radiation shows blackbody at 2.726 K with small anisotropies which evolves to the complex universe we see today.

In infrared, the EBL is divided into two sub-categories: near-IR and far-IR. The EBL observation in mid-IR is limited due to the strong Zodiacal Light (ZL) foregrounds. They are extended from 0.1 to 1000  $\mu\text{m}$  with two peaks at 1 and 250  $\mu\text{m}$  (Dole et al. 2006; see Figure 1.2). First peak is produced by nuclear processes such as nucleosynthesis in the stars, matter accretion onto the black hole while the second peak is from stellar light absorbed and re-emitted by dust inside galaxies. The figure shows the detailed EBL spectrum. Thanks to the deep sky observation with high spatial resolution telescope,  $\sim 90\%$  of far-IR background is detected as galaxy based on the stacking method (Viero et al. 2015). Residual emissions are thought to be as Dust Obscured Galaxies (DOGs), pure starburst, AGNs, Quasar, or Ultraluminous Infrared Galaxy (ULIRG) at high redshift ( $z > 1$ ). On the other hand, we found there remains unexplainable residual brightness coming from all parts of the sky like CMB. The excess brightness is a factor of 2 to 8 times brighter than the Integrated Galaxy Light (IGL) which achieved extremely deep measurements by JHKs  $\sim 28$  AB magnitude (Keenan et al. 2010). Throughout this dissertation, we review studies on the EBL to constrain energies of candidate sources and we use the term *Near-Infrared Extragalactic Background Light (NIREBL)* to indicate the near-IR EBL.

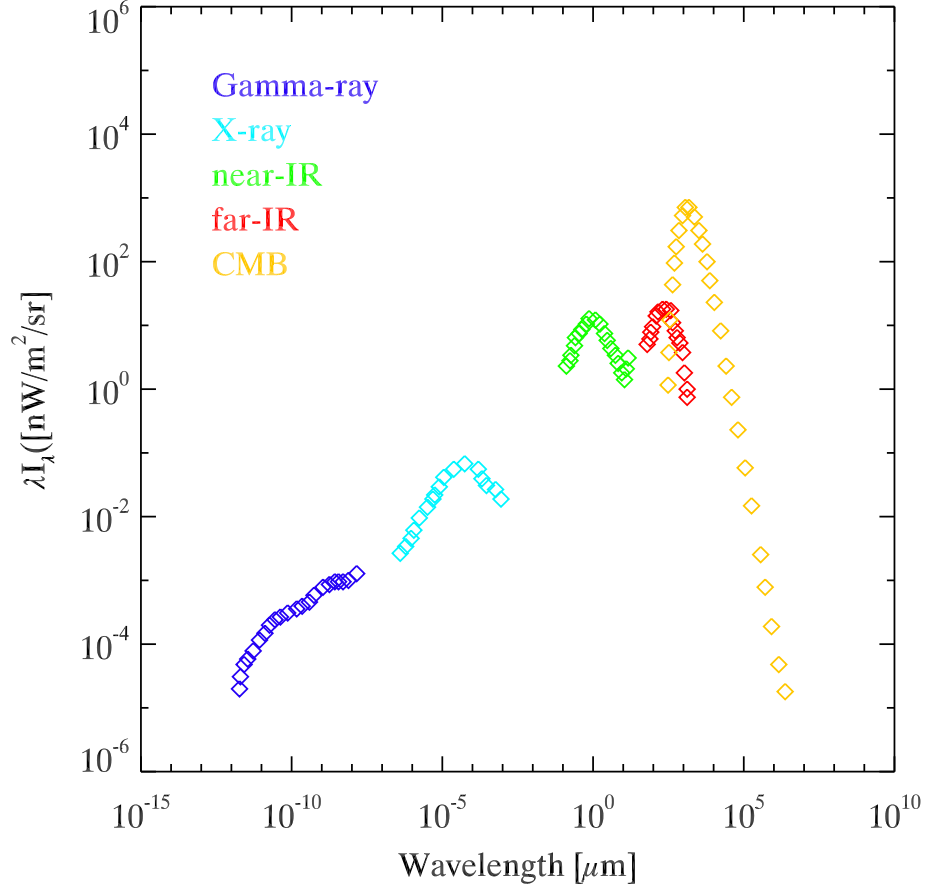


Figure 1.1 EBL intensities for all electromagnetic wavelengths except UV and radio backgrounds. The CMB has the highest energy density of all backgrounds showing blackbody at 2.726 K.  $\gamma$ -ray is the strongest radiation but has the lowest energy density. From  $\gamma$ -ray to CMB, we use data from Fermi-LAT (Ackermann M et al. 2015), SWIFT/BAT (Ajello M et al. 2008), H.E.S.S. (Abramowski et al. 2013), DIRBE (Hauser MG et al. 1998), and Planck (Planck Collaboration, 2015).

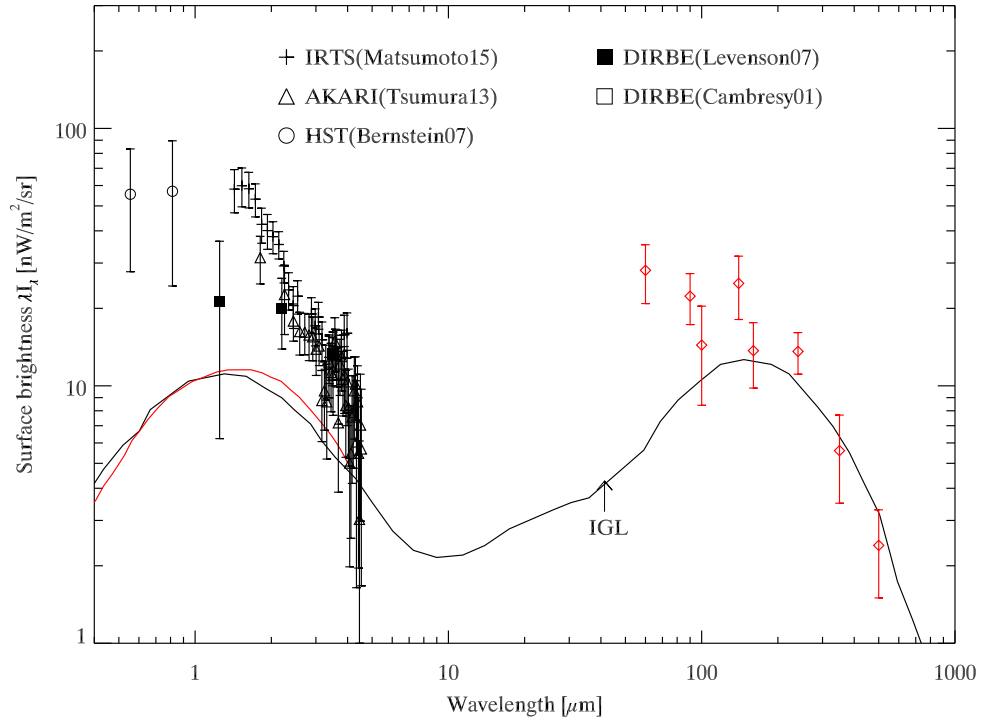


Figure 1.2 EBL intensities measured for near-IR and far-IR. Black solid line is IGL estimated by combining wide and deep galaxy number count data (Driver et al. 2016), Red solid line is the IGL inferred from AEGIS galaxy-SED-type (Dominguez et al. 2011). In NIREBL, they are IRTS (Matsumoto et al. 2015), HST (Bernstein 2007). In far-IR EBL, we draw all data in red for the COBE/DIRBE, COBE/FIRAS, Herschel/PACS, Spitzer/MIPS (see Table 4. in Dwek & Krennrich, 2012).



### 1.1.2 NIREBL detection methods

There are mainly three ways to measure the NIREBL. Measuring absolute brightness, fluctuations and observing  $\gamma$ -ray blazars are those. Here we introduce those measurements while we use first two methods in our work.

#### Absolute brightness

Absolute brightness is a direct measurement of background energy in flux. It is analogous to stellar photometry which subtracts background from observed stars. Simply, the background brightness is measured in a reverse way by subtracting stars from the sky brightness. However, simple star subtraction does not give us NIREBL brightness. There are additional diffuse components we need to consider and subtract. The first one is the Zodiacal Light (ZL) which is the scattered Sun light in the Interplanetary Dust Particle (IPD). The second one is scattered star light from the interstellar medium (Diffuse Galactic Light, hereafter DGL). The third one is the Integrated Star Light (ISL) over all magnitude of Galactic stars above the detection limit of telescope. The last one is the Integrated Galactic Light (IGL) comprises of known galaxies resolved from current telescope. Among those foregrounds, the ZL is the brightest and varies due to the seasonal variation by Earth revolution around the Sun. The details about foreground modelings are discussed in Section 3.4.2. In addition, accurate flux calibration as well as foreground estimation is the crucial key since we measure the absolute flux of the background.

#### Fluctuations

Fluctuation measures angular power spectrum of spatial brightness. It reveals how sources are distributed as a function of angular scales. The degree of relative brightness variations about the mean level is appeared as an amplitude in the power spectrum. Since even the strong ZL brightness appeared as smooth component in

brightness variations around mean over the large angular scales ( $< 0.03\%$ ; Pyo et al. 2012), the accuracy of foreground measurement is not critical problem. Therefore, it is less sensitive to the foreground subtraction distinct from *Absolute brightness* measurement (Kashlinsky et al. 1996).

### $\gamma$ -ray blazars

Blazar is a subset of AGN with relativistic jets oriented at small angles to the line of sight towards the observer. The outflows are close to the speed of light produced by accretion of gas from the surroundings. Via inverse compton scattering with NIREBL photons,  $\gamma$ -rays are partly absorbed and the attenuation is appeared in observed blazar spectrum. Therefore, the farther the blazar locates, the higher the attenuation is. Several studies estimated the upper limit of NIREBL brightness by analyzing the amount of attenuation in blazar spectrum. However, we need to assume the intrinsic spectrum of blazar which is derived from Synchrotron Self-Compton (SSC) model. Therefore, the blazar spectrum has large uncertainties in observation. In other words, the lack of knowledge on the blazar spectrum limits the measurement of attenuation and thus the NIREBL brightness.

## 1.2 Previous Studies

For decades, studies on the NIREBL have been established both on the observations and the theories. Here, we review the previous observations and studies on the NIREBL.

### 1.2.1 NIREBL

After few decades of Jim Peebles predicting the brightness portion from the early universe in 1967, several space telescopes have succeeded observing the brightnesses

of the diffuse background in near-IR as well as excess fluctuations out to  $1^\circ$ . However, there were many trials and errors. In the beginning, the NIREBL observations were tried using ground based telescopes but failed due to bright atmospheric emission and instrumental noise. To overcome the Earth effect, rocket based observations above the Earth atmosphere were performed (Matsumoto et al. 1988; Noda et al. 1992; Matsuura et al. 1994). However, these early attempts were also failed due to foregrounds subtraction errors caused by limited exposure time.

The first valuable measurement was done from the DIRBE on the COBE satellite in absolute brightness although it had difficulty in subtracting the galactic stars due to too bright confusion limit (Gorjian et al. 2000; Wright & Reese 2000; Cambr  sy et al. 2001; Levenson et al. 2007; Sano et al. 2015; Sano et al. 2016). They found significant excess brightness above IGL. Subsequently, observations using IRTS/NIRS also succeeded to observe isotropic background at short wavelengths with better precision due to the smaller beam size and low resolution spectroscopy (Matsumoto et al. 2005). The results between COBE and IRTS are consistent well at common wavelength region ( $\lambda > 2\mu\text{m}$ ). Follow-up observation using AKARI/IRC ( $2.4\mu\text{m} < \lambda < 4.1\mu\text{m}$ ; Tsumura et al. 2013) detected consistent NIREBL brightness with better resolution and detection limit. Significant excess was also found at short wavelength ( $1.4\mu\text{m} < \lambda < 1.8\mu\text{m}$ ) using HST/NICMOS data (Bernstein 2007). Their measurements are plotted in Figure 1.3.

The excess brightness is initially explained with first stars formed at reionization era (Santos et al. 2002, Salvaterra & Ferrara 2003). However, theoretical model tells that the star formation was not efficient enough to radiate observed excess brightness (Madau & Silk 2005). If this is true, another source is needed to explain the excess brightness.

Nevertheless, several studies disagree excess brightness and interpreted as measurement error. There are mainly two main controversies on the excess brightness.

One is the foreground subtraction error. Since the ZL is the strong foreground component, NIREBL excess brightness can be induced from ZL subtraction error. Dwek et al. (2005) insists that the NIREBL spectrum is similar to the ZL spectrum for COBE/DIRBE and IRTS/NIRS. However, current short wavelength observation rejects the argument since the observed NIREBL spectrum shows bluer than ZL spectrum. Second, the observed blazar SEDs show that the attenuation is not significant to explain NIREBL excess brightness but similar to IGL which represents the excess brightness can be explained by IGL. Since the approach assumes intrinsic blazar spectrum from Synchrotron Self Compton (SSC) model, it is still under debate. We need to observe statistically large number of blazars to confirm the result.

On the other hands, the first detection of NIREBL excess fluctuation was achieved from Spitzer/IRAC in a range of  $3.6 \sim 8 \mu\text{m}$  after subtracting faint-end galaxies up to  $m_{AB}=25$  (Kashlinsky et al. 2005) at arcminute scales. Subsequently, using deep and large FoV of Spitzer/IRAC data, the excess fluctuation at larger angular scales out to  $1^\circ$  was detected confirming previous measurement (Kashlinsky et al. 2012, Cooray et al. 2012). Using HST/NICMOS data, Thompson et al. (2007) measured fluctuation at  $1.4 \sim 1.8 \mu\text{m}$  at sub-arcminute scale. Matsumoto et al. (2011) tried to detect fluctuation at angular scales between the Spitzer and HST using AKARI and found significant excess fluctuation ( $2.4 \mu\text{m} < \lambda < 4.1 \mu\text{m}$ ) at arcminute scales. In summary, they all show significant excess fluctuations from sub-arcminute to  $1^\circ$ . Figure 1.4 shows representative NIREBL fluctuations. The fluctuation exceeds shot noise power towards large angular scales.

Although the fluctuation measurement is less sensitive to strong foregrounds such as ZL, several studies claim that the faint normal galaxies can explain the fluctuation (Cooray et al. 2007, Chary et al. 2008). There is still debate since we mostly depend on the model to explain excess emission or fluctuation. Cooray et al. (2012) and Zemcov et al. (2014) tried to explain excess fluctuation using Intra

Halo Light (IHL) at  $z < 3$  from tidally stripped stars during galaxy mergers and interactions. However, they found the model prediction cannot explain the observed fluctuation. We discuss several proposed candidates in next section.

### 1.2.2 NIREBL candidates

There are several candidates which may contribute to the NIREBL brightness such as the first stars in the early universe and the faint star light distributed around nearby galaxies. Or there can be new populations that have never been observed. In this section, we review characterizations of each candidate sources.

#### First stars

According to the  $\Lambda$ CDM model, the universe has begun with the BigBang. Initially, the universe was fully ionized in hot dense environment that photons were scattered by electrons and protons. As the universe expanded and cooled down, the electrons and protons were bound to form neutral hydrogen and gradually become transparent that the photons could travel freely as mean free path increases which we call the last scattering. The phenomena is observed as CMB showing 2.726 K blackbody radiation redshifted from  $z \sim 1100$ . After the recombination, the universe became dark that no radiation sources exist which we call the dark age. The dark age had been maintained until stars and galaxies lighten the universe again via nucleosynthesis at  $z \sim 10$  (Thomson scattering  $\tau = 0.087 \pm 0.017$ ). The primordial stars and galaxies then reionize the universe slowly until  $z \sim 6$ . For such a long periods, some part of ionization could be performed by Population II stars made after the death of the Population III stars. There are four radiation processes from first stars: direct stellar emission, indirect emissions such as free-bound, free-free, and Lyman alpha from the ionized clouds surrounding the stars. Of all, the Lyman alpha is the strongest at around Lyman break position. Since the neutral hydrogen surrounds the stars, UV

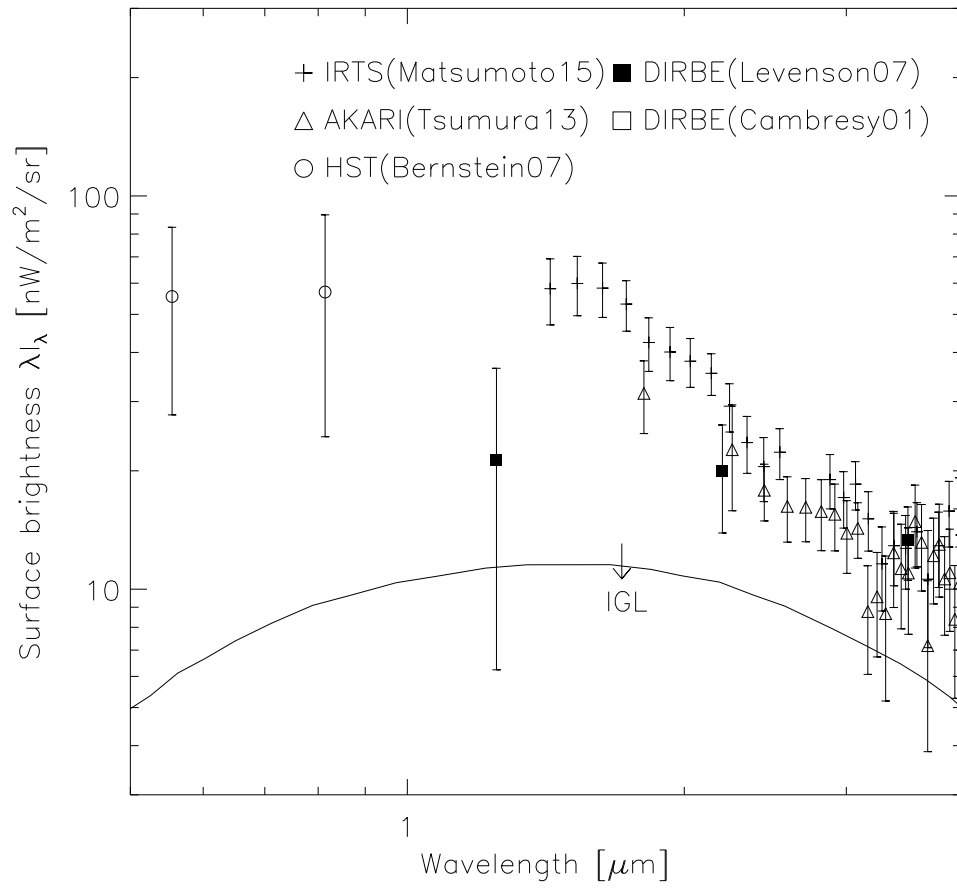


Figure 1.3 Same plot in Figure 1.2 but only NIREBL is drawn.

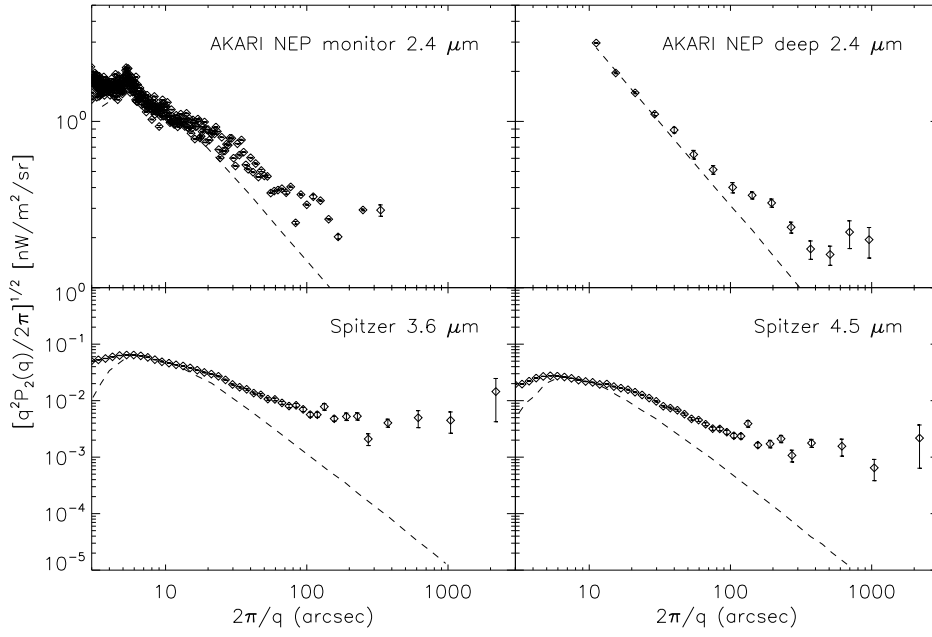


Figure 1.4 Fluctuation spectra measured from previous studies. Angular scale ranges from a few arcsec to sub-degree. Left top: AKARI NEP monitor  $2.4 \mu\text{m}$  (Matsumoto et al. 2011), Right top: AKARI NEP deep  $2.4 \mu\text{m}$  (Seo et al. 2015), Left bottom: Spitzer  $3.6 \mu\text{m}$  (Kashlinsky et al. 2012), Right bottom: Spitzer  $4.5 \mu\text{m}$  (Kashlinsky et al. 2012). The dashed line denotes shot noise fluctuation. The uncorrected PSF causes sharp drop at small angular scale.

radiation is absorbed in the cloud and re-emitted in Lyman-alpha. This re-processed light is then redshifted as the universe expands and expected to be seen as Lyman break at around  $1\ \mu\text{m}$ . The formation and evolution of the objects in this early epoch is very important to understand our universe. However, we have no direct detections of first objects due to the detection limit of telescope.

### **Direct Collapse Black hole**

First stars are formed in mini-haloes with insufficient metal free cooling process (i.e.  $\text{H}_2$  line emission). However, larger haloes ( $T_{\text{vir}} > 10^4\ \text{K}$ ) is not likely cooled down to be fragmented into smaller haloes to form stars. It rather made Direct Collapse Black Hole (DCBH) with mass ranges from  $10^4$  to  $10^6\ M_{\odot}$  (Bromm & Loeb 2003). Thus, DCBH is formed inside metal-free haloes at early universe ( $z < 12$ ). The DCBH is highly obscured by neutral hydrogen ( $N_H > 10^{25}\ \text{cm}^{-2}$ ) due to the gas accretion. Currently there is no observation due to its faintness but this source can explain the Supermassive Black Hole (SMBH; Petri, A. et al., 2012) at  $z \sim 6$  where such a high mass black hole is unlikely to be formed. The black hole absorbs strong energies from UV to X-ray and reprocesses into optical to UV which is then redshifted to near-IR. The NIREBL contribution from DCBH is studied by cross correlating Spitzer data with soft X-ray background (Yue et al. 2013).

### **Intra-Halo Light**

Intra-Halo Light (IHL) is star light tidally stripped around galaxies by collisions and mergers. Although they exist relatively nearby universe ( $z < 3$ ), it is difficult to observe. By star counts, several studies found that IHL fraction in our MilkyWay is  $\sim 1\%$  of total Galactic luminosity. In galaxy group or cluster sized system, the IHL fraction reaches over  $40\%$  depending on system. By stacking the 683 bright central galaxies in the clusters, Zibetti et al. (2005) found the surface brightness



does not follow de vaucouleur's law ( $R^{1/4}$ ) but it shows much brighter outer radii of galaxy. Their surface brightness is  $\sim 30$  magnitude. The number of stripped stars to form IHL is proportional to the halo masses governed by dark matter distributions (Purcell et al. 2007). To explain the current excess fluctuation measurements, the halo masses should be in a range of  $10^9$  to  $10^{12} M_{\odot}$  and populate at  $z < 3$  (Cooray et al. 2012).

### Other possible candidates

Although there is no successful observation yet like first stars, dark stars may exist powered by dark matter (Maurer et al. 2012). Like nuclear fusion process in typical first stars, dark stars radiates its energy via annihilation process of Weakly Interacting Massive Particle (WIMP). This weak interaction produces electron, positron,  $\gamma$ -ray, and neutrinos. The products then collide with surrounding clouds to heat up. When the heating process is much more powerful than the cooling, the cloud collapses to form dark star powered by dark matter. The masses of initial dark star is a few solar masses and keep grow by accreting atomic masses as well as dark matter to be annihilated. It grows until it run out of dark matter fuel and collapse to form first star radiating its energy via nuclear fusion. In theory, dark star can live longer than general first stars and it may present in the universe. The numerical solution of dark stars tells they can contribute a few percent in NIREBL background brightness (Maurer et al. 2012). In addition, another faint source can be an NIREBL origin. According to the  $\Lambda$ CDM model, first galaxies, formed in small halos with mass less than  $10^9 M_{\odot}$ , may evolve into faint dwarf galaxies as we observe today. Although those galaxies were probably masked with their host galaxies, we cannot exclude and need deeper and multiwavelength observations.

### 1.3 The purpose of this study

Figure 1.3 shows the previous measurements of the NIREBL. The NIREBL brightness is a factor of 2 to 8 times larger than the IGL depending on the wavelengths. With peak at  $\sim 1.5 \mu\text{m}$ , measurements at shorter and longer wavelengths show consistency within error range. In theory, NIREBL spectrum shows Lyman break below  $\sim 1 \mu\text{m}$  if the first star is the dominant source. Nevertheless, current studies reveal that the first star does not contribute much but there are other various candidates have to be considered as described in Section 1.2.2. We can approach in two ways. One is to decompose sources into each wavelength using well-established models. These models, however, do not clearly explain the excess brightness and fluctuation as well. We need additional sources or more confident models in the future. Another is to measure the NIREBL for unexplored wavelength or angular scale in brightness or fluctuation spectrum. When we have complete and quite informative spectrum, it is more viable to constrain energies of the NIREBL sources.

Our study is focused on the latter approach. For the absolute brightness measurement, we are lack of the NIREBL spectrum below  $1.4 \mu\text{m}$  as shown in Figure 1.3. For the fluctuation measurement, current measurements were performed at angular scales below  $1^\circ$  for wavelengths above  $2.4 \mu\text{m}$ . We wonder whether the fluctuation increases or decreases beyond  $1^\circ$ . To answer those questions, we analyze the data from the CIBER sounding rocket (Section 2) and the IRTS space telescope (Section 3). In Section 4, we discuss the results and their limitations and introduce future missions to probe the NIREBL origins.



## Chapter 2

# CIBER experiments and results

### 2.1 Overview

The CIBER is a NASA sounding rocket designed for study the NIREBL above the Earth's atmosphere. From the first launch on 2009 Feb through 2013, it has flown four times via payload recovery. The CIBER investigate the NIREBL with two approaches for wavelength ranges which were not covered before. One is the absolute brightness and another is the spatial fluctuation. Absolute brightness approach measures the brightness of the NIREBL at around  $1\ \mu\text{m}$ . And spatial fluctuation evaluates the NIREBL at wavelength ranges below  $2.4\ \mu\text{m}$ .

However, we found that the flux calibration for the 4th flight is different with others on analyzing the data. Since there were no changes in optical or mechanical systems of payload, the difference was not understood. We calibrate the 4th flight data using calibration factor measured for the 3rd flight. To validate the calibration between flights, we use stars' spectra observed from both flights and they show consistency for wavelength ranges below  $1.7\ \mu\text{m}$  which validates the 4th flight result for the NIREBL study. This manuscript is published in Kim et al. 2017.

Here, we describe the CIBER pre-flight experiments and observations for valida-

tion of the 4th flight flux calibration. Based on the results, we briefly introduce the NIREBL measurements from the CIBER.

## 2.2 Instruments

Inside the payload, four telescopes are mounted on the common optical bench as shown in Figure 2.1. Two are I- and H-band Imagers and the other two are spectrometers which are named Narrow Band Spectrometer (NBS) and Low Resolution Spectrometer (LRS). Their focal plane assemblies are cooled down to 77K using liquid-nitrogen. The CIBER is designed to observe low background brightness. We designed payload with care. To reduce the IR emissivity induced by the heat-up of rocket skin during the flight, payload inside is coated with gold. Four telescopes on the optical bench are shielded with aluminum radiation plate for low radiative load. In addition, passively cooled plate is attached inside of the front door to prevent thermal radiation from heated door during the flight.

As described in Section 1.1.2, there are mainly two methods to measure the NIREBL. The purpose of Imagers is to measure any clustering that contribute to the NIREBL based on the fluctuation analysis in I- and H-bands. The LRS is designed to measure absolute brightness of the NIREBL at wavelength around  $1\ \mu\text{m}$ . In both measurements, we need to subtract the brightnesses of foregrounds, especially, the ZL which accounts for the  $\sim 90\%$  of the sky brightness. Another spectrometer, NBS, is designed to measure absolute level of the ZL. For the spectrometers measuring the absolute level of background, dark current should be accurately subtracted. To measure the dark current, we installed cold shutter for the spectrometers as well as Imagers. Although Imager do not need absolute flux level for the fluctuation analysis, cold shutter is installed to clear instrumental noise appeared in small angular scale. Calibration lamp is installed to all telescopes to check the stability during flight. Detailed specifications of each telescope are described in this section.

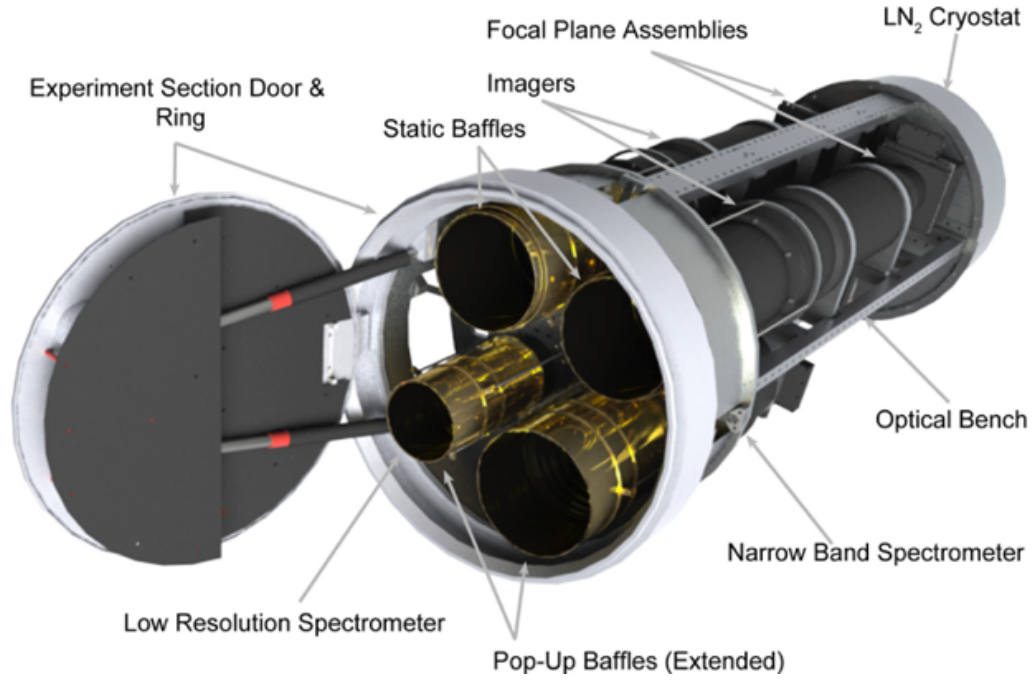


Figure 2.1 The CIBER payload and installed telescopes. All four telescopes are installed on the common optical bench. Top two telescopes are the H- and K-band Imagers. Bottom left one is the LRS and bottom right one is the NBS. Two types of baffles are drawn. One is static baffle and another is popup baffle. From second flight, popup baffles were additionally installed to all telescopes. Black coatings inside baffles are laserblack <sup>1</sup>. LN<sub>2</sub> tank is located at the backside of the payload. The LN<sub>2</sub> cools down the detectors to 77 K. The door was opened when observation began and automatically closed when it ended before landing on the ground with parachute. The photograph is retrieved from Zemcov et al. (2013).

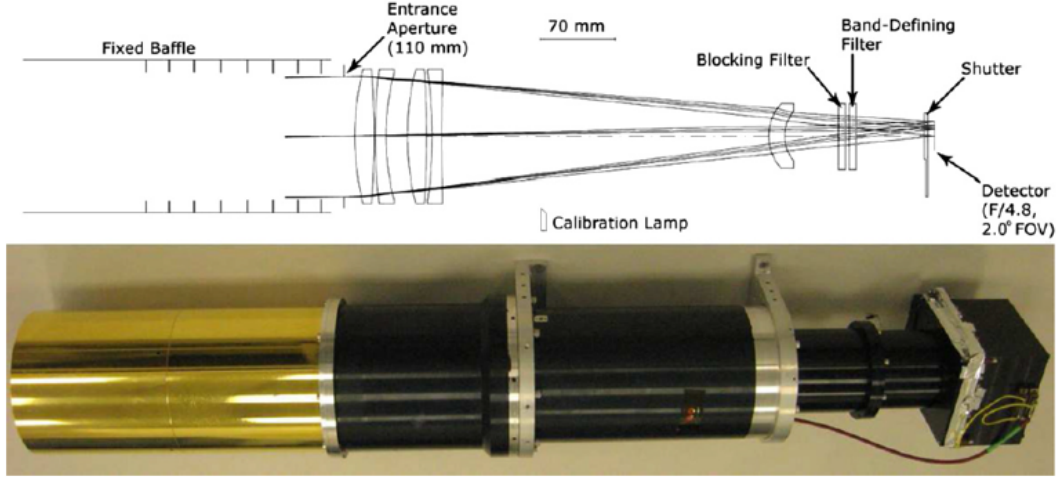


Figure 2.2 Optical cross sectional schematic and photograph of the Imager. Both H- and K-band are identical except filter inside. The Imager is  $2^\circ \times 2^\circ$  FoV refracting telescope with HAWAII-1 detector array. Light path is shown in optical schematic. Calibration lamp is electronically controlled to check detector stability. Shutter is in close status for dark. Static baffle is threaded and the surface is treated with laserblack to block stray light.

### 2.2.1 Imagers

Two imagers are equipped with central wavelengths at 1.1 and 1.6 $\mu$ m (Bock et al. 2013). The Imager is designed to estimate fluctuation level from  $7'$  to  $2^\circ$  angular scale. Two bands are used to effectively discriminate astronomical and instrumental sources since the contributions of sources depend on the wavelength as well as angular scale. Both telescope has 11-cm aperture size and uses Teledyne HAWAII-I 1024  $\times$  1024 pixel arrays to cover  $2^\circ \times 2^\circ$  Field of View (FoV). Size of each pixel is  $7'$  to reduce local galaxies down to 23.0 and 21.5 mag for I- and H-band, respectively. See the Imager photograph in Figure 2.2.

### 2.2.2 LRS

LRS is a prism based spectrometer to measure the NIREBL with wavelength coverage from 0.7 to 2.1  $\mu\text{m}$  (Tsumura et al. 2013). It is designed to cover 1  $\mu\text{m}$  which is essential to measure redshifted Lyman alpha radiation from Epoch of Radiation (EoR). It has an aperture size of 5-cm in diameter and five long slits ( $2.8' \times 5.8^\circ$ ) as shown in Figure 2.3. Therefore, the LRS covers  $5.8^\circ \times 5.8^\circ$  Field of View (FoV). The incident beam is passed through slit and spectrally dispersed via prism which is then illuminated on the detector appearing five strips as shown in Figure 2.7. The detector has  $256 \times 256$  pixels where each pixel scale is  $1.36' \times 1.36'$ . The detector array is read non-destructively at  $4\text{Hz frame}^{-1}$ . See the LRS photograph in Figure 2.3.

### 2.2.3 NBS

Since the brightness of Zodiacal Light has seasonal variation induced by Earth's revolution around the Sun, it is important to measure the ZL brightness at the same time of NIREBL observation using LRS. NBS is specially designed to measure the ZL brightness using Fraunhofer absorption line (Korngut et al. 2013). It measures intensity of CaII lines with central wavelength at 854.2 nm. It is a 7.5-cm aperture refractive telescope with a Fabry-Perot filter with  $\lambda/\Delta\lambda \sim 1000$  to spectrally resolve CaII line. Fabry-Perot has two reflecting surfaces to transmit only interferenced light that satisfies  $\lambda = \lambda_0 \cos\theta_0$ , where  $\theta$  is angle of incident light. The satisfied light form concentric circles on the detector. It has same detector array as LRS. See the NBS photograph in Figure 2.4.



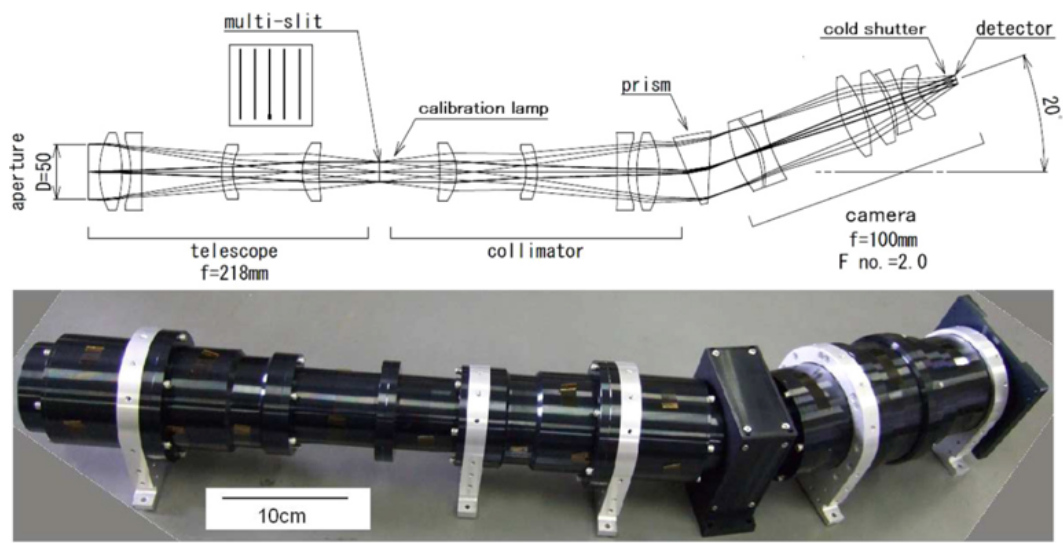


Figure 2.3 Optical cross sectional schematic and photograph of the LRS. The LRS is  $5.8^\circ \times 5.8^\circ$  FoV spectrometer with PICNIC detector array. Light path is shown in optical schematic. Incident light passes 5 hole multi-slit and dispersed at prism. Calibration lamp is electronically controlled to check detector stability. Shutter is in close status for dark. Static baffle is threaded and the surface is treated with laserblack to block stray light.

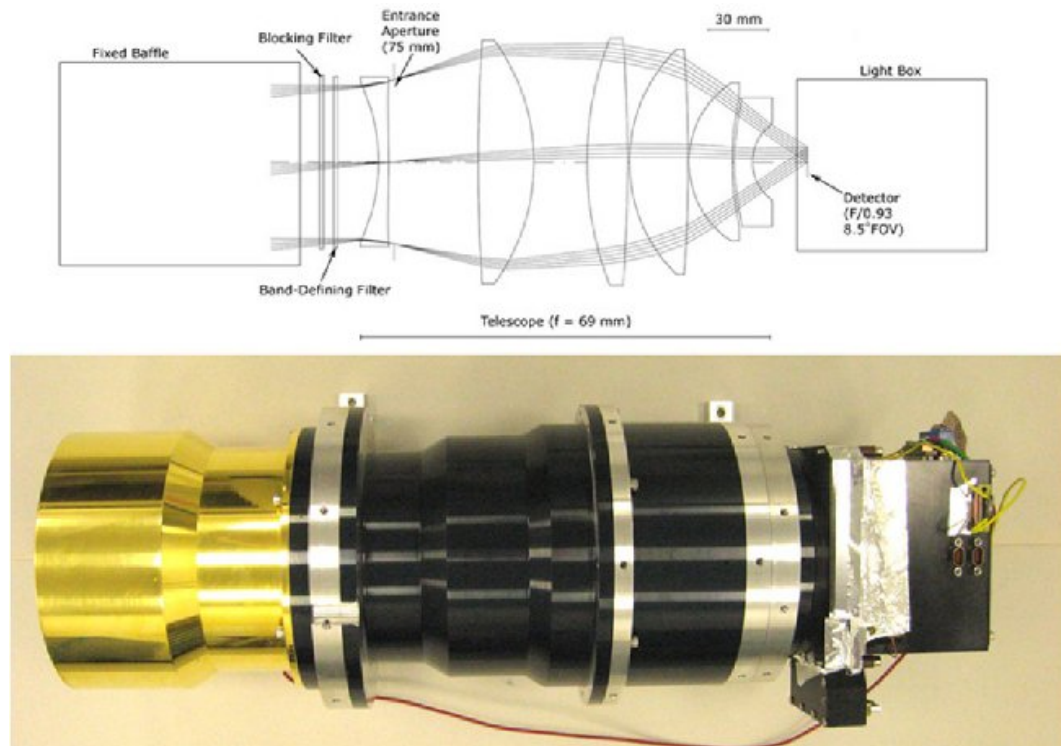


Figure 2.4 Optical cross sectional schematic and photograph of the NBS. The NBS is  $8^\circ \times 8^\circ$  FoV spectrometer with PICNIC detector array. Light path is shown in optical schematic. Calibration lamp is electronically controlled to check detector stability. Shutter is in close status for dark. Static baffle is threaded and the surface is treated with laserblack to block stray light.

## 2.3 Laboratory experiments

Before each flight, we carried out various tests and calibrations in the laboratory. Tests are focus test, stray light analysis which are necessary to optimize system before observation. In addition to analyze the flight data, absolute calibration, wavelength calibration, and flat image acquisition were carried out. Here we describe details of each laboratory experiment.

### 2.3.1 Calibration

Calibration tests are absolute calibration and wavelength calibration. Since both tests are not possible to achieve precisely during the flight, we need to perform in the laboratory before each flight.

#### Absolute calibration

For spectrometers, absolute calibration is difficult using standard star due to unknown PSF and pointing accuracy. Before each flight, absolute calibration was done at laboratory in collaboration with the NIST (National Institute of Standards and Technology). Two types of calibration tests were prepared. Both have same configuration except light source. We use tunable Spectral Irradiance and Radiance Responsivity Calibrations (SIRCUS) laser (Brown et al. 2006) that covers wavelengths from 0.7 to 2.1  $\mu\text{m}$  and white light source from Quartz Tungsten Halogen (QTH) lamp. Nevertheless, since the calibration results from white light source varies up to 30 % between tests before each flight, we use calibration result obtained from SIRCUS laser source. The light source is attached to the integrating sphere and the homogeneous light is entered through output port which is viewed by LRS aperture. Absolute brightness of input source is measured by absolutely calibrated radiometer. The ambient brightness was measured at each wavelength step by shuttering the

light source and subtracted. The conversion factor of the detector is then derived by taking the ratio of the signal between detector and radiometer. Details on the laboratory experiments concerning these measurements can be found in Arai et al. (2015). The systematic uncertainties are estimated to be around 3 %.

### Wavelength calibration

For LRS and NBS spectrometers, we calibrated positions at which wavelength is imaged on the detector. Since small amount of displacement gives rise to variations in the pixel position of observed spectra, we carried out wavelength calibration before each flight. Two different sources are used to cover whole wavelength coverage, especially for the LRS. One is SIRCUS laser that covers  $0.7 \sim 1.0 \mu\text{m}$  and another is QTH lamp with monochrometer that covers from  $0.7 \sim 2.0 \mu\text{m}$ . For accurate measurements, we calibrate the SIRCUS laser with external wavemeter and monochrometer using He-Ne laser. Both sources are attached to the integrating sphere that homogeneous light is illuminated on to whole FoV of telescope. Since wavelength coverage for SIRCUS laser and QTH lamp are overlapped between  $0.7 \sim 1.0 \mu\text{m}$ , we could check their consistency. Uncertainties of those calibrations are more than two orders of magnitude smaller than the LRS spectral resolution ( $\Delta\lambda \sim 0.01 \mu\text{m}$ ).

#### 2.3.2 Flat field

The different pixel response causes artificial noise and we corrected it using flat image taken at laboratory. The experiment was performed in the same manner as Absolute calibration in Section 2.3.1. Using the integrating sphere between the light source and the telescope, the uniform radiation is illuminated to the detector. The uniformity of illumination is varied less than 1 % (Korngut et al. 2013). Here, independent measurements using three different types of light sources (i.e. SIRCUS laser, Super Continuum Laser (SCL), and QTH lamp) has been carried out to check

any systematics. We then average three different results to make final flat image. They are distributed  $\sim 3\%$  from unity.

### 2.3.3 Focus test

In the laboratory, focus test was performed to find the best focus for each telescope. The best focus enables us to identify stars efficiently up to limiting magnitude and ultimately makes possible to study background by removing all detectable point sources. Usually, the focus adjustment has been done by changing the detector position while looking a spot imaged on the detector at the same time. Here, the spot can be from a star or collimated light in the laboratory. However, the CIBER is a cryogenic system cooled down by 77 K to operate the detector and there is no remote control system to change the detector position when it is in the cryogenic system. This makes impossible to adjust best focus in real time.

Instead, we use autocollimator to find the best focus. The autocollimator has focuser with pinhole at prime focal point and plane mirror is placed in front of its aperture. The input light source from focuser is then reflected back from a plane mirror. There is also a beam splitter at the prime focal point that we can directly see the reflected light from the plane mirror. The reflected light is seen as a spot having a certain size depending on the position of focuser. First, we find the sharp and bright spot by moving the focuser back and forth. We focuser position at best spot is called *zero point*. Next, we replaced the flat mirror with telescope that collimated light can now be illuminated into the telescope. Since the collimated light is illuminated with a certain fixed angle, we can see a spot imaged on the detector. The spot is mostly blurred than designed PSF size and this indicates we need to move detector at best focus position of telescope. As noted, however, we cannot change the detector position when it is in the cryogenic system. We, instead, move the focuser at the autocollimator with constant steps. At each step of movement, we analyze the spot

size imaged on the detector. As shown in Figure 2.5, the spot size described in Full-Width Half Maximum (FWHM) is varied with focal position. With polynomial fit, we can find the best focal position of detector. The difference between the *zero point* and the best focal position let us know how much detector is defocused from the best focus position. This has been done for every corners of detector to position the detector at best focus position. The positioning has been done by inserting or removing *sim*s after take the detector a part from cryogenic system.

#### 2.3.4 Stray light test

The stray light is critical issue to observe low background brightness. This should be treated more carefully in infrared since not only the scattered light but also the thermal emission contaminated the observed data. To study background, CIBER is designed to eliminate the stray light. The initial design for the first flight uses black anodized static baffle in front of aperture at each telescope. However, during the first flight we observed thermal emission from the heated rocket skin due to the air friction, which scattered off inside the door and entered the detector. This causes significant noise that we could not use the first flight data for scientific purpose.

To mitigate the stray light from the second flight, we redesign the baffle and the door inside. Instead of black anodizing of the baffle, the inner surface was threaded and coated with the laserblack. In addition, to extent the length of the baffle, popup baffle was installed which is compressed when the door close and popped up when the door is open at the beginning of the observation. The door inside is treated with black anodization to reduce the radiation from outer skin. The coating materials were chosen from laboratory experiment and detail of experiment is described in Appendix.

In practice, we test stray light using the CIBER payload for three different baffle designs: static baffle (black anodized), static baffle (laserblack with thread), static

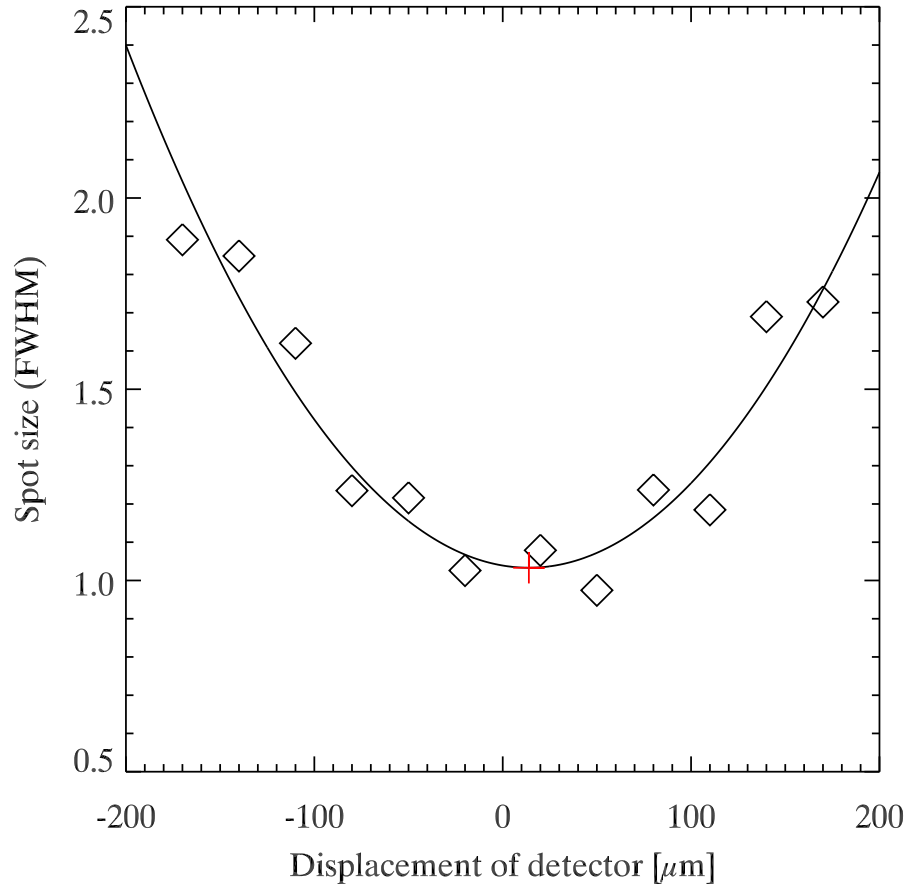


Figure 2.5 Schematic plot for the focus test. Diamond symbols are measured spot size at different focal positions of collimator. Polynomial fit (solid line) is performed to find the best focus position marked in red cross.

baffle (laserblack and thread) with popup baffle (laserblack). The Figure 2.6 shows the incoming stray light comparison between baffles from first flight and redesigned second baffle. Test has been performed with custom made payload-stand that can control the angle between the light source and the telescope. The test has been carried out at room temperature. Thus, we replace the PICNIC detector with silicon photo diode. The collimated beam is illuminated on the telescope. We use the chopped light with certain frequency to reduce the noise from ambient light. The intensity of collimated light was measured for angles from 0 to 90°. The static baffle for the second flight shows an order of magnitude lower stray light than the first flight one. The stray light has been much reduced when we install the popup baffle.

## 2.4 Field selection

CIBER observed 7 ~ 8 fields depending on the flight. They are chosen in two different purposes. One is for the background study (hereafter, science fields) and another is for the ZL (hereafter, ecliptic fields). Due to the strong ZL near the ecliptic latitude, science fields are chosen located at higher ecliptic latitudes. In addition, one or two ecliptic fields near the ecliptic latitudes are observed to study ZL. The number of ecliptic fields are varied in flights. The detailed flight date and fields were chosen based on the launch window calculation. The specific conditions used for the launch window is described as below.

- (i) Fields are located above 40 ° altitude.
- (ii) Solar elongation angle of fields are between 64 and 124 °.
- (iii) The Moon is below 108.6 ° from the zenith.
- (iv) The Sun is below 113.6 ° from the zenith.
- (v) Fields are located above 30 ° in galactic latitude.



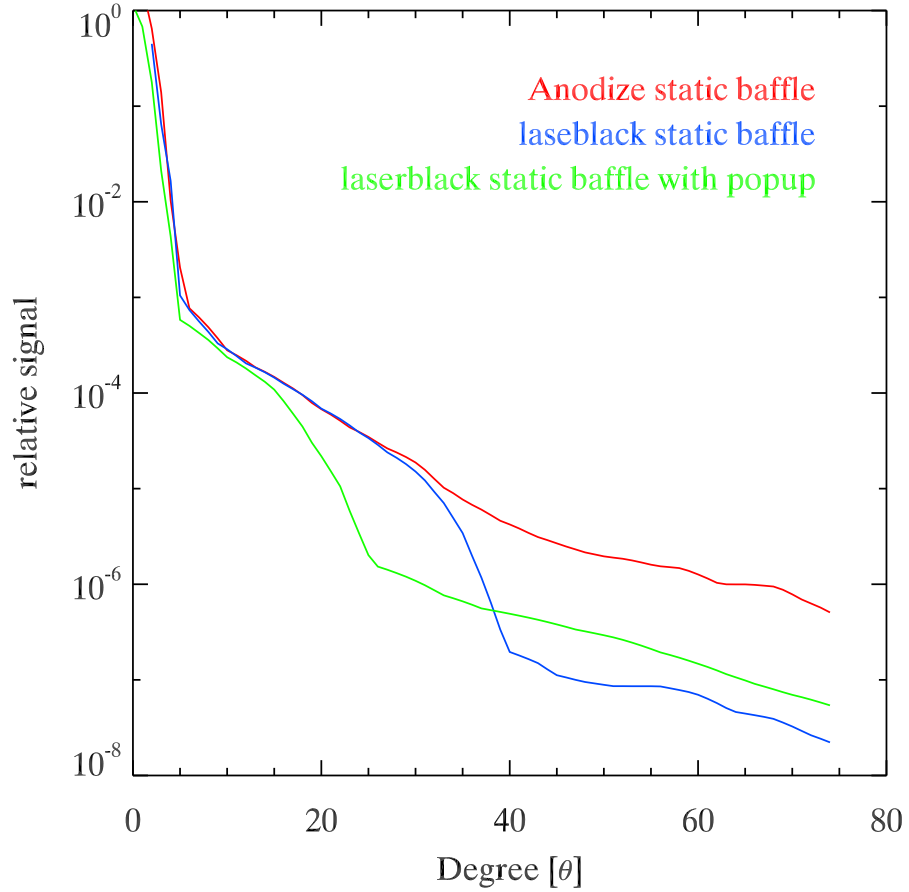


Figure 2.6 Stray light of the CIBER/Imager. The relative signal is normalized at zero angle. Red curve is measured from static baffle attached to the Imager. Here, the static baffle is treated with anodize black to reduce stray light. Blue curve is measured from laserblack surfaced static baffle. Green curve is from static baffle with additional popup baffle with both laserblack treated.

Crit. (i) is chosen to avoid the 300 K blackbody radiation from the Earth. The 300 K radiation is significant noise contaminating observed image in infrared. The brightest diffuse foreground for NIREBL study is ZL. Therefore, the precise estimation of the ZL is very important. To do so, we use Kelsall model based on the COBE/DIRBE data (Kelsall et al. 1998). To estimate ZL based on their model, it is better to observe our fields in same sky condition as described in Crit. (ii). Crit. (iii) and (iv) prevent the direct illumination from the Sun or the Moon. The Sun avoidance angle is  $5^\circ$  larger due to its brightness. Crit. (v) is to avoid strong Galactic foregrounds such as stars and dust. All flights observed three science fields in common. They are NEP, SWIRE, and Bootes fields. They have abundant ancillary data and results for background studies. The details of the observed fields and flight date is in Table 2.1.

Table 2.1. Coordinates and launch information of the observed fields

Flight	Launch date(site)	Field	RA	Dec	$l$	$b$	$\lambda$	$\beta$
1st flight	2009. Feb. 25. (WSMR) <sup>i</sup>	Elat10	234.05	-8.32	357.23	36.63	233.76	10.71
		Elat30	222.75	20.56	25.89	61.96	212.82	35.101
		BootesA	218.75	34.30	57.20	66.69	201.23	46.278
		BootesB	220.04	34.89	58.13	65.54	202.23	47.278
		NEP	270	66.56	96.38	29.81	90	90
		SWIRE	242.75	55	84.89	44.62	208.4	72.629
2nd flight	2010. Jul. 10. (WSMR) <sup>i</sup>	SWIRE	242.84	54.65	84.89	44.62	207.68	72.73
		NEP	270.87	66.45	96.13	29.81	279.88	89.31
		Elat10	226.97	-2.55	356.88	46.08	233.76	10.71
		Elat30	220.86	19.80	23.52	63.31	212.82	35.10
		BootesA	218.51	34.75	58.76	66.79	200.75	46.72
		BootesB	217.30	33.25	55.44	68.02	200.30	44.94
3rd flight	2012. Mar. 22. (WSMR) <sup>i</sup>	Lockman Hole	161.43	58.21	149.41	51.97	135.42	45.49
		SWIRE	242.81	54.59	84.31	44.71	209.32	72.32
		NEP	270.63	66.28	96.06	29.56	311.48	89.62
		Elat30	236.98	9.57	18.64	44.89	234.38	29.25
		BootesB	217.30	33.27	55.13	68.06	200.35	44.82
		BootesA	218.38	34.69	58.33	66.91	200.58	46.69
4th flight	2013. Jun. 5. (WFF) <sup>j</sup>	DGL	251.99	68.76	100.27	36.19	154.03	82.84
		NEP	270.80	66.15	95.91	29.49	307.86	89.48
		Lockman Hole	161.23	58.58	149.07	51.65	135.01	45.74
		Elat10	190.46	8.12	295.67	70.86	186.37	11.6
		Elat30	193.08	28.03	110.75	89.08	179.76	30.70
		BootesB	217.24	33.28	55.18	68.11	200.28	44.80
		SWIRE	242.76	54.68	84.45	44.71	209.05	72.38

<sup>i</sup>White Sands Missile Range<sup>j</sup>NASA Wallops Flight Facility

## 2.5 Flight performance

All CIBER flights were successfully launched and obtained data with no loss from the ground station (Zemcov et al. 2013). Of the four flights, the first flight was experienced the thermal radiation from the 400 K heated rocket skin as described in Section 2.3.4. This makes data not proper for the scientific purpose. The modified version from the second through fourth flight observed with no significant contamination adaptable for the science purposes. Each flight observed with apogees around 330 km with more than 420 sec observing time. In particular, the fourth flight with non-recovery mission achieved apogee of 577 km and 620 sec observing time. The achieved pointing accuracy was less than 3 " over  $\sim 30$  sec integrations.

## 2.6 In-flight calibration from stars

### 2.6.1 Background subtraction

The raw image contains not only spectrally dispersed images of stars, but also the combined emission from Zodiacal light  $\lambda I_{\lambda}^{\text{ZL}}$ , diffuse galactic light  $\lambda I_{\lambda}^{\text{DGL}}$ , the extragalactic background  $\lambda I_{\lambda}^{\text{NIREBL}}$ , and instrumental effects  $\lambda I_{\lambda}^{\text{inst}}$  (Leinert et al. 1998). The measured signal  $\lambda I_{\lambda}^{\text{meas}}$  can be expressed as:

$$\lambda I_{\lambda}^{\text{meas}} = \lambda I_{\lambda}^* + \lambda I_{\lambda}^{\text{ZL}} + \lambda I_{\lambda}^{\text{ISL}} + \lambda I_{\lambda}^{\text{DGL}} + \lambda I_{\lambda}^{\text{NIREBL}} + \lambda I_{\lambda}^{\text{inst}}, \quad (2.1)$$

where we have decomposed the intensity from stars into a resolved component  $\lambda I_{\lambda}^*$  and an unresolved component arising from integrated light of stars below the sensitivity of the LRS  $\lambda I_{\lambda}^{\text{ISL}}$ . It is important to subtract the sum of every component but  $\lambda I_{\lambda}^*$  from the measured brightness to isolate the emission from detected stars. At this point in the processing, we have corrected for multiplicative terms affecting  $\lambda I_{\lambda}^{\text{meas}}$ . Dark current, which is the detector photocurrent measured in the absence of incident flux, is an additional contribution to  $\lambda I_{\lambda}^{\text{inst}}$ . The stability of the dark current in the

LRS has been shown to be  $0.7 \text{ nWm}^{-2}\text{sr}^{-1}$  over each flight, which is a negligible variation compared to the typical dark current (i.e.,  $20 \text{ nWm}^{-2}\text{sr}^{-1}$ ) (Arai et al. 2015). As a result, we subtract the dark current as part of the background estimate formed below.

The relative brightnesses of the remaining background components are wavelength-dependent, so an estimate for their mean must be computed along constant-wavelength regions, corresponding to vertical columns in Figure 2.7. Furthermore, because of the LRS’s large spatial PSF, star images can extend over several pixels in the imaging direction, and even overlap one another. This complicates background estimation in pixels containing star images, and reduces the number of pixels available to estimate the emission from the background components.

To estimate the background in those pixels containing star images, we compute the average value of pixels with no star images along each column as summarized in Figure 2.8. We remove bright pixels that may contain star images as described in (Arai et al. 2015). The spectral smile effect shown in Figure 2.7 introduces spectral curvature along a column. We estimate it causes an error of magnitude  $\delta\lambda/\lambda > 10^{-2}$ , which is small compared to the spectral width of a pixel. Approximately half of the rows remain after this clipping process; the fraction ranges from 45 to 62 % depending on the stellar density in each field. This procedure removes all stars with  $J > 13$ , and has a decreasing completeness above this magnitude (Arai et al. 2015).

To generate an interpolated background map, each candidate star pixel is replaced by the average of nearby pixels calculated along the imaging direction from the  $\pm 10$  pixels on either side of the star image. We again do not explicitly account for the spectral smile. This interpolated background image is subtracted from the measured image, resulting in an image containing only bright stellar emission. The emission from faint stars and bright stars which inefficiently illuminate a grating slit that contribute to  $I_{\lambda}^{\text{ISL}}$  are naturally removed in this process.

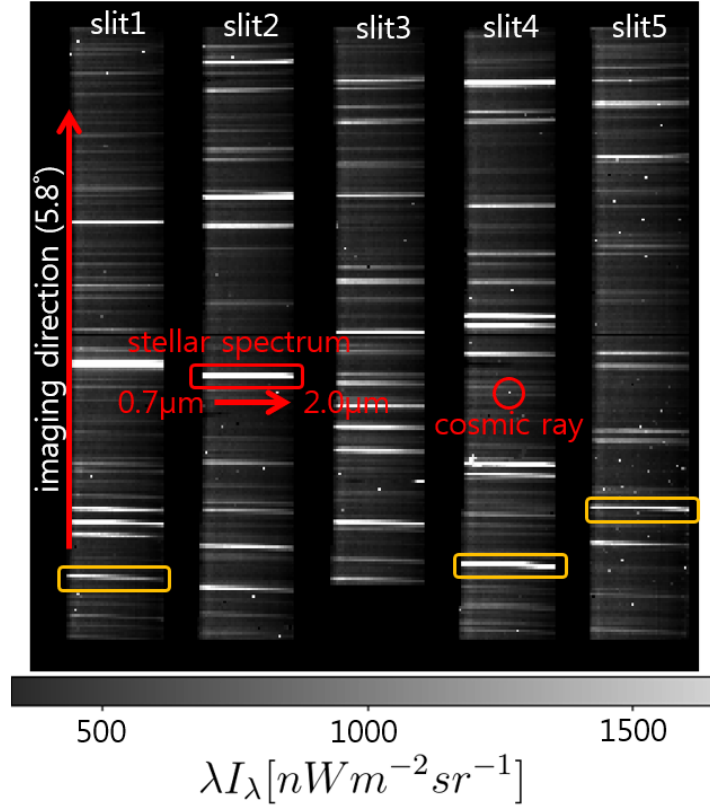


Figure 2.7 An example CIBER/LRS image towards NEP field. The five illuminated columns are dispersed spectra from the five slits of the LRS, and the bright horizontal lines in each column are images of individual stars. As an example, we highlight a single horizontal light trail by the red box, which is the light from a single star dispersed from 0.7 to 2.0  $\mu m$ . The bright dots are pixels hit by cosmic rays. The yellow boxes highlight representative examples of stellar spectra disturbed by the prism. Note that the distortion direction is different between upper and lower part of the image, and the distortion becomes negligible at the center line of the image.

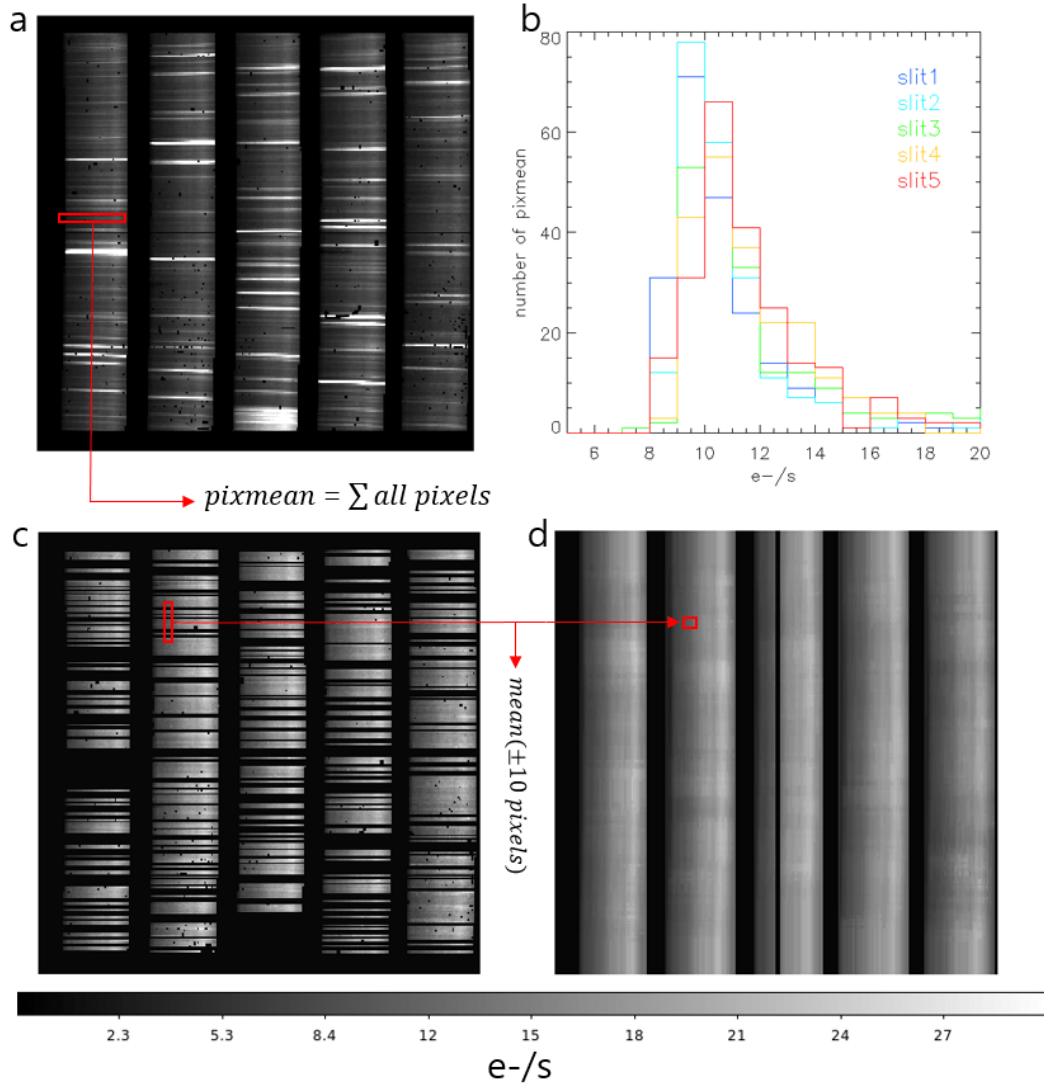


Figure 2.8 Flow chart of the background image construction. (a) Same as Figure 2.7. The red box indicates set of rows to be averaged. (b) Histogram of averaged values for each row. Average values for each slit are drawn with different color. (c) Image after iterate sigma clipping of bright rows from (b). The red box indicates the size of  $\pm 10$  pixels that are averaged. (d) Reconstructed background image including all instrumental noise and undetected faint stars.

### 2.6.2 Astrometry

We match the synthesized LRS  $J$ ,  $H$ , and  $J - H$  information with the 2MASS point source catalog (Skrutskie et al. 2006) to compute an astrometric solution for the LRS pointing in each sky image. This is performed in a step-wise fashion by using initial estimates for the LRS’s pointing to solve for the image registration at fine scales.

As a coarse guess at the LRS pointing, we use information provided by the rocket’s Attitude Control System (ACS) that controls the pointing of the telescopes (Zemcov et al. 2013). This provides an estimated pointing solution that is accurate within  $15'$  of the requested coordinates. However, since the ACS and the LRS are not explicitly aligned to one another, a finer astrometric registration is required to capture the pointing of the LRS to single pixel accuracy.

To build a finer astrometric solution, we simulate images of each field in the 2MASS J-band using the positional information from the ACS, spatially convolved to the LRS PSF size. Next, we apodize the simulated 2MASS images with the LRS slit mask, compute the slit-masked magnitudes of three reference stars, and calculate the  $\chi^2$  statistic using:

$$\chi^2_{p,q} = \sum_i \left( \frac{F_{LRS,i} - F_{2MASS,i}}{\sigma_{LRS,i}} \right)^2, \quad (2.2)$$

where index  $i$  represents each reference star and subscripts  $p$  and  $q$  index the horizontal and vertical position of slit mask, respectively.  $F_{LRS,i}$  and  $F_{2MASS,i}$  are fluxes in the LRS and 2MASS  $J$ -band, and  $\sigma_{LRS,i}$  is the statistical error of the LRS star. The minimum  $\chi^2$  gives the most likely astrometric position of the slit mask. Since, on average, there are  $\sim 5$  bright stars with  $J < 9$  per field, spurious solutions are exceedingly unlikely and all fields give a unique solution.

Using this astrometric solution, we can assign coordinates to the rest of the detected LRS stars. We estimate that the overall astrometric error is  $120''$  by com-



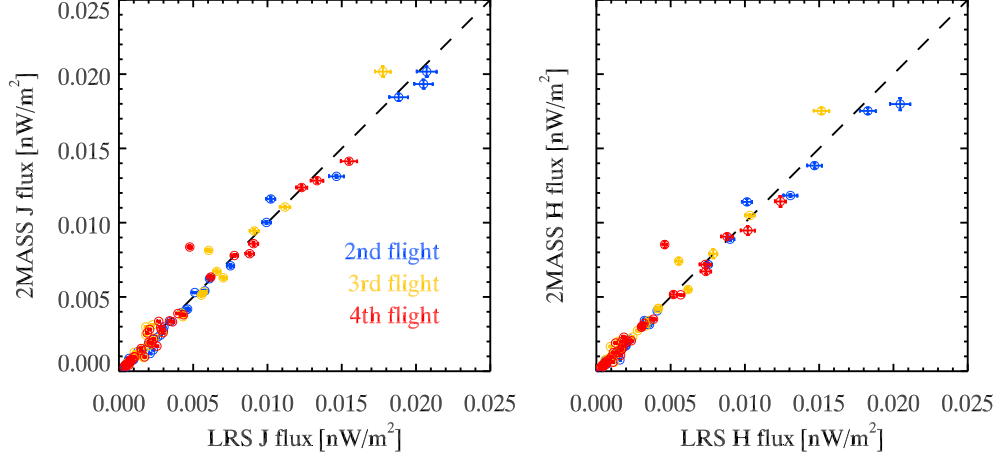


Figure 2.9 The 2MASS J- and H-band fluxes are shown as a function of the LRS J- and H-band. Each color represents the data obtained during different flights. Slit apodization effect is corrected for all LRS stars. Correction factor is derived based on the slit simulation for magnitude ranges covered by the LRS stars as shown in Figure 2.11 and Figure 2.12.

puting the mean distance between LRS and 2MASS coordinates of all matched stars. The error corresponds to 1.5 times the pixel scale. We check the validity of astrometric solutions by comparing the colors and fluxes between the LRS and matched 2MASS stars. In Figures 2.10 and 2.9, we show the comparison of the  $J - H$  colors and fluxes of the cross-matched stars in each field. Here, we multiplied LRS fluxes at J- and H-band by 2.22 and 2.17, respectively, to correct for the slit apodization. On the whole, they match well within the error range.

### 2.6.3 Star identification

The bright lines dispersed in the spectral direction in the background-subtracted images are candidate star spectra. To calculate the spectrum of candidate sources,

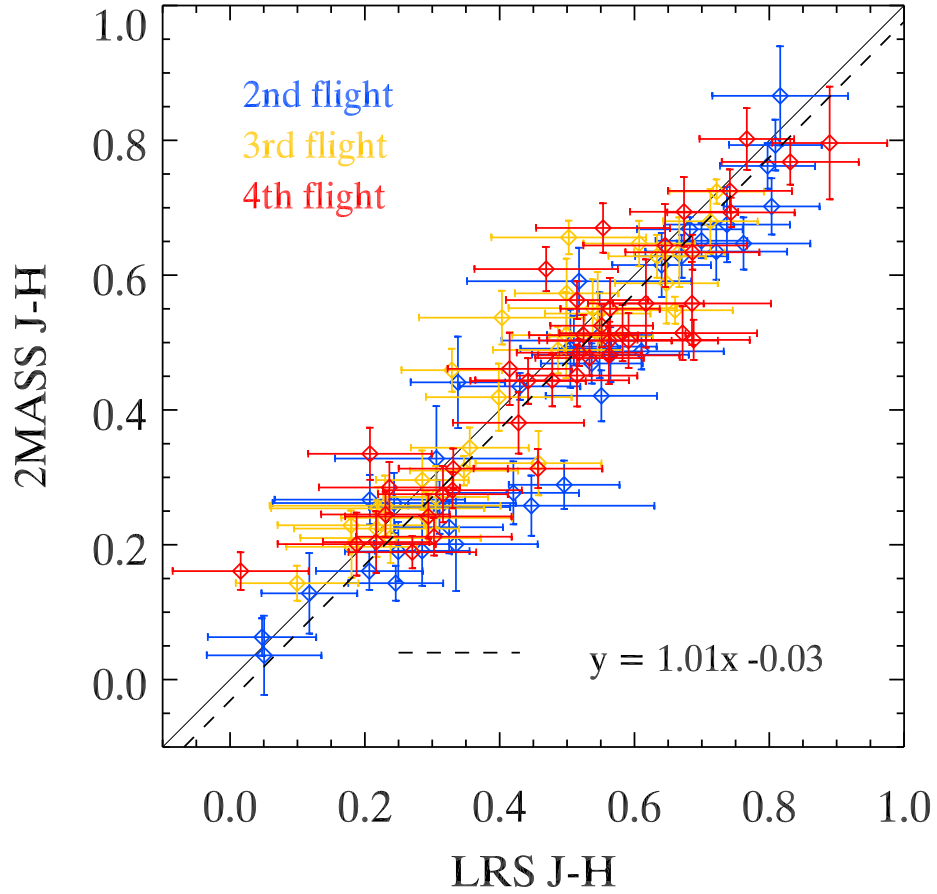


Figure 2.10 The LRS J-H color comparison with cross-matched 2MASS J-H color. Each color corresponds to a different flights. The dashed line shows a linear fit, exhibiting a slight systematic offset from unity. The J-H colors of LRS stars are conserved regardless of slit apodization effect.

we simply isolate individual lines of emission and map the pixel values to wavelength using the ground calibration. However, this procedure is complicated both by the extended spatial PSF of the LRS and source confusion.

To account for the size of the LRS spatial PSF (FWHM  $\sim 1.2$  pixels), as well as optical distortion from the prism that spreads the star images slightly in the imaging direction, we sum 5 rows of pixels in the imaging direction for each candidate star. Since the background emission has already been accounted, this sum converges to the total flux as the number of summed rows is increased. By summing 5 rows, we capture  $> 99.9\%$  of a candidate star’s flux. The wavelength of the spectral bins are calculated from the corresponding wavelength calibration map in the same way.

From these spectra, we can compute synthetic magnitudes in the  $J$  and  $H$ -bands, which facilitate comparison to 2MASS measurements. We first convert surface brightness in  $nWm^{-2}sr^{-1}$  to flux in  $nWm^{-2}sr^{-1}$ , and then integrate the monochromatic intensity over the 2MASS band, applying the filter transmissivity of the  $J$  and  $H$ -bands (Cohen et al. 2003). To determine the appropriate the zero magnitude, we integrate the  $J$  and  $H$ -band intensity of Vega’s spectrum (Bohlin & Gilliland 2004) with same filter response. The  $J$  and  $H$ -band magnitudes of each source are then calculated, allowing both flux and color comparisons between our data and the 2MASS catalog.

Candidate star spectra may comprise the blended emission from two or more stars, and these must be rejected from the catalog. Such blends fall into one of two categories: (*i*) stars that are visually separate, but are close enough to share flux in a 5 pixel-wide photometric aperture, and (*ii*) stars that are close enough that their images overlap so as to be indistinguishable. We isolate instances of case (*i*) by comparing the fluxes calculated by summing both 3 and 5 rows along the imaging direction for each source. If the magnitude or  $J - H$  color difference between the two apertures is larger than the statistical uncertainty, we remove those spectra from the

catalog. To find instances of case (ii), we use the 2MASS star catalog registered to our images using the procedure described in Section 2.6.2. Candidate sources which do not meet the criteria presented below are rejected.

To ensure the catalog spectra are for isolated stars rather than indistinguishable blends, we impose the following requirements on candidate star spectra: (i) each candidate must have  $J < 11$ ; (ii) the  $J$ -band magnitude difference between the LRS candidate and the matched 2MASS counterpart must be  $< 1.5$ ; (iii) the  $J - H$  color difference of the LRS candidate star and the matched 2MASS counterpart must be  $< 0.3$ ; and (iv) among the candidate 2MASS counterparts within a  $500''$  ( $= 6$  pixel) radius of a given LRS star, the second-brightest 2MASS star must be fainter than the brightest one by more than 2 magnitudes at J-band. Criterion (i) excludes faint stars that may be strongly affected by residual backgrounds, slit mask apodization, or source confusion. The second and third criteria mitigate mismatching by placing requirements on the magnitude and color of each star. In particular, the  $J - H$  color of a source does not depend on the slit apodization or position in image space (see Figure 2.10), so any significant change in  $J - H$  color as the photometric aperture is varied suggests that more than a single star could be contributing to the measured brightness. Finally, it is possible that two stars with similar  $J - H$  colors lie close to one another, so the last criterion is applied to remove stars for which equal-brightness blending is an issue. Approximately one in three candidate stars fails criterion (iv).

In addition, 3 of LRS candidate stars are identified as variables in the SIMBAD database <sup>2</sup>. We also identify 2 stars as binary and multiple-star system, and 4 high proper motion stars. Through these stringent selection requirements, we conservatively include only the spectra of bright, isolated stars in our catalog. Finally, 105 star spectra survive all the cuts and are selected as catalog members.

---

<sup>2</sup><http://simbad.u-strasbg.fr/simbad/>

## 2.6.4 Result and discussion

### Slit effect simulation

Due to the slit apodization effect, the incoming stellar flux is reduced while passing through the LRS slit. The synthesized LRS magnitudes thus become fainter than the original stellar magnitudes. Since the CIBER did not point stars during observation, this effect occurred randomly depending on the position of a star against the slit. To estimate the effect, we performed an empirical simulation as follows. For each 2MASS star matched with LRS candidate, we made a point source image convolving with LRS PSF. Instrumental noise and source confusion from faint stars beyond limiting magnitude are added. By applying the slit mask and moving it along an arbitrary direction, we estimate the apodized magnitudes as a function of slit position. Figure 2.11 and 2.12 shows the simulations drawn with shaded color. Points with error bars show flux ratio between the LRS and 2MASS counterparts. They are fall within the shaded region. Since the faint LRS stars can be easily affected by background noise either from statistical uncertainties or nearby faint stars, the flux ratio fluctuate bigger than other bright stars. Here, we multiplied LRS fluxes at J- and H-band by 2.22 and 2.17, respectively, to correct for the slit apodization.

The simulation shows LRS stars identified for each flight with different color. The mean value of the 4th flight agrees well with that of other flights. There exists no biases between flights. This indicates that we can apply 3rd flight calibration factor to calibrate 4th flight data.

### Duplicate observations

Serendipitously, of 110 stars, 5 stars are observed twice in two different flights. Among those, 4 stars are observed from 2nd and 3rd flight while 1 star is observed from 2nd and 4th flight. Although there exist only 1 star, it enables us to check

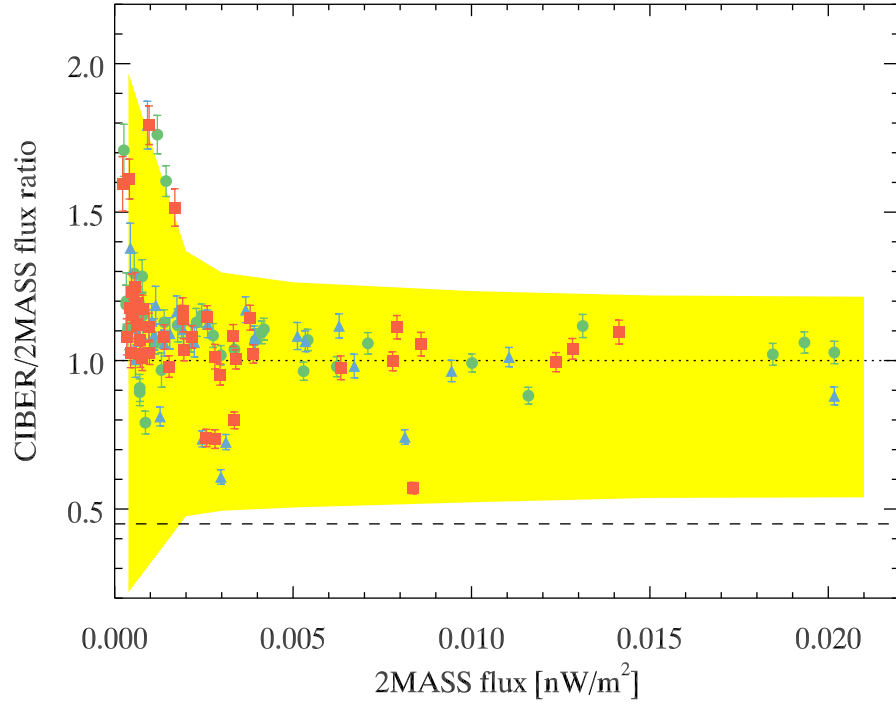


Figure 2.11 Flux ratios of all LRS stars to the matched 2MASS stars in J-band. Each color represents stars observed from each flight. Since the LRS flux is apodized by the slit mask, an aperture correction has been made to yield ratio unity in ideal case (dotted line). The averaged original flux ratio is drawn with dashed line where the reciprocal of it is used for aperture correction. The shaded color shows the range of relation we expect from an instrument simulation, representing an upper and lower bound of the absolute calibrations of the LRS.

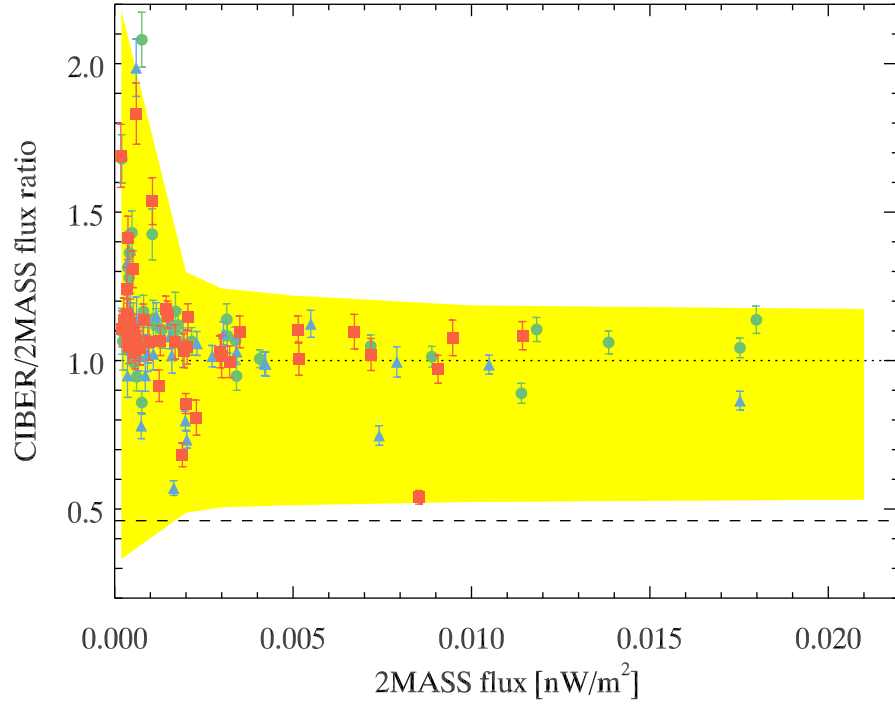


Figure 2.12 Flux ratios of all LRS stars to the matched 2MASS stars in H-band. Each color represents stars observed from each flight. Since the LRS flux is apodized by the slit mask, an aperture correction has been made to yield ratio unity in ideal case (dotted line). The averaged original flux ratio is drawn with dashed line where the reciprocal of it is used for aperture correction. The shaded color shows the range of relation we expect from an instrument simulation, representing an upper and lower bound of the absolute calibrations of the LRS.

4th flight calibration. Figure 2.13 shows the spectra comparisons for 5 stars. The extracted spectra for a star observed from 2nd and 4th flight show well consistency below  $1.6 \mu\text{m}$ . The discrepancy can be explained by calibration error which it affects little variation to the NIREBL.

## 2.7 Absolute brightness measurement

After the validation of the flux calibration, we can measure the absolute brightness of the NIREBL for wavelength ranges from  $0.8$  to  $1.7 \mu\text{m}$ . Here we describe brief introduction of the data process and the result. The content of this Section is submitted to ApJ (Matsuura et al.).

### 2.7.1 LRS data analysis

The NIREBL measurement has been done using the 2nd and the 4th data. The 1st flight data was contaminated much by thermal emission from the rocket skin and the airglow was significantly affected during the 3rd flight. As shown in Figure 2.14, the LRS detector uses multiple sampling. Until the reset signal is on, the signal increases linearly with time. The brighter signal masks steeper increment. In each pixel, we performed linear fit and the slope is assigned to a pixel as a photocurrent ( $\text{e}^{-1}\text{s}^{-1}$ ). Figure 2.7 shows the intensity map derived through this process. In the same manner, dark current is measured by averaging the signal from masked region in the detector (see Figure 2.7). Dark was then subtracted for each pixel.

In order to extract NIREBL from the processed image, we subtracted all known foregrounds which is categorized into two: resolved and diffuse sources. The resolved source is bright galactic stars and unresolved sources are ZL, DGL, and ISL above limiting magnitude ( $J_{Vega} \sim 11$ ). We first remove bright galactic stars using sigma clipping method. The star mask process is described in Arai et al. (2015). Left



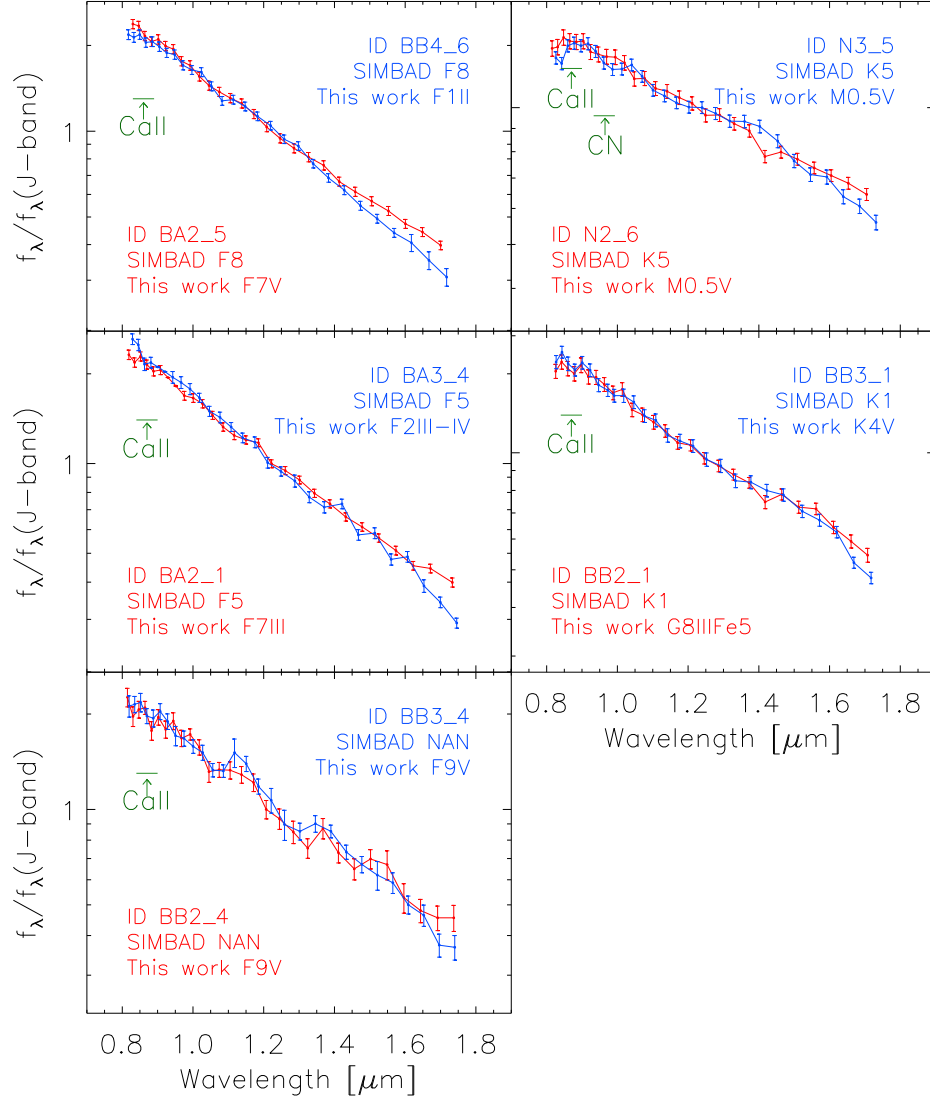


Figure 2.13 Five stars are serendipitously observed in two independent flights. Each panel shows two spectra extracted from each flight. Detailed information of each star is in Table 3 from Kim et al. (2017).

bottom panel of Figure 2.8 shows the star removed map. The intensity of masked pixel  $\lambda I_{\lambda}^{\text{mask}}$  can be expressed as:

$$\lambda I_{\lambda}^{\text{mask}} = \lambda I_{\lambda}^{\text{ZL}} + \lambda I_{\lambda}^{\text{ISL}} + \lambda I_{\lambda}^{\text{DGL}} + \lambda I_{\lambda}^{\text{NIREBL}}, \quad (2.3)$$

where ZL, ISL, and DGL are diffuse foreground components. The brightness of each component is determined both from observation and model. The detailed description of foreground estimation is in Matsuura et al. (submitted to ApJ). The  $\lambda I_{\lambda}^{\text{NIREBL}}$  is then calculated by subtracting all foregrounds from  $\lambda I_{\lambda}^{\text{mask}}$ .

### 2.7.2 Result and discussion

By combining the 2nd and the 4th flight data, we firstly measure the excess NIREBL spectrum at around  $1 \mu\text{m}$  based on the ZL model from Kelsall et al. (1998). As shown in Figure 2.15, the NIREBL spectrum shows broad excess emission between  $0.8$  to  $3 \mu\text{m}$  with peak at  $1.5 \mu\text{m}$ . It decreases slowly towards shorter wavelengths and rather rapidly towards longer wavelength. The surface brightness level of excess NIREBL is  $26.6 \text{ nWm}^{-2}\text{sr}^{-1}$  at  $1.4 \mu\text{m}$  which is significantly brighter than the IGL. Our NIREBL brightness shows discrepancy with the NIREBL estimated from  $\gamma$ -ray measurements (H.E.S.S. Collaboration 2013) which sets the upper limit of NIREBL brightness. Since the  $\gamma$ -ray approach is also based on the theoretical model to estimate the NIREBL brightness, we need more observational results with a wide range of redshifts.

Dwek et al. (2005) argued that the spectrum of the ZL is similar to the NIREBL measured from IRTS/NIRS (Matsumoto et al. 2005, 2015) and COBE/DIRBE (Gorjian et al. 2000). Based on the CIBER/LRS measurement, we found that the color changes between the NIREBL and the ZL at shorter wavelength region. The NIREBL from the CIBER/LRS shows redder spectrum than the ZL which indicates that the ZL is not the excess origin. To ensure our result, we use another ZL model (i.e.

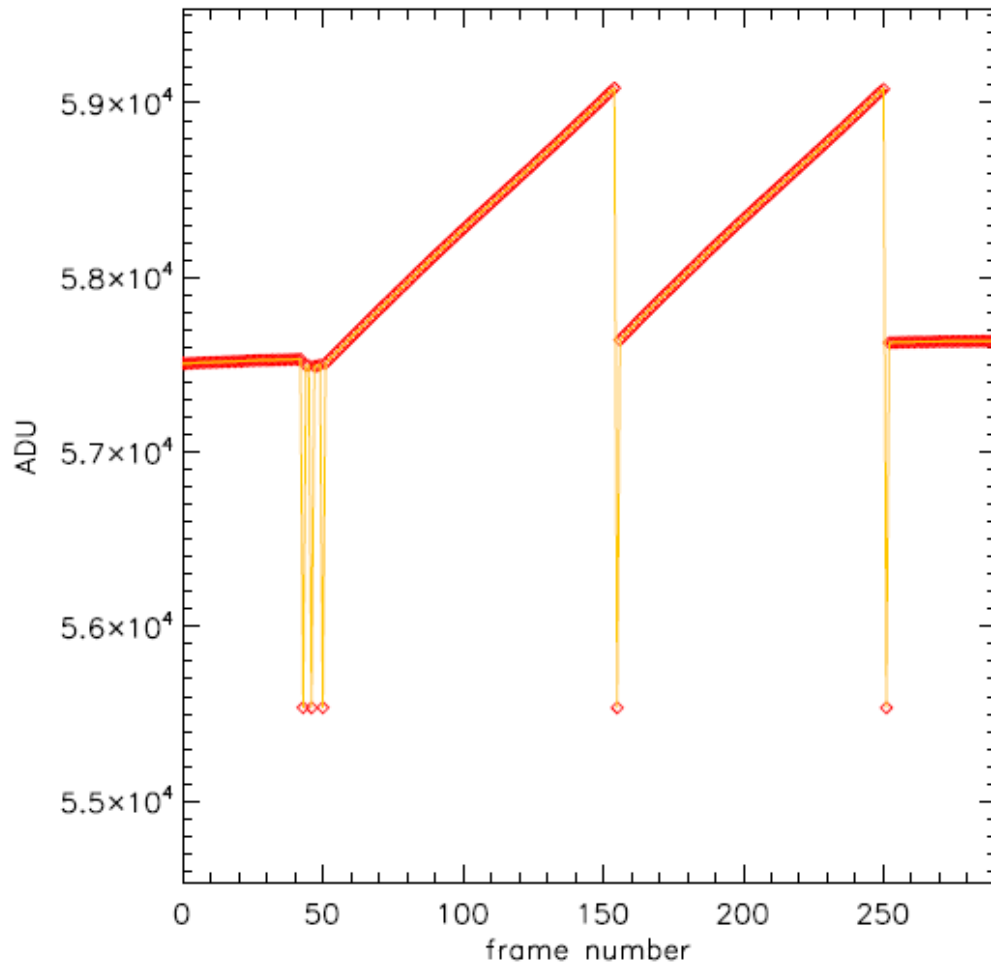


Figure 2.14 Schematic diagram of multisampling. Incident signal is integrated over frames before reset signal on.

Wright 2001). However, we exclude the Wright model since the estimated NIREBL shows unphysical value (i.e. negative or smaller than the IGL brightness).

In addition, we assume the worst case of ZL brightness to check the significance of the excess NIREBL. We scale the ZL brightness to make NIREBL same level as IGL for wavelength ranges between 0.8 and 1  $\mu\text{m}$ . Even after the exaggerated ZL brightness, significant excess NIREBL is observed above 1.5  $\mu\text{m}$ .

## 2.8 New insights from fluctuation measurements of the CIBER

The CIBER team also investigated the spatial fluctuation using two telescopes in the CIBER payload. They are I- and H-band Imagers. The result is published in the SCIENCE (Zemcov et al. 2014). Figure 2.16 shows the result auto spectra for I- and H-band. The total amplitude of foregrounds somewhat under predicts the observed amplitude between multiple moment  $l$  from 500 to 2000 and the small angular scale is dominated by known galaxy population. Three models are examined to explain the results: first stars, IHL, and DCBH. We exclude DCBH since it is expected to show Lyman break at longer than the CIBER bands and the DCBH shows very different color and amplitude comparing with our measurements. Furthermore, neither the IHL nor the first stars fit the observed H(1.6 $\mu\text{m}$ )-Spitzer(3.6 $\mu\text{m}$ ) color as shown in Figure S26 (Zemcov et al. 2014). One reason for the discrepancy can be absence of nonlinear clustering term for the IHL which considers the scale dependent distribution of dark matter haloes or we definitely need new populations.

Zemcov et al. (2014) converted the RMS fluctuation ( $500 < l < 2000$ ) to intensity assuming model-dependent contrast factor as shown in Figure 2.19. Comparing with other telescope measurements converted into intensities, the I- and H-band results do not follow Rayleigh-Jeans spectrum well. The I- and H-band show lower and higher

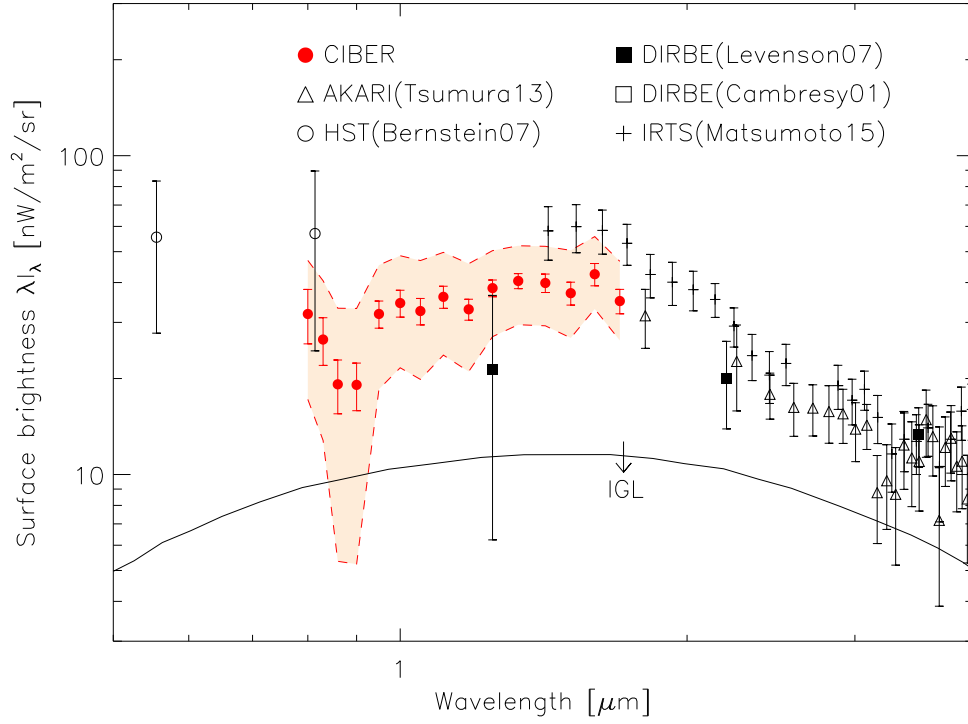


Figure 2.15 The NIREBL spectra for the CIBER/LRS drawn with red shaded error. Extragalactic background intensities measured from various observations are also drawn. Black solid line is IGL inferred from AEGIS galaxy-SED-type (Dominguez et al. 2011). The NIREBL measurements from previous studies are plotted with error bars. They are the IRTS (Matsumoto et al. 2015), AKARI (Tsumura et al. 2013), HST (Bernstein 2007), DIRBE (Levenson 2007), and DIRBE (Cambresy 2001).

than nominal amplitudes, respectively. The brightness of the IHL is comparable to the IGL but the IHL shows much bluer color. Since it shows bluer than the first stars, we ruled out the first star as a dominant contributor.

On the other hand, Zemcov et al. (2014) perform the cross correlations of Spitzer ( $3.6 \mu\text{m}$ ) with each CIBER I-band and H-bands. They show significant correlations which represent the same sources contribute to wide wavelength range. Nevertheless, different source may also exist. Yue et al. (2013) made a correlation analysis between the Spitzer and the X-ray background which also shows significant correlation and suggests the dominant X-ray background source is DCBH. However, the CIBER bands cannot be explained by the DCBH since the redshifted DCBH radiation is expected to be seen at longer wavelength due to its distance ( $z > 12$ ).

Based on the Figure 2.16, the fluctuation spectra at larger angular scale ( $\theta > 1^\circ$ ) can be explained by the DGL. However, the DGL estimation was not accurate enough since they extrapolate the DGL power spectrum towards large angular scale with constant power. Furthermore, they used the dust map having low spatial resolution (Schlegel et al. 1998) for the DGL estimation. To investigate the precise DGL fluctuation, we used the AKARI/FIS image which achieved deep pointing observation at  $90 \mu\text{m}$  as shown in Figure 2.18. Since the AKARI/FIS is far-IR map, we scaled the intensity to near-IR using empirical scaling relation as described in Section 3.4.2. We then measure the power spectrum using publicly available tool named POKER<sup>3</sup>. Figure 2.18 shows the new estimation of the DGL. The spectrum shows turnover at  $l \sim 1000$  and decreases towards larger angular scales. The AKARI based DGL fluctuation has different spectral shape from the original DGL. If this is true, the CIBER measured fluctuation amplitude at the largest angular scale cannot be explained by the DGL but need additional source reside in the NIREBL.

---

<sup>3</sup><http://www.ipag.osug.fr/~ponthien/Poker/Poker.html>

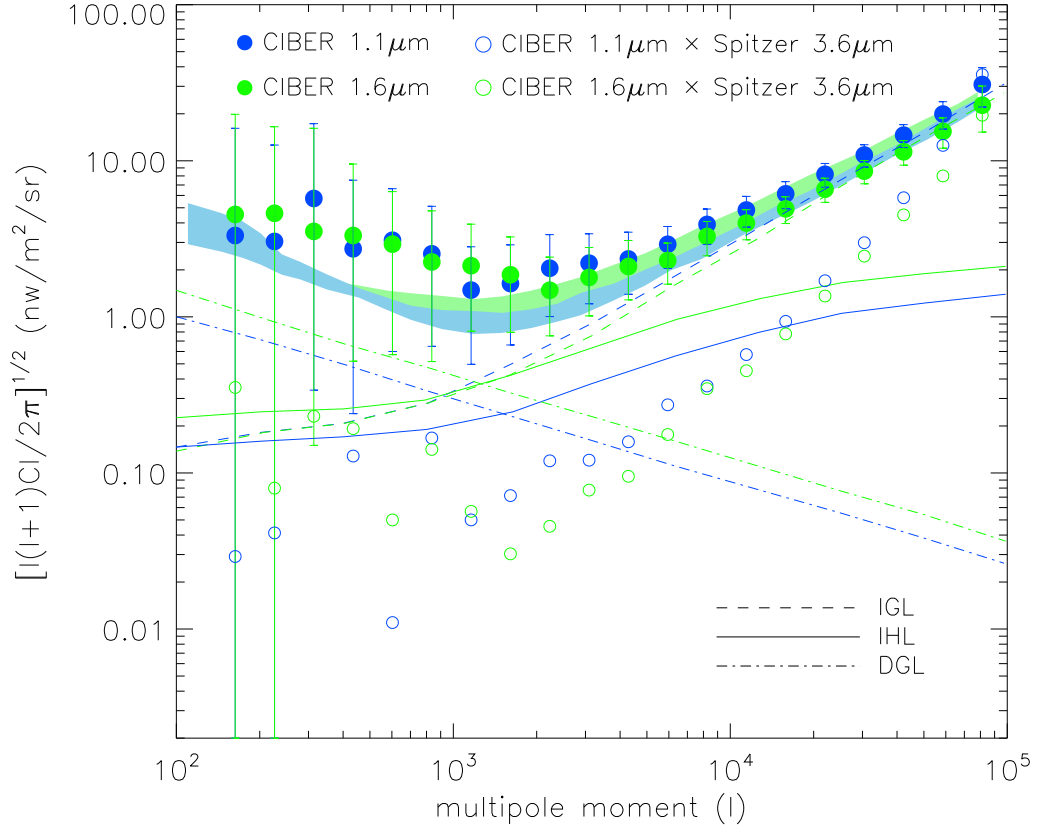


Figure 2.16 The CIBER auto spectra for I - and H-band are drawn with filled circle. Open circle is the cross spectra for Spitzer 3.6  $\mu\text{m}$  (Cooray et al. 2012) with each CIBER bands. Model spectra of IHL, IGL, and first star are drawn with solid, long-dashed, and dotted line, respectively. Short-dashed line is DGL spectrum. Sum of all astrophysical sources including flat-fielding error (not drawn here) is in shaded color. Blue and Green represent I- and H-bands.

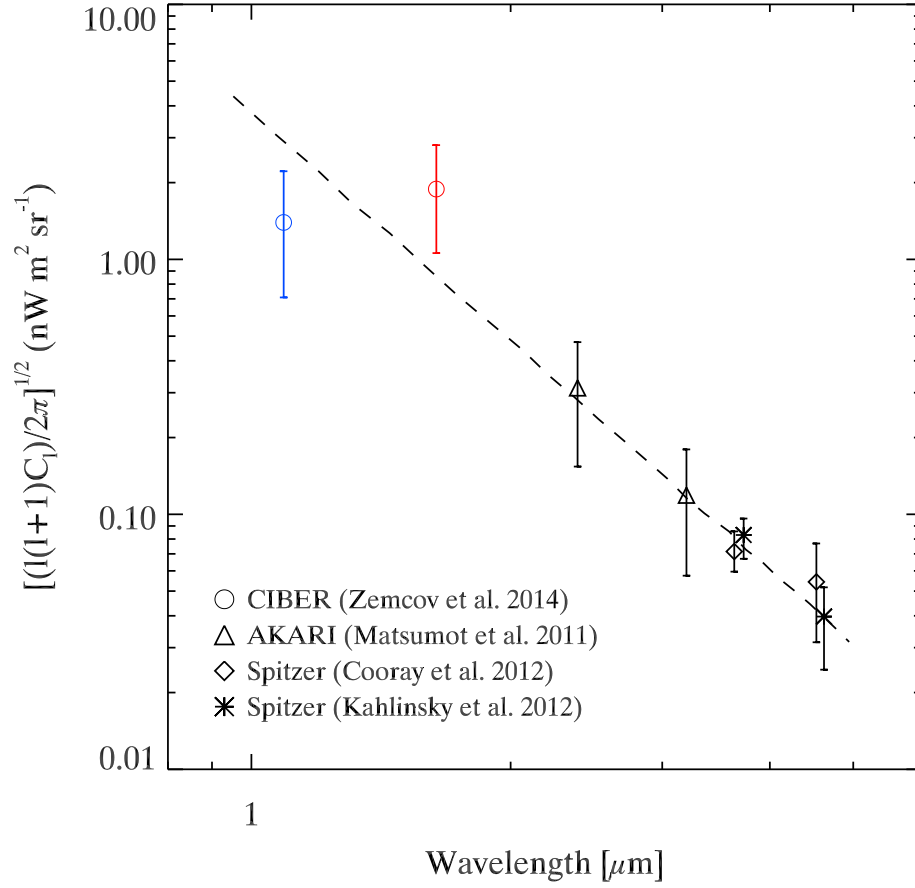


Figure 2.17 Intensities of excess fluctuation. Averaged fluctuation from  $l$  between 500 and 2000 is converted to intensities for the CIBER. I- and H-band are drawn in blue and red, respectively. The points for the AKARI, and Spitzer are calculated from  $l \sim 3000$ . Best-fit Rayleigh-Jeans spectrum for AKARI and Spitzer is drawn in dashed line.



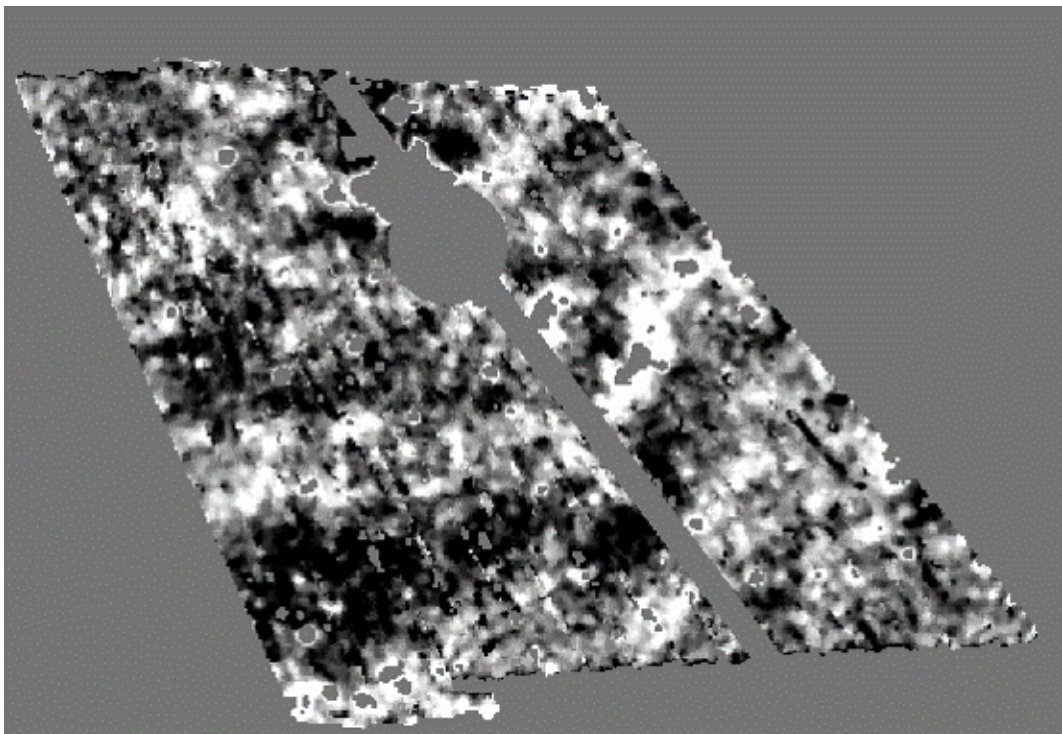


Figure 2.18 AKARI/FIS deep pointing image 90  $\mu\text{m}$  toward NEP field. Pixels shown with black are masked.

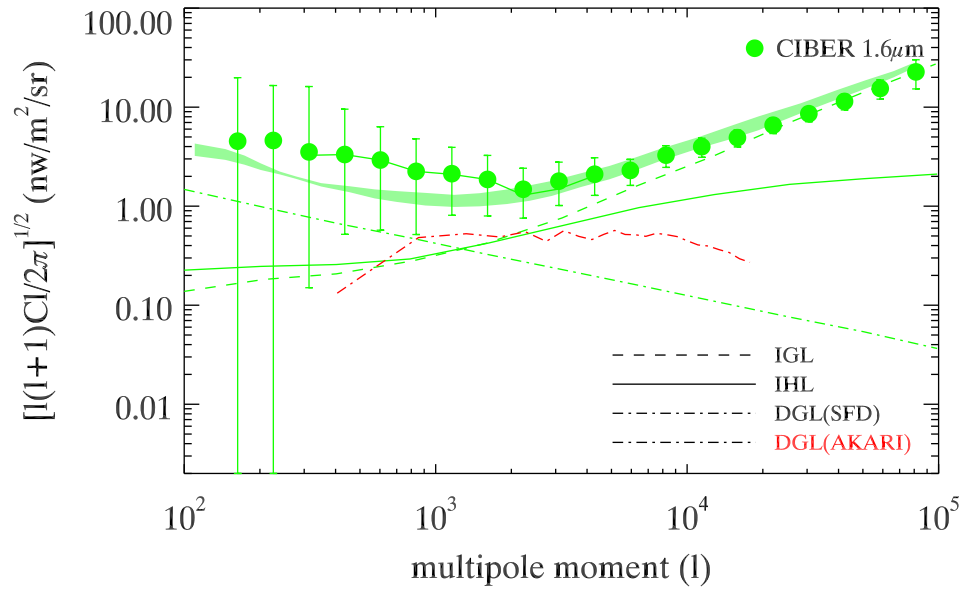


Figure 2.19 The CIBER H-band and DGL fluctuation spectra. The CIBER H-band fluctuation spectrum is drawn in green with other foreground components. Red represents our new DGL estimation from AKARI high resolution map.



## Chapter 3

# Large angular scale fluctuations with IRTS data

### 3.1 Overview

Previous studies including the CIBER reveal that the excess emission and fluctuation are real signature from hidden background origin. However, due to the limited observation, the spatial fluctuation studies were performed only below  $1^\circ$ . The CIBER explains that the fluctuation spectra at larger angular scale ( $\theta > 1^\circ$ ) can be explained by the DGL. However, the DGL estimation was not accurate enough due to low spatial resolution of the dust map used for the CIBER data analysis. We investigate the DGL using higher spatial resolution map from the AKARI/FIS and the result shows somewhat different spectral feature over large angular scales. It decreases towards larger angular scale and does not affect amplitude above  $1^\circ$ . To investigate the excess fluctuation above  $1^\circ$  angular scales, we use the data observed from the IRTS. The manuscript of this Chapter will be submitted to the Astrophysical Journal.

### 3.2 IRTS instruments

IRTS is a Japanese first orbiting IR telescope onboard the Space Flyer Unit (SFU) launched on March 18 UT in 1995. It covers 7 % of Sky ( $2700 \text{ deg}^2$ ) until the liquid Helium is exhausted from March 29 to April 25 with scanning rate of  $3.82' \text{ s}^{-1}$  (Murakami et al. 1996). The IRTS is 15-cm Ritch-Chretien type telescope and has 60-cm focal length (Onaka et al. 1994). Four focal plane instruments are installed on IRTS and cryogenically cooled down to 2 K with liquid Helium. They are Near-Infrared Spectrometer (NIRS), Mid-Infrared Spectrometer (MIRS), Far-Infrared Line Mapper (FILM), and Far-Infrared Photometer (FIRP). Of those, the NIRS is optimized for the diffuse background study with widest sky coverage to date.

The NIRS covers wavelength range between 1.4 and  $4.0 \mu\text{m}$  with  $0.13 \mu\text{m}$  spectral resolution. The incident beam enters the  $1.4 \text{ mm} \times 1.4 \text{ mm}$  slit and diffracted by grating. The dispersed beam is then focused on the detector into 24 InSb linear arrays where each array has order-sorting band-pass filter. The optical path is shown in Figure 3.1. To reduce background errors arose from Galactic stars, it has higher spatial resolution than COBE (i.e. beam size =  $8' \times 8'$ ). To study background, NIRS has cold shutter to obtain the dark current and detector stability is monitored using calibration lamp during the observation. It used J-FET charge integrating amplifiers for detecting low background brightness by reducing the noise and achieving high sensitivity. The InSb detector read outs the data with 4 Hz sampling rate at  $\sim 2 \text{ K}$  operating temperature. Charges are integrated for 65.54 sec before a reset and 8.192 sec of it is used for dark current observation with shutter close configuration. To maintain the linearity, the dynamic range of detector is controlled. Details of NIRS performance can be found in Noda et al. (1996).

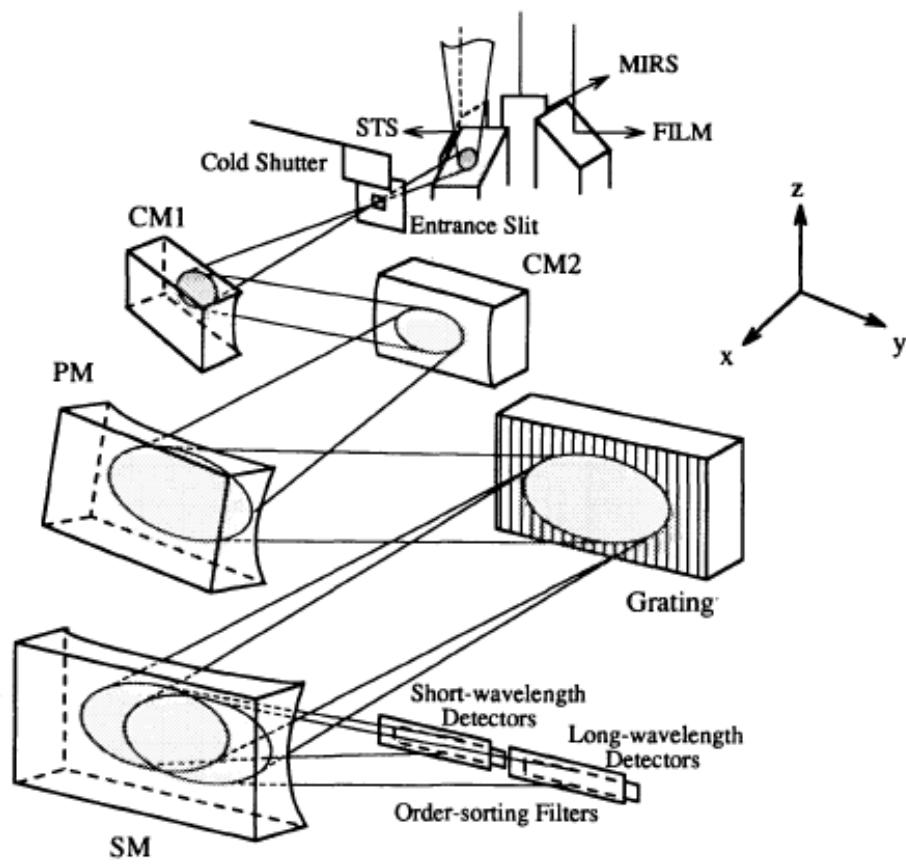


Figure 3.1 NIRS optical path. The incident beam through entrance slit is dispersed by grating and focused on detector.

### 3.3 Observation and data reduction

Figure 3.2 shows the whole scanned area of the IRTS as well as the coverage used for this study. It has two scan modes. South and north scans denote pointing directions in celestial coordinate during the day light time. The scan modes are changed by flip maneuver. To avoid the strong galactic foregrounds such as stars and dusts, we used data obtained during south scan mode where the observation achieved galactic latitude above  $40^\circ$ . Due to contaminations from OH emission for first half of mission, we collected NIRS data observed from latter 15 days before mission-ends. We also rejected data obtained while passing through South Atlantic Anomaly (SAA) region where the noise level increases by high energy charged particles. For 65.54 sec integration, we do not use first 4 sec data due to anomalous residual charges after reset. The flux (e-/s) of each NIRS data is then attained from linear fit of 5 sec along the scan direction. Since the telescope axis scans about  $20'$  in 5 sec, the beam is elongated along the great circle and the effective beam size become  $20' \times 8'$ . In linear fit process, we additionally exclude data contaminated by cosmic-ray, instrumental noise, and stars (Matsumoto et al. 2005) and dark is subtracted.

Astrometry was achieved within  $4'$  using attitude control sensor which is accurate enough to detect Galactic stars. Calibration has been done using standard stars observed by NIRS (Murakami et al. 2003). They compared 4 stars with Cohen's SED library which contains 180 stars with continuous spectra from 1.2 to  $35 \mu\text{m}$ . The calibration factor measured from laboratory and that derived from the observed stellar fluxes agrees very well. Finally, the absolute calibration was achieved with a few percent errors based on the inflight calibration (Noda et al. 1996).

In order to compare with other studies, we made H- and K-band fluxes from 24 discrete NIRS spectrum. Fluxes from 1.53, 1.63, and  $1.73 \mu\text{m}$  are averaged for H-band and fluxes from 2.03, 2.14, 2.24, and  $2.34 \mu\text{m}$  are averaged for K-band. After this process, about 50 % data are filtered out and the 7545 of 15208 data are

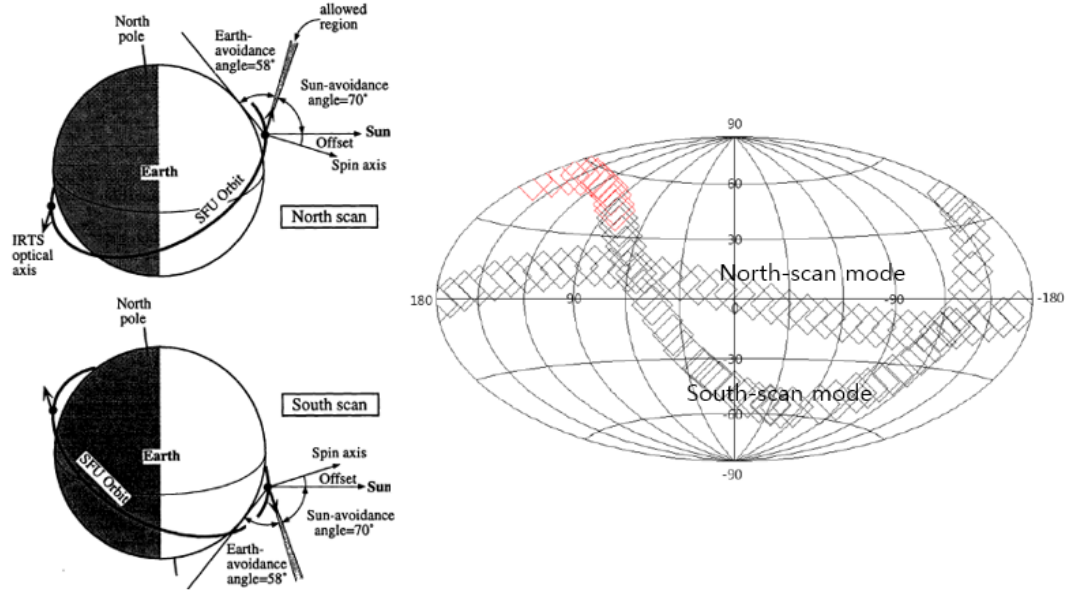


Figure 3.2 Left panel: IRTS attitude control modes. Right panel: IRTS scan path. Two stripes for two different scan modes. The red boxed region is used for this work. The selected fields are above  $40^\circ$  of Galactic latitudes.

remained.

### 3.4 Data analysis

The goal of data analysis is to make a pixel map to measure power spectrum. Since our data covers more than  $10^\circ$ , we cannot apply flat sky approximation for the fluctuation analysis (Kashlinsky et al. 2007). Therefore, we use Spherical Harmonic Transforms to avoid the distortion induced from projection onto sphere instead of Fourier Transform analysis. We use one of the pixelization schemes for spherical harmonic transforms, named HEALPix which stands for the Hierarchical Equal Area isoLatitude Pixelization. HEALPix divides the sphere into pixels with roughly equal shape and identical size. The pixelization is performed along the isolatitude which



has an advantage to reduce computational time for the spherical harmonic transform (Gorski et al. 2005). The resolution of the pixelization is defined by  $N_{side} = 2^k$ , where  $k$  is an integer from 0 to  $n$ . Because of its mathematical definition, we can only pixelize sky into fixed resolutions. By considering the NIRS beam size, we use  $N_{side} = 64$  where its pixel size is  $55' \times 55'$ . In this section, we describe how we estimated the brightnesses of NIRS and foregrounds such as ZL, ISL, and DGL based on the HEALPix format.

### 3.4.1 NIRS data analysis

We pixelize the NIRS data into HEALPix scheme. The  $N_{side}$  of 64 divides the sky into 49152 pixels with FoV of each HEALPix pixel  $0.84 \text{ deg}^2$ . As shown in Figure 3.3, each pixel is comprised of 10 to 400 NIRS data. The value of each HEALPix pixel is assigned from mean of the NIRS data belonged to it. The HEALPix pixels uncovered by the NIRS were masked to  $-1.6375e+30$  (i.e. bad pixel indication in HEALPix). The pixelized H- and K-band maps are then stored in FITS format (Calabretta & Greisen 2002) for the next step to evaluate power spectrum.

### 3.4.2 Foregrounds estimation

If we can observe the universe outside of our Galaxy, only extragalactic objects are there. Some of them are resolved by telescope and the others are shining as diffuse emission. However, since it is not possible to observe the universe outside of our Galaxy, we have unavoidably observe Galactic and Solar system foregrounds that need to subtract for the background study. Fortunately, the foreground brightnesses can be estimated using well validated model. In this section, we describe the methods used for the foregrounds estimation for the NIRS fields.

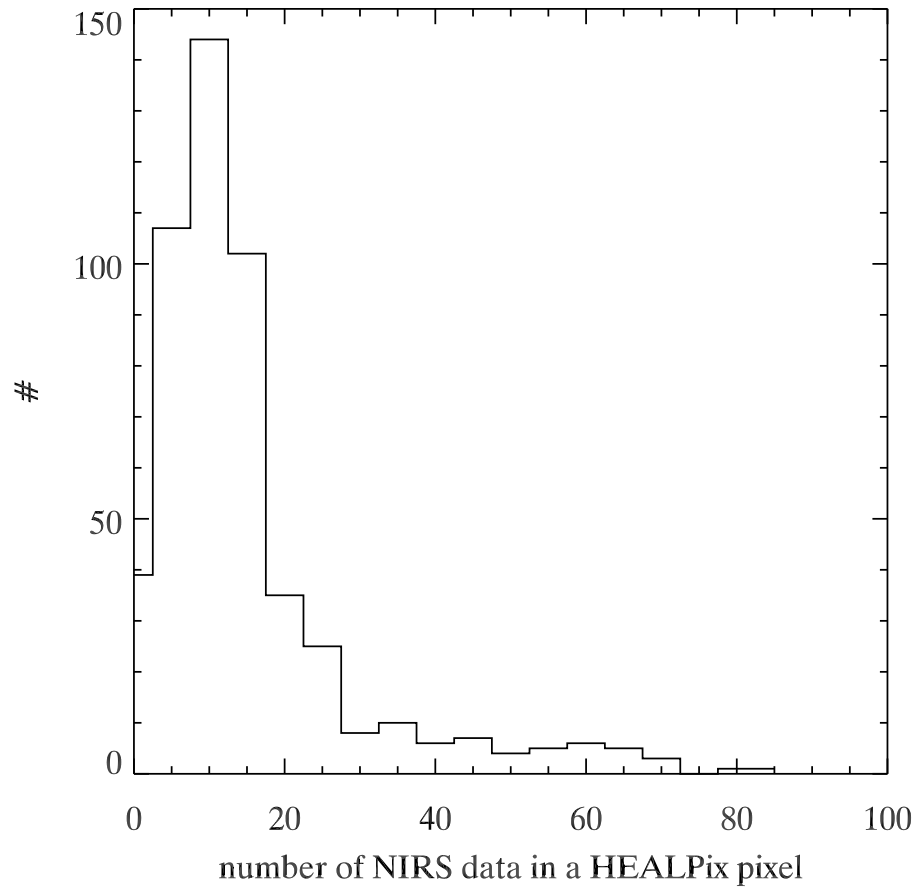


Figure 3.3 Histogram of the NIRS pixel numbers used for each HEALPix pixel bin. Here, the bin width is 5.

## Zodiacal Light

The ZL in near-IR is scattered sun light from IPD in solar system. IPD is composed of asteroid and comets. Since the Sun light illuminate the dust particles, the comparable wavelength to the size of the dust particles are scattered to be seen as ZL. Therefore, the ZL spectrum resembles spectrum of the Sun. Nevertheless, the brightness of ZL varies with time due to movements and collisions of asteroid or comets as well as Earth revolution around the Sun which we call seasonal variation. Therefore, the ZL depends on the IPD model. Kelsall et al. (1998) made 3D model including smooth cloud, dust band, and circumsolar ring components. The brightness of ZL is then estimated by integrating the density along the line of sight. The largest fraction is comprised with smooth cloud and other two (i.e. dust band, and circumsolar ring) are dusts reside in asteroid and dust captured by Earth gravity.

To estimate the ZL, we need position and observation time. For each NIRS point, we derive brightness of the ZL at K-band ( $2.2 \mu\text{m}$ ) based on the Kelsall model (Kelsall et al. 1998) using ZL modeling tool written in IDL. Finally, by scaling the solar spectrum (ASTM G173-03 Reference System <sup>1</sup>) to the K-band brightness, we obtain the ZL model brightnesses for the NIRS bands assuming the ZL spectrum is same as solar spectrum.

However, the assumption needs a correction. Matsumoto et al. (2015) studied correlation between the ZL model and observed data as shown in Figure 3 in that paper. For 1010 data, they plot the ISL and DGL subtracted surface brightness in vertical axis and ZL model brightness in horizontal at a given wavelength. The brightness in vertical axis corresponds to the brightness of isotropic background plus ZL. If the ZL model brightness is consistent with observed one, the y-intercept is equal to NIREBL and the slope must be the unity. However, the result slope is a little higher than the unity. The deviation represents the discrepancy between the

---

<sup>1</sup><http://rredc.nrel.gov/solar/spectra/am1.5/astmg173/astmg173.html>

model and the solar spectrum. We, therefore, multiplied the slope by ZL model brightness at each NIRS bands to get correct ZL brightness.

### Diffuse Galactic Light

DGL is emitted from interstellar radiation field which is scattered star light from dust grains distributed in interstellar space. In near-IR, however, we have no direct detection of DGL due to strong other foregrounds. Fortunately, the brightness of the DGL has correlated with far-IR thermal emission (e.g. 100  $\mu\text{m}$ ) and H1 or CO column density (Brandt & Drain 2012). By cross correlating brightnesses of far-IR and near-IR after subtraction of other foregrounds, Arai et al. (2015) derive scaling factor between near-IR and far-IR (see Figure 3.4).

At each NIRS position, we obtained the 100  $\mu\text{m}$  intensity. Using the conversion factor provided by Arai et al. (2015), we scaled the brightness of 100  $\mu\text{m}$  map to DGL brightness for NIRS spectral bands. The conversion factor used in this process is tabulated in Table 3.1. We then averaged DGL spectrum of NIRS bands into H- and K-band. The H- and K-band fluxes are then pixelized into HEALPix map. However, the DGL brightness shows difference with model (Zubko et al. 2004) by a factor of 2 (Arai et al. 2015). Therefore, the systematic error induced from the difference is estimated as described in Section 3.5.

### Integrated Star Light

Stars are distributed all around in our Galaxy that we cannot avoid when observing the NIREBL. Since the SEDs of stars are different with their spectral types, energy contribution to the sky spectrum depends on the spectral types of sources. For instance, hot stars and white dwarfs emit most their energy in UV, main sequence stars in visible, and IR from late type of stars. Thanks to the advanced infrared telescopes (e.g. 2MASS, WISE), almost all bright galactic stars were identified and

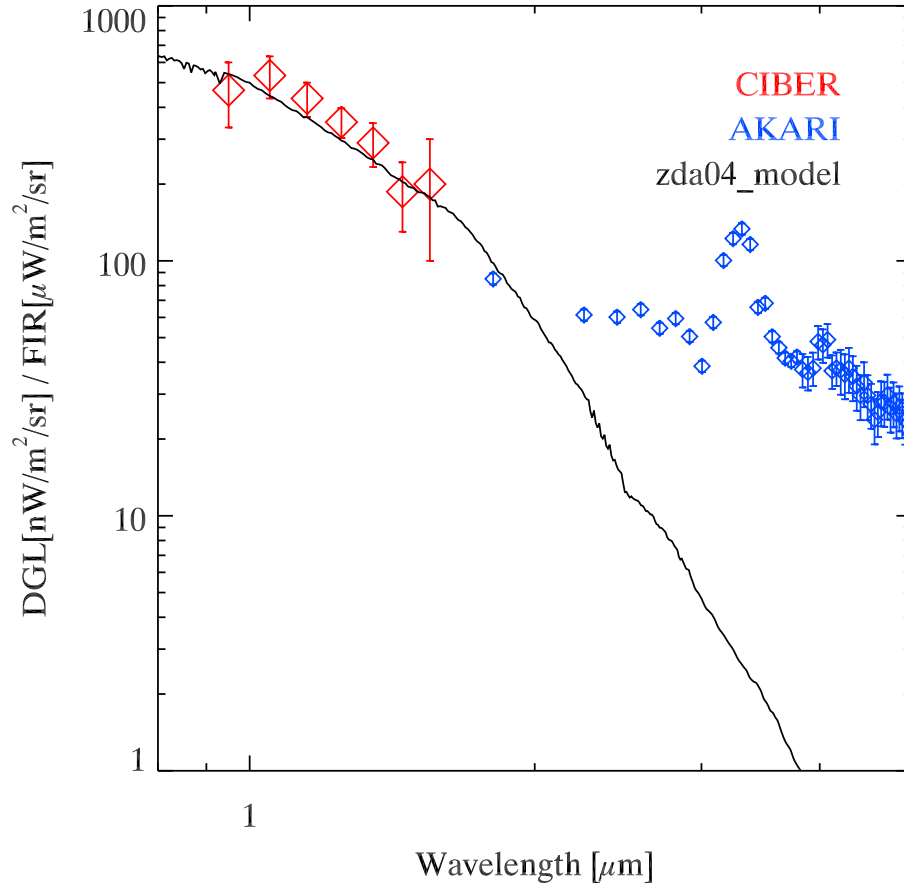


Figure 3.4 DGL spectrum. Vertical axis corresponds to the scaling factor to derive DGL intensities. The CIBER/LRS is from (Arai et al. 2015), AKARI is from Tsumura et al. (2013), and DGL model to fit the CIBER/LRS data is drawn with solid line (Brandt & Draine 2012).

Table 3.1. DGL scaling factor

Wavelength ( $\mu\text{m}$ )	DGL( $nW m^{-2} sr^{-1}$ )/100 $\mu\text{m}(\mu W m^{-2} sr^{-1})$
1.53	184.21
1.63	154.87
1.73	121.9
2.03	54.161
2.14	40.722
2.24	31.32
2.34	23.032

archived. Cross matching with point sources enables ones to find and mask pixels contaminated by bright stars. However, there still remains unresolved faint stars distributed in our Galaxy due to detection limit of telescope. These stars can be estimated from sky model such as SKY (Wainscoat et al. 1992) and TRILEGAL (Girardi et al. 2005) using the Galaxy model. They estimate the number of stars and their brightnesses in various wavelengths. One can thus calculates the brightness of integrated star light for any line of sight directions in our Galaxy.

The NIRS data contaminated by bright Galactic stars were initially removed. Therefore, NIRS data contains unresolved brightnesses from faint Galactic stars. The limiting magnitude of NIRS depends on the wavelength as shown in Figure 3.5. We use the TRILEGAL model to estimate the brightness from the integrated star light along the line of sight from the limiting magnitude to faint-end magnitude generated by the model (i.e.  $\text{mag} < 30$ ). The TRILEGAL model generates model stars at a given position and FoV based on the Galaxy model (i.e. Halo, Bulge, Disk, etc.). It gives us physical information of stars including their magnitudes for any interesting bands.

For each NIRS observed position and FoV, we run the TRILEGAL code to obtain

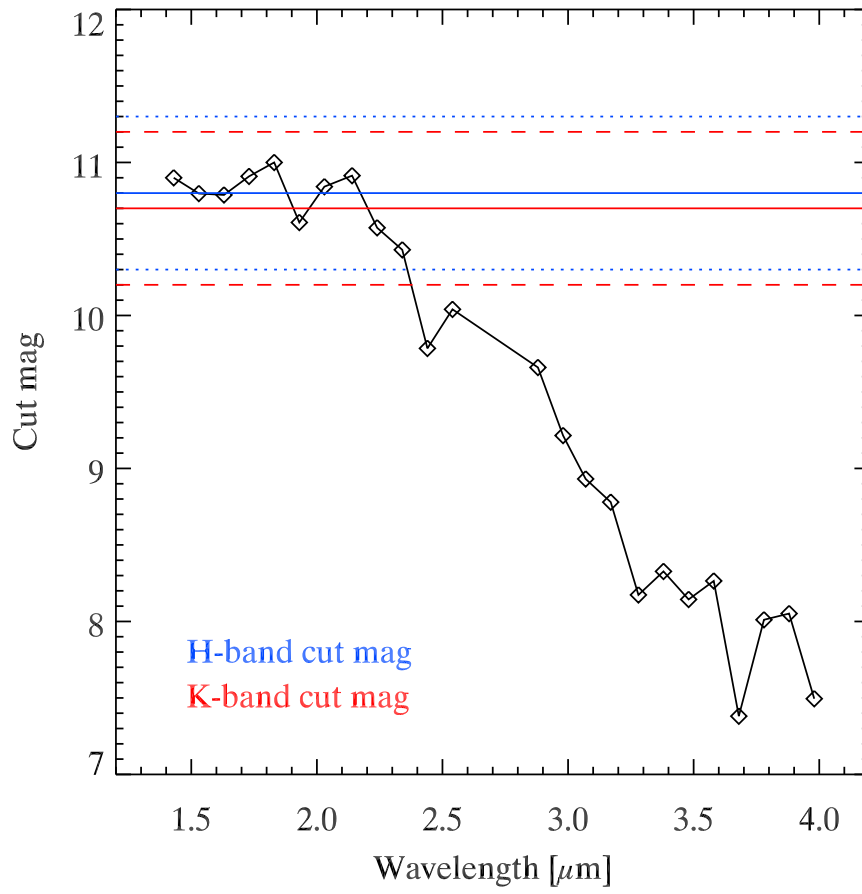


Figure 3.5 Limiting magnitudes for the 24 NIRS bands (diamond). Red and blue solid lines are the H- and K-band cutoff magnitudes used to estimate the unresolved brightness of Galactic stars.  $\pm 0.5$  of cutoff magnitude errors are drawn in dashed lines.

model stars for H- and K-bands. To reduce the statistical error, the TRILEGAL was run 50 times. To check the validity of TRILEGAL model, we compared the brightness of the H- and K-band ISL for stars fainter than NIRS limiting magnitude using 2MASS point source catalog. However, since the 2MASS limiting magnitude is brighter than the TRILEGAL, we add TRILEGAL stars fainter than 2MASS limiting magnitude. The Figure 1 in Matsumoto et al. (2015) shows the comparison between the TRILEGAL model and 2MASS plus TRILEGAL faint stars. They show clear correlation but 2MASS ISL shows systematically higher than TRILEGAL result which needs model correction by a factor of 1.23. Therefore, we multiplied the correction factor by TRILEGAL ISL to obtain the final ISL for both H- and K-band. The derived ISL for each pixel is then pixelized into HEALPix format.

### Deep Galaxy Count

The NIREBL is the unresolved sources either by distance or faintness of the origins. Therefore, a fraction of the NIREBL brightness is accounted by faint or distant normal galaxies which is not accessible with current telescope. However, since the limiting magnitude of current telescope reaches almost faint-end  $m_J=28$  (Keenan et al. 2010), the portion of the unresolved galaxies contribute to the NIREBL seems to be very low. Even in bright galaxies, their contributions on power spectrum at large angular scale is negligible and dominant in small angular scale (sub-degree). Since the NIRS covers large angular scales, we simply use 2MASS extended source catalog where the limiting magnitude is not much deeper than other observations. Of 2MASS extended catalog, we integrated brightnesses of all galaxies belonged to each HEALPix pixel and HEALPix map for H- and K-bands are generated.



### 3.5 Power spectrum analysis at large angular scale

Using HEALPix map for each component and band derived in previous section, power spectrum is measured. The power spectrum is an expression of relative brightness distributions as a function of angular scales ( $\theta$ ) or multipole moments ( $l$ ). The relative brightness of each map is

$$\delta I(\theta, \phi) = I(\theta, \phi) - \langle I(\theta, \phi) \rangle, \quad (3.1)$$

where  $\theta, \phi$  is angular position of the sky. If the background is observed for whole sky with no masked region, the brightness distribution  $\delta I(\theta, \phi)$  can be expanded in spherical harmonics as

$$\delta I(\theta, \phi) = \sum_{l=0}^{\infty} \sum_{m=-l}^l a_{lm} Y_{lm}(\theta, \phi) \quad (3.2)$$

where

$$a_{lm} = \frac{1}{\Omega_{obs}} \int d\phi \int \sin\theta d\theta \delta I(\theta, \phi) Y_{lm}^*(\theta, \phi) \quad (3.3)$$

Here,  $Y_{lm}(\theta, \phi)$  is laplace spherical harmonics,  $a_{lm}$  is multipole coefficients of the expansion, and  $\Omega_{obs}$  is solid angle of each pixel. The  $l$  equal 0 is monopole and  $l$  equal 1 is dipole terms. Then, the power spectrum  $C_l$  is expressed as below.

$$C_l = \frac{1}{2l+1} \sum_{m=-l}^l |a_{lm}|^2 \quad (3.4)$$

However, since parts of the sky is observed from NIRS, we need correction for the incomplete sky which is appeared as bias in the power spectrum. There are two popular methods to measure power spectrum for incomplete sky coverage: maximum likelihood estimation (Bond et al. 1998; Tegmark 1997) and pseudo power spectrum estimation (Hivon et al. 2002). For NIRS power spectrum analysis, we use publicly

available PolSpice software<sup>2</sup>(Chon et al. 2004) based on the pseudo power spectrum analysis. Here, *Pseudo* means that the isotropy assumption is broken. The PolSpice does correction for partial sky map with low computational cost.

To measure the true power spectrum, we calculate  $a_{lm}$  from  $\delta I(\theta, \phi)$  map. Then, the pseudo power spectrum for incomplete sky coverage is calculated from equation 3.4. The pseudo power spectrum  $C_l$  is then converted to correlation function

$$\xi(\eta) = \frac{1}{4\phi} \sum_{l=0}^{\infty} (2l+1) C_l P_l(\cos\eta) \quad (3.5)$$

where  $\xi(\eta)$  is expanded form as legendre series from

$$\xi(\eta) = \langle \delta I(\theta, \phi) \delta I(\theta', \phi') \rangle \quad (3.6)$$

Finally, the true power spectrum is derived by inverse operation of equation 3.5.

$$C_l = 2\phi \int_{-1}^1 \xi(\eta) P_l(\cos\eta) d(\cos\eta) \quad (3.7)$$

In order to measure true power spectrum using PolSpice tool, we prepare the two maps in HEALPix format. One is the brightness map for each component generated from previous section and another is a mask map having 1 for covered sky and 0 for uncovered sky. To estimate the NIREBL power spectrum, we generated the background map by subtracting all foreground components from preprocessed image in Section 3.4.2. However, instrumental noise such as photon noise and readout noise is also resided in the map. Since we don't know the noise level for each pixel, we performed Monte Carlo simulation to estimate the noise power spectrum. From Matsumoto et al. (2015), we adopted the I(H) [ $nWm^{-2}sr^{-1}$ ] band readout noise and photon noise FWHM of 4.59(1.48), 2.38(0.85), respectively. Readout and Photon noises are then summed in a quadrature to be total error of 4.80(2.53). We, then,

---

<sup>2</sup><http://www2.iap.fr/users/hivon/software/PolSpice/>

made a gaussian distribution having FWHM as same as total error. Since pixels of HEALPix has random noise following the gaussian distribution, we randomly pick value in the distribution and assign it in each HEALPix pixel. Repeat this until filling the all HEALPix pixel covered by NIRS and applied same mask used for NIRS data analysis. Then, power spectrum is estimated for the mask applied random noise map. This procedures were repeated 100 times and averaged to estimate final noise power spectrum. The noise power spectrum is then subtracted from the background power spectrum directly for each band.

The finite resolution and pixelization can suppress power spectrum at small angular scale. The suppression is corrected using beam transfer function. Figure 3.6 shows the beam transfer function for NIRS elongated FoV normalized to unity at small angular scale. Since the function does not decrease until  $2^\circ$ , we did not consider beam transfer function in our analysis. We also measured the power spectrum for each astrophysical component. They are plotted in Figure 3.7 with error bars. The ZL shows the largest amplitude. The shaded color shows NIREBL auto spectra for comparison.

Errors can be categorized into two: Random and systematic errors. Random errors include 3 % NIRS calibration error, ISL error from the NIRS limiting magnitude, DGL error, HEALPix binning error, and sample variance. We apply 3 % of NIREBL brightness as calibration error. To derive ISL error, we calculate the ISL brightness for lower and upper bound of the NIRS limiting magnitude. It is  $\pm 0.5$  mag from nominal limiting magnitude. The calculation is performed with same procedure for the ISL estimation described in Section 3.4.2. DGL error is reported from Arai et al. (2015). By comparing the DGL model with observed data, they found the scaling factor from far-IR to near-IR has 20 % error. To estimate the DGL error in our power spectrum, we derive the DGL brightness using scaling factor applied with 20 % error and calculate its power spectrum. HEALPix binning error is the

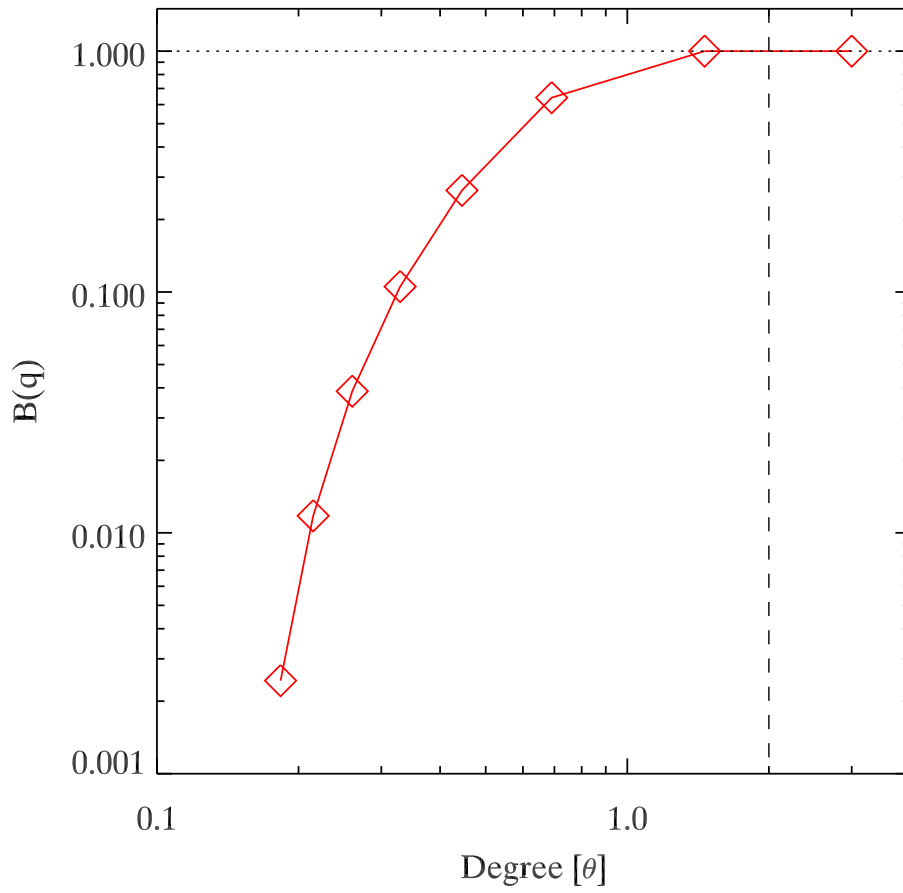


Figure 3.6 Beam transfer function of the NIRS PSF (beam size =  $20' \times 8'$ ). The estimated power spectrum is normalized to unity at large angular scale. The dashed line indicates  $\theta = 1.5^\circ$  where the power spectrum converges to unity.

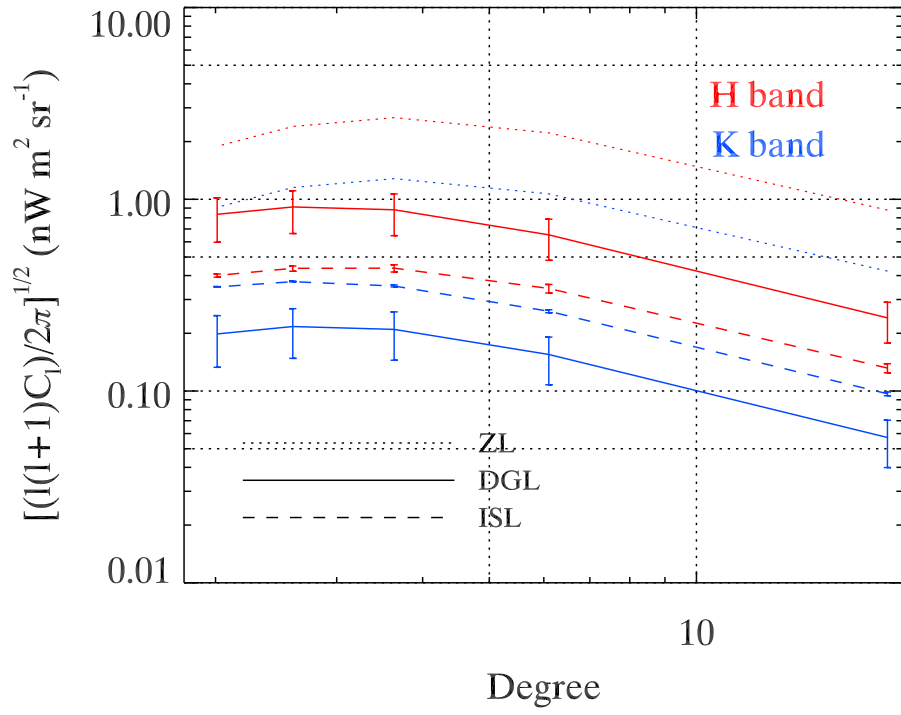


Figure 3.7 The measured foregrounds auto spectra for the NIRS. H- and K-band is drawn in red and blue, respectively. The ZL, DGL, and ISL are drawn in dotted, solid, and dashed lines, respectively. Shaded colors are NIREBL auto spectra with errors for the comparison purpose with other foregrounds.

1  $\sigma$  of the NIRS brightness in a HEALPix pixel. The sample variance is the error induced from power spectrum estimation. At a given angular scale, the number of possible modes are limited due to the finite sky coverage. The smaller the angular scale, larger the number of possible modes and reduces the sample variance. Systematic error is induced from ISL model which shows discrepancy of 1.23 factor with ISL estimated from the 2MASS. We multiplied 1.23 factor to the nominal ISL and estimated the power spectrum. Final error is then combined in a quadrature. Figure 3.8 and Figure 3.9 show the H- and K-band errors for each component.

### 3.6 Result and discussion

We firstly measure the fluctuation spectrum at the largest angular scales above  $1^\circ$  in H- and K-band as shown in Figure 3.10 and Figure 3.11. The fluctuation spectrum ranges from  $2^\circ$  to  $20^\circ$ . We compare our result with previously measured auto spectra at smaller angular scales ( $< 1^\circ$ ). However, since other studies were measured at different wavelength bands, scaling has been done by assuming they follow Rayleigh-Jeans. They are AKARI ( $2.4 \mu\text{m}$ ), Spitzer ( $3.6 \mu\text{m}$ ), and CIBER ( $1.6 \mu\text{m}$ ). We multiplied scaling factors of 1.68(AKARI), 22.80(Spitzer), 0.18(CIBER) to the original power spectra to compare them with the K-band (i.e.  $2.2 \mu\text{m}$ ) IRTS power spectrum. The scaling factors are estimated from Rayleigh-Jeans spectrum fitted to the AKARI and Spitzer (see Figure 2.19). Power spectra from the AKARI and the Spitzer are marginally agree and the Spitzer is extended to larger angular scales. The discrepancy between the CIBER and other measurements (i.e. Spitzer and AKARI) denotes contributions of NIREBL origins are different depending on the wavelengths. Interestingly, the Spitzer fluctuation diverges more than 10 times of resolved galaxies out to  $1^\circ$  (Kashlinsky et al. 2012). Although angular scales between the IRTS and the others (e.g. AKARI, Spitzer, CIBER) were not measured to date, we can expect the fluctuation peaks at around  $1^\circ$ .

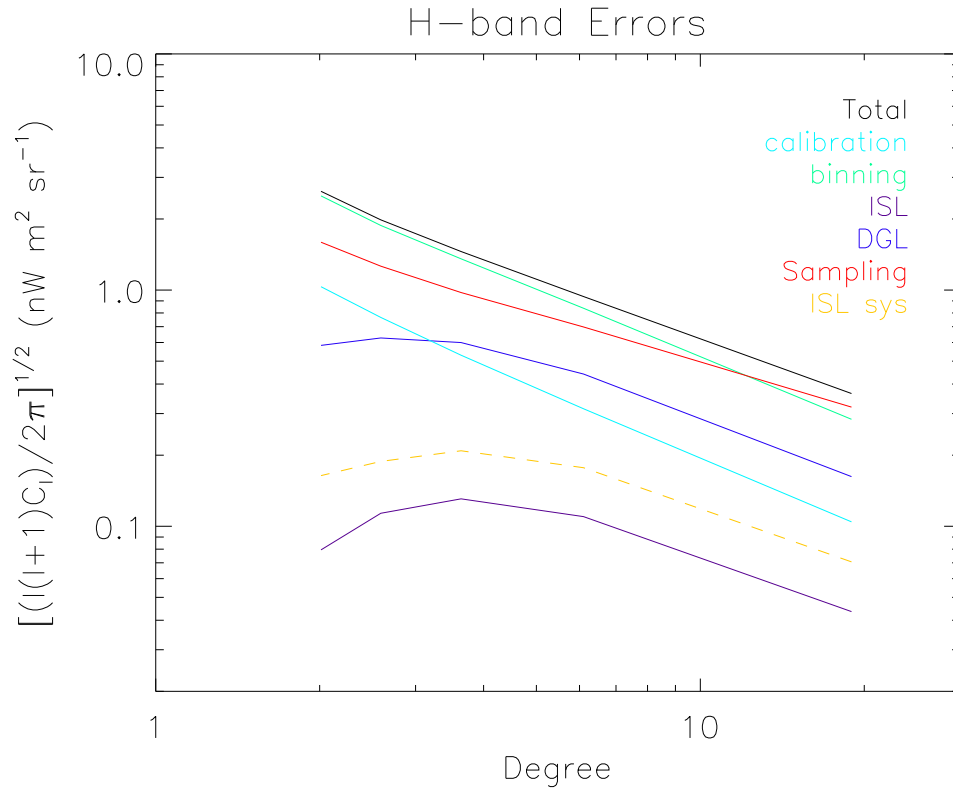


Figure 3.8 H-band fluctuation errors. Statistical errors are drawn in solid line and systematic error is in dashed line. Each error is indicated with different colors and quadrature summed total error is shown in black.

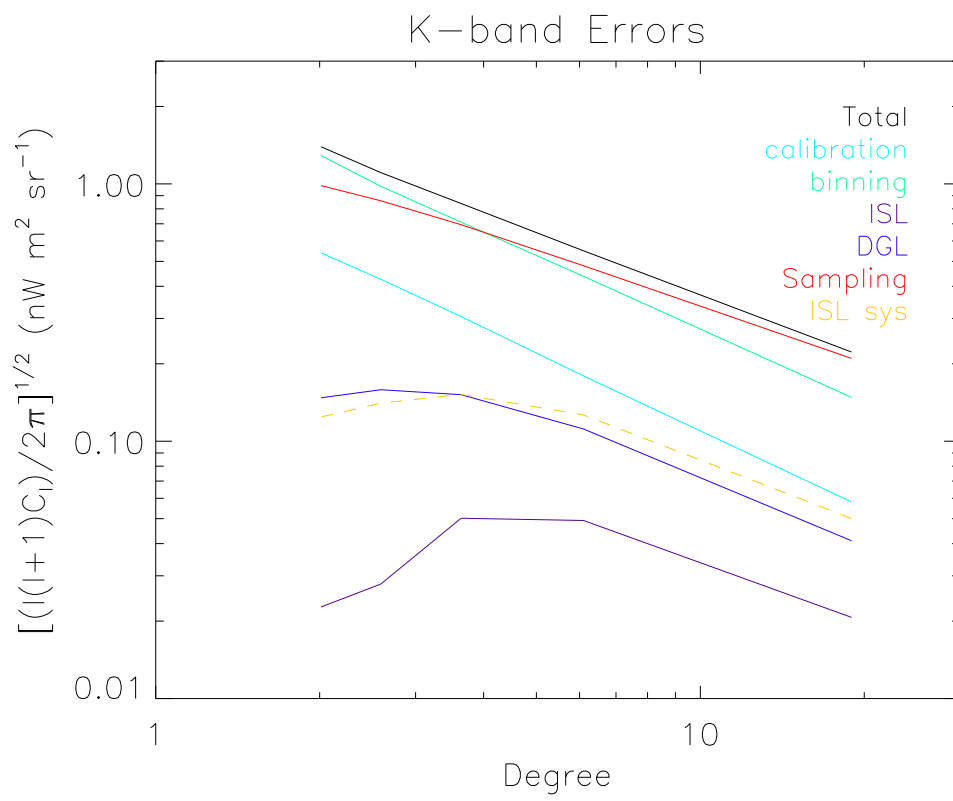


Figure 3.9 K-band fluctuation errors. Color code is same as Figure 3.8



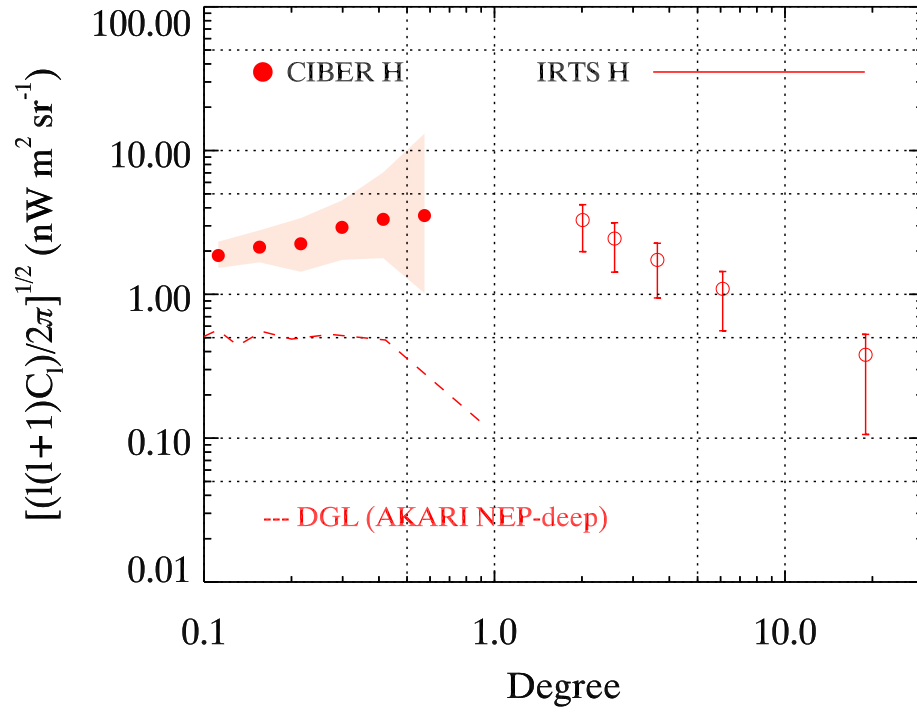


Figure 3.10 The measured H-band auto spectrum for the IRTS/NIRS. CIBER/Imager and IRTS/NIRS auto spectra are drawn in red circle and solid line, respectively. The shaded colors denote corresponding errors. Dashed line is DGL spectrum measured using the AKARI/FIS deep pointing data towards NEP region.

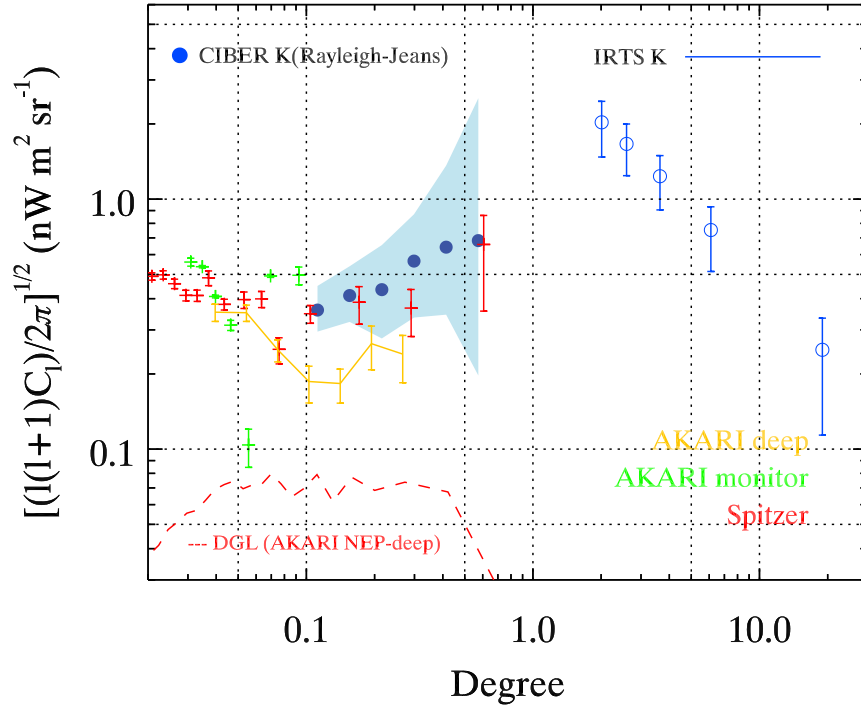


Figure 3.11 The measured K-band auto spectra for the IRTS/NIRS. The CIBER/Imager and IRTS/NIRS auto spectra are drawn in blue circle and solid line, respectively. The shaded colors denote corresponding errors. Cross points with errors are the AKARI ( $2.4 \mu\text{m}$ ) and Spitzer ( $3.6 \mu\text{m}$ ). All spectra except the IRTS/NIRS are scaled to K-band ( $2.2 \mu\text{m}$ ) assuming they follow Rayleigh-Jeans.

We performed cross correlation with other maps in different wavelengths using PolSpice. There are three categories: (i) NIRS and Planck 545Hz/857Hz cross correlation, (ii) NIRS and  $100\mu\text{m}$  (Schlegel et al.1998) cross correlation, and (iii) NIRS H- and K-band cross correlation. Planck and  $100\mu\text{m}$  data is mostly dominated by thermal dust. If we achieve significant cross correlation between the far-IR and the NIRS, the fluctuation in the NIRS can be explained by Galactic dust. Nevertheless, we found no correlation for (i) and (ii) case. In case (iii), the H- and K-band show excellent correlations as shown in Figure 3.12. This represents that the same origins are contributing to H- and K-band. Furthermore, they show significant correlation in brightness as shown in Figure 3.13. However, somewhat steep slope represents it does not follow Rayleigh-Jeans (i.e.  $\text{Flux} \sim \lambda^{-3}$ ). The discrepancy between slopes may denote origins of  $1^\circ$  peak is different from small angular scales.

The significant clustering at large angular scale cannot be explained by normal galaxies from deep galaxy count or luminosity function evaluation. Since normal galaxy contributes mostly on the small angular scale measurements (i.e. shot noise), increasing their number densities to explain large angular clustering also increase the amplitude at small angular scales. However, there exists no enough space for unresolved galaxies to account at small angular scales. This represents that the NIREBL origins, at least part of them, has different spatial distribution with normal galaxies. Cooray et al. (2012) models the Halo Occupation Distribution (HOD) governed by dark matter. It is described with one-halo and two-halo terms. One-halo term describes the clustering of baryonic matter inside one halo and two-halo term describes the correlations between individual halos. The IHL is composition of the one-halo and two-halo terms. Cooray et al. (2012) explained the excess fluctuation at small angular scale ( $\theta < 20'$ ) using the halo model. Although the relatively large angular scale is dominant with two-halo term, it decreases above  $1^\circ$  which rejects the IHL from NIRS measurement (see Figure 1 in Cooray et al. 2012).

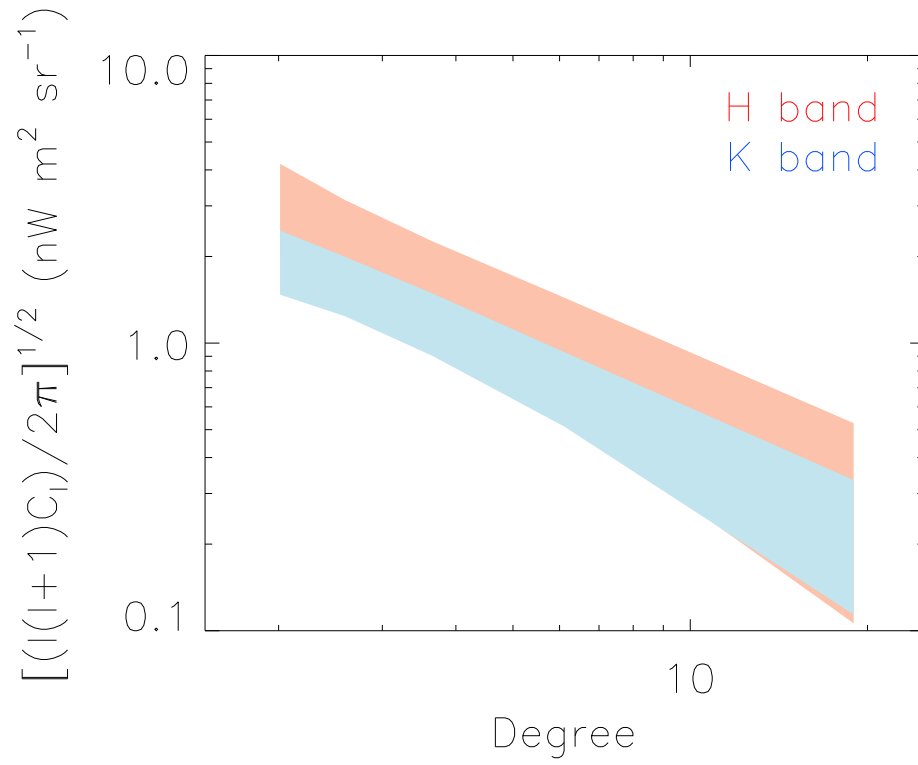


Figure 3.12 The NIRS cross spectrum. The shaded colors are the H- and K-band NIREBL fluctuations with errors drawn in red and blue, respectively. Black solid line is the H- and K-band cross fluctuation.

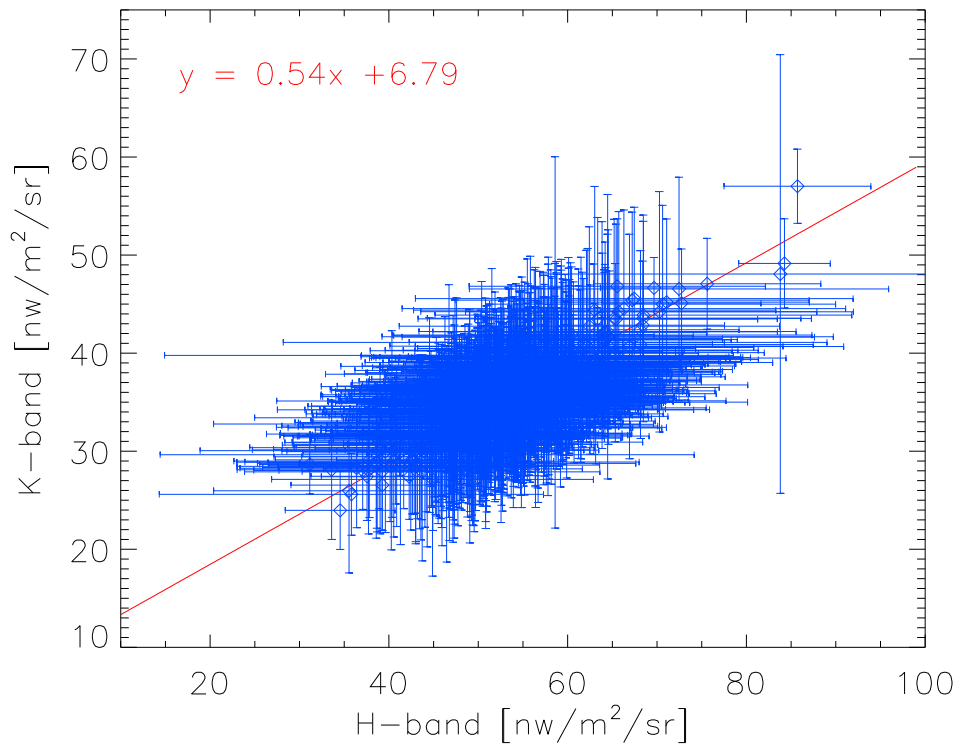


Figure 3.13 The correlation diagram between the H- and K-band NIREBL surface brightness. Blue points are the surface brightnesses of the NIRS NIREBL. The linear fit is drawn in red solid line with best-fit parameter.

## Chapter 4

# Summary and conclusions

In this dissertation, we have studied NIREBL to understand characteristics of their origins. Since current designed telescopes cannot directly detect the individual objects, we only can observe their integrated light from the early universe to the present. The integrated light can be studied in absolute brightness and spatial fluctuation. From absolute brightness measurement, we found the significant excess brightness using the CIBER/LRS with wavelength ranges from 0.8 to 1.7  $\mu\text{m}$  where the wavelength range was not covered before. The NIREBL spectrum is slowly decreases from peak at 1.5  $\mu\text{m}$  towards shorter wavelength and rather rapidly decreases towards longer wavelength. This can constrain the spectral energy from NIREBL origins although we currently rely on models. If the origin is from the first stars and Lyman break is at 0.8  $\mu\text{m}$ , the reionization was occurred from redshift  $z = 20$  and 6 with rest frame wavelength of Lyman  $\alpha$  is 121.5 nm. Second, the energy cannot be explained only by first stars but combinations with other sources. Current studies favor latter case. The hierarchical structure formation and evolution simulation in accordance with  $\Lambda\text{CDM}$  show that the star formation efficiency of first stars cannot explain the whole excess brightness (Bromm & Loeb, 2002).

However, there are two main controversial for the excess emission. One, Dwek

et al. (2005) argue that the NIREBL spectrum is similar to the ZL spectrum that the excess emission is simple subtraction error of the ZL. To clear the argument, we subtract artificially scaled ZL spectrum from the CIBER/LRS NIREBL spectrum. Even the worst case, the excess brightness is still shown significantly above  $1 \mu\text{m}$ . Furthermore, our NIREBL spectrum shows redder spectrum than ZL. This ensures the ZL brightness error cannot explain the excess brightness.

Second, we can indirectly infer the NIREBL brightness from  $\gamma$ -ray observation (H.E.S.S. Collaboration 2013). That is, the interaction between the  $\gamma$ -ray and NIREBL photon is appeared as attenuation in the blazar spectrum. The inferred brightness is close to the IGL level and shows large discrepancy with excess emission. However, two reasons make the excess NIREBL cannot be ruled out. First, due to difficulties to measure the blazar spectrum,  $\gamma$ -ray observation assumes the intrinsic blazar spectrum using theoretical SSC model. Second, secondary  $\gamma$ -ray photons can be produced by interacting with NIREBL or CMB photons and survive en route to the Earth. Since the  $\gamma$ -ray observation assumes the intrinsic blazar spectrum and measures the attenuation by interacting with NIREBL photons, the survived secondary photons make us to underestimate the NIREBL.

Based on the CIBER/Imager data at I- and H-band, Zemcov et al. (2014) examined the power spectrum out to  $1^\circ$  for the NIREBL. The result shows excess power at  $> 4.3'$ . Even using the theoretical models of the IHL, DCBH, and first stars, they cannot explain the excess power and needs new model or modifications of current models to fit the observed spectrum. The intensity estimated from fluctuation amplitude between  $500 < l < 2000$  shows comparable magnitude with the IGL but have much bluer spectrum. Thus, the result shows that the IHL can explain parts of the NIREBL brightness although it is faint to access with current designed telescopes.

According to the Zemcov et al. (2014), a parts of fluctuation amplitude at larger

angular scale ( $l < 500$  or  $\theta > 43.2'$ ) was initially explained with the DGL which was estimated from low resolution IRAS dust map (Schlegel et al. 1998). Although the observed fields are different, the CIBER shows significantly large amplitude of DGL fluctuation which contradicts with the DGL analysis from the AKARI and the Spitzer (Matsumoto et al. 2011, Kashlinsky et al. 2012). Based on the correlation analysis, the AKARI and the Spitzer demonstrate that there is no correlation between the NIREBL and the DGL. To validate the result, we estimate the DGL power spectrum using deep pointing AKARI/FIS image observed at NEP field. Since the image has high spatial resolution (pixel scale  $\sim 1.46' \times 1.46'$ ) and field covered at relatively high cirrus region, we can set upper limit of the DGL contribution. As a result, the fluctuation amplitude shows more than 10 times lower than the DGL from IRAS map and declined beyond  $0.5^\circ$  (see Figure 3.11).

If we neglect the amplitude of DGL emission, the excess emission at  $l < 500$  in the CIBER result is not negligible. However, relatively small CIBER FoV limits how the spectrum is shown at larger angular scales. Does it increase more towards large angular scale? Or does it decrease with no excess?

To evaluate the spectrum at larger angular scale, we analyze the IRTS data having the largest sky coverage with high sensitivity in near-IR to date. We found that the peak may appear at  $\sim 1^\circ$  although we have no current measurement at that angular scale. The peak at  $\sim 1^\circ$  was not predicted either from theories nor from observations. Since the CIBER does not have K-band to compare directly with the IRTS, we scaled its power spectrum to K-band assuming it follows Rayleigh-Jeans. The AKARI ( $2.4\mu\text{m}$ ) and the Spitzer ( $3.6\mu\text{m}$ ) results are also scaled in the same manner and compared. Both absolute brightness and spatial fluctuation show excess NIREBL and the brightness correlation shows somewhat steep slope which indicates that the IRTS does not follow Rayleigh-Jeans as well as the CIBER H-band. Since they are not resolved from current observation, it should be very faint and have



different spatial distribution to show significant clustering in spectrum beyond  $1^\circ$ . The peak corresponds to 10 Mpc at  $z \sim 0.15$ . However, it is unrealistic that such a specific population is distributed at a certain redshift.

Current theories and observations tried to explain the NIREBL origins with three candidates: first stars in early universe, IHL, and DCBH. However, none of those can explain current observation results (Cooray et al. 2012, Zemcov et al. 2014). There can be another NIREBL origin that was never observed before. One of those candidates is dark stars formed in early universe but radiate via annihilation of dark matter, WIMPs. Modeling by varying free parameters (i.e. formation rate, luminosity, spectrum, and effective lifetime) shows that the surface temperature of 7,500 K dark star can explain the NIREBL brightness (Maurer et al. 2012).

However, we have no obvious results yet. It either can be low- $z$  sources or high- $z$  sources. Kashlinsky et al. (2007) studied cross correlation between the residual Spitzer/IRAC (3.6, 4.5  $\mu\text{m}$ ) and the HST/ACS (B, V, i, and z bands) galaxies. They show no correlation. On the other hand, Bernstein et al. (2007) observed the excess brightness in visible bands using HST/WFPC2. Although the uncertainty is pretty large, the NIREBL is also contributed by sources at visible wavelength region. This indicates that different sources contribute between visible to near-IR wavelengths. If excess origin at near-IR is high- $z$  sources, the redshifted Lyman break of sources is much longer than the HST/ACS band. If it is low- $z$  sources, we can imagine they are extremely faint.

Several projects were proposed or proceeded to find more evidence in the NIREBL observation. They are CIBER-2, Multipurpose InfraRed Imaging System (MIRIS), and SPHEREx. The CIBER-2 is a successor of the CIBER-1. It has a 28.5-cm primary mirror inside a payload. The incident beam is then split into three cameras installed on the common optical bench. Each camera has six broad spectral bands from visible to near-IR (i.e. 0.6, 0.8, 1.03, 1.28, 1.55, 1.85  $\mu\text{m}$ ). It uses  $2048 \times 2048$

HAWAII-2RG arrays. Parts of each detector are used for fluctuation analysis ( $\text{FoV} = 1.1 \times 2.2$ ) and the residual arrays are used for absolute brightness measurements using linear-variable filter (LVF). With  $\sim 3$  AB magnitude higher detectivity than the CIBER-1, the CIBER-2 measurement will confirm the CIBER-1 result and probes the fluctuation and absolute brightness measurements in visible bands.

On the other hand, MIRIS is already mission completed Korea satellite. It performed pointing observations in NEP region with  $\text{FoV}$  of  $3.67^\circ \times 3.67^\circ$ . Since there is a gap between the CIBER and the IRTS in fluctuation measurements, the MIRIS is expected to cover the power spectrum in that angular scales which will connects the CIBER and the IRTS power spectra.

Lastly, SPHEREx will make a crucial role to understand the NIREBL origins. SPHEREx is designed to perform an all sky spectral survey with spectral coverage from  $0.75$  to  $4.8 \mu\text{m}$ . While the SPEHREx will map the whole sky four times for 2 years of mission period, North and South ecliptic poles (deep survey fields) will be observed more than 100 times. The deep survey fields will cover approximately a total area of  $200 \text{ deg}^2$ , which will enable us to probe the spatial fluctuation from sub-degree to degree scales. Due to the wide spectral coverage of SPHEREx, we are able to determine the redshifts of individual galaxies accurately. That is, with the intensity mapping methods, we can constraint contributions from resolved galaxies as a function of redshift on the NIREBL. The SPHEREx will be proposed to medium-class explorer program. The spacecrafts of above three mission are shown in Figure 4.1.

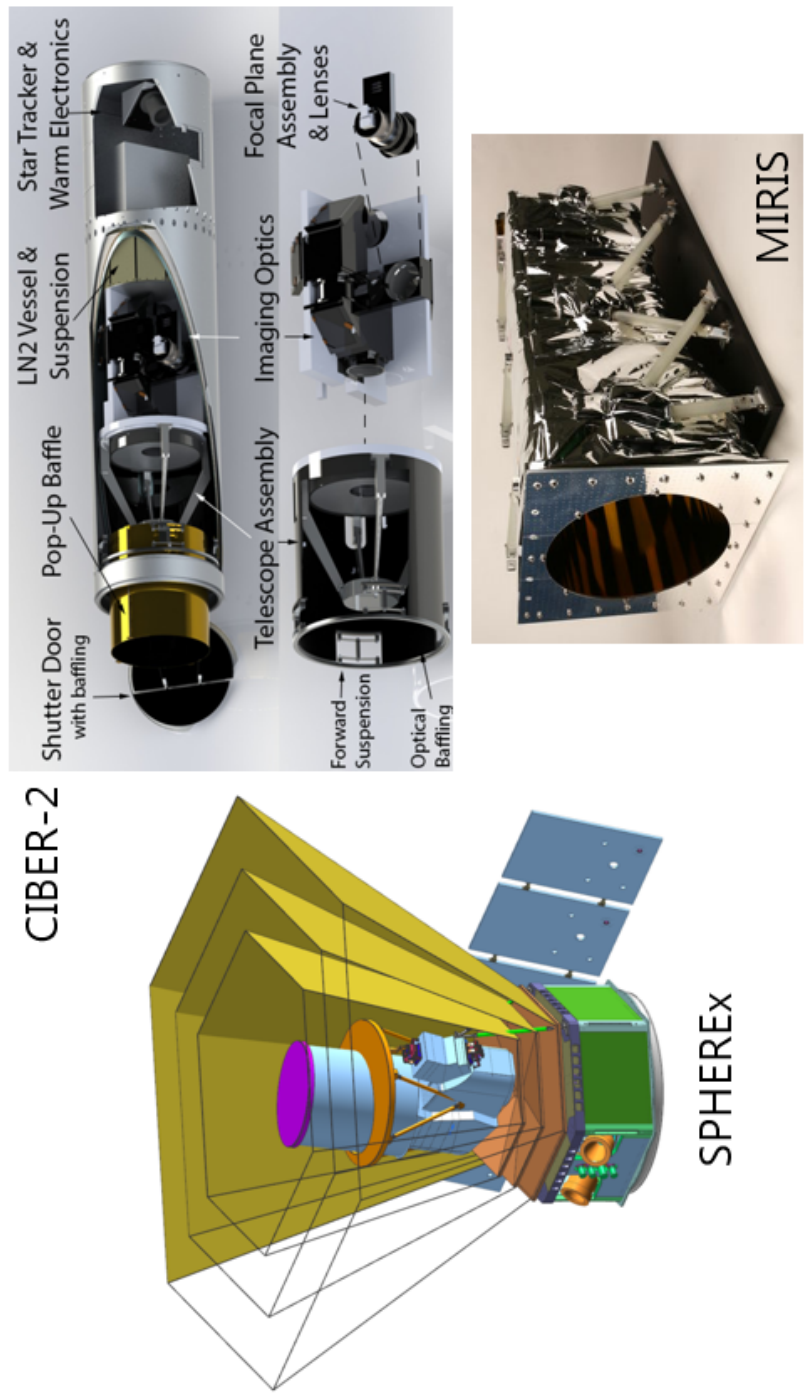


Figure 4.1 Schematic designs for the SPHEREx and the CIBER-2 and photograph for the MIRIS. The MIRIS had completed its mission in 2015 while other two are the future missions.

# Bibliography

Abdo, A., et al. 2010, J. Cosmol. Astropart. Phys. 1004, 014

Abramowski et al. 2013, A&A, 550, 4

Ackermann, M., et al. 2015, ApJ, 799, 86

Ajello, M., et al. 2008, ApJ, 689, 666

Arai, T., et al. 2015, ApJ, 806, 69

Becker, R. H., et al. 2001, AJ, 122, 2850

Bernstein, R.A., 2007, ApJ, 666, 663

Bock, J., et al. 2006, New A Rev., 50, 215

Bock, J., et al. 2013, ApJS, 207, 32

Bohlin, R. C., & Gilliland, R. L., 2004, AJ, 127, 3508 (BG)

Bond, J. R., et al. 1998, Phys. Rev. D, 57, 2117

Bouwens, R. J., et al. 2012, ApJ, 754, 83

Brandt, T. D., & Draine, B. T., 2012, ApJ, 744, 129

Bromm, V. & Loeb, A., 2002, ApJ, 575, 111

- Bromm, V. & Loeb, A., 2003, *ApJ*, 596, 34
- Brown, S. W., 2006, *ApOpt*, 45, 8218
- Calabretta, M. R. & Greisen, E. W., 2002, *A&A* 395, 1077
- Cambresy, L., et al. 2001, *ApJ*, 555, 563
- Chary, R., et al. 2008, *ApJ*, 681, 53
- Chon, G., et al. 2004, *MNRAS*, 350, 914
- Cohen, M., et al. 2003, *AJ*, 126, 1090
- Cooray, A. et al. 2007, *ApJ*, 659, L91
- Cooray, A., et al. 2012, *Nature*, 490, 514
- Dole, H., et al. 2006, *A&A*, 451, 417
- Dominguez, A., et al. 2011, *MNRAS*, 410, 2556
- Driver, S. P., et al. 2016, *ApJ*, 827, 108
- Dwek, E., et al. 2005, *ApJ*, 635, 784
- Dwek, E. & Krennrich, F., 2013, *Astroparticle Physics* 43, 112
- Fan, X. et al. 2001, *AJ*, 122, 2833
- Girardi, L., et al. 2005, *A&A*, 895, 915
- Gorjian, E. L., et al. 2000, *ApJ*, 536, 550
- Gorski, K. M. et al. 2005, *ApJ*, 622, 759
- Hasinger, G., 2004, *NuPhS*, 132, 86

- Hauser, M. G., et al. 1998, *ApJ*, 508, 25
- Hauser, M.G. & Dwek, E., 2001, *ARA&A*, 39, 249
- H.E.S.S. Collaboration 2013, *A&A*, 550, A4
- Hivon, E., et al. 2002, *ApJ*, 567, 2
- Kashlinsky, A., et al. 1996, *ApJ*, 470, 681
- Kashlinsky, A., et al. 2005, *Nature*, 438, 45
- Kashlinsky, A., et al. 2007, *ApJ*, 654, L5
- Kashlinsky, A., et al. 2012, *ApJ*, 753, 63
- Keenan, R. C., et al. *ApJ*, 723, 40
- Kelsall, T., et al. 1998, *ApJ*, 508, 44
- Kim et al. 2017, *AJ*, 153, 84K
- Korngut, P. M., et al. 2013, *ApJS*, 207, 34
- Lee, D. H., et al. 2010, *Journal of Astronomy and Space Sciences*, 27, 401
- Leinert, Ch. et al. 1998, *A&AS*, 127, 1L
- Levenson, L. R., et al. 2007, *ApJ*, 666, 34
- Madau, P. & Pozzetti, L., 2000, *MNRAS*, 312, L9-L15
- Madau, P., & Silk, J. 2005, *MNRAS*, 359, L37
- Matsumoto, T., et al. 2005, *ApJ*, 626, 31
- Matsumoto, T., et al. 2011, *ApJ*, 742, 124

- Matsumoto, T., et al. 2015, ApJ, 807, 57
- Matsuoka, Y., 2011, ApJ, 736, 119
- Matsuura, S., et al. 1994, PASP, 106, 770
- Matsuura, M., et al. 1999, A&A, 348, 579
- Matsuura, S., et al. 2016, ApJ submitted
- Mattila, K., et al. 2011, Proceedings IAU Symposium No. 284, 429
- Maurer, A., et al. 2012, ApJ, 745, 166
- Murakami, H., et al. 1996, PASJ, 48, L41
- Murakami, H., et al. 2003, ESA SP-481, 431
- Natarajan, A. & Yoshida, N., Progress of Theoretical and Experimental Physics, V.2014, Issue 6
- Noda, M., et al. 1992, ApJ, 391, 456
- Matsumoto, T., et al. 1988, ApJ, 332, 575
- Noda, M., et al. 1996, SPIE 2817, 248
- Onaka, T., et al. 1994, Appl. Opt. 33, 1880
- Petri, A., et al. 2012, MNRAS, 422, 1690
- Planck Collaboration I, Planck 2015 results. I. Overview of products and results. 2016,
- Purcell, C. W., et al. 2007, ApJ, 666, 20
- Pyo, J. H., et al. 2012, ApJ, 760, 102

- Rayner, J. T. 2009, *ApJS*, 185, 289
- Salvaterra, R. & Ferrara A. 2003, *MNRAS*, 339, 973
- Sano, K, et al. 2015, *ApJ*, 811, 77
- Sano, K, et al. 2016, *ApJ*, 818, 72
- Santos, M. R., et al. 2002, *MNRAS*, 336, 1082
- Schlegel, D. J., 1998, *ApJ*, 500, 525
- Seo, H. J., et al. 2014, *ApJ*, 807, 140
- Seigal-Gaskins, J. M., et al. 2010, *MNRAS*, 415, 1074S
- Skrutskie, M. F., et al. 2006, *AJ*, 131, 1163S
- Tegmark, M., 1997, *ApJ*, 480, L87
- Thompson, R. I., et al. 2007, *ApJ*, 666, 658
- Tsuji, T. 2015, *A&A*, 67, 26
- Tsumura, K., et al. 2010, *ApJ*, 719, 394
- Tsumura, K., et al. 2013, *ApJS*, 207, 33
- Viero, M. P., et al. 2015, *ApJL*, 809, L22
- Wainscoat, R., 1992, *ApJS*, 83, 111
- Wright, E. L. & Reese, E. D. 2000, *ApJ*, 545, 43
- Wright, E. L. 2001, *Proc. IAU Symposium*, 204, 157
- Yuan, H. B., Liu, X. W., & Xiang, M. S. 2013, *MNRAS*, 430, 2188



Yue, B., et al., 2013, MNRAS, 431, 383

Zemcov, M., et al. 2013, ApJS, 207, 31

Zemcov, M., et al. 2014, Science 346, 732

Zibetti, S., 2005, MNRAS, 358, 949

Zubko, V., et al. ApJS, 152, 211

## Appendix A

# Reflectivity measurements

When designing an optical system, especially for the space-borne satellites' parts, stray light is one of the most important factor have to be reduced to detect only the desired signal with high signal to noise performance. There can be a leakage in the enclosed system, reflection and scattering from a mirror or inside structures, and thermal emission of system itself as well as particulates or outgassing phenomena. Although it is very hard to get rid of causes, we can reduce the stray light by using materials having low reflectance inside an optical system. Ideally, black material absorbs all incident light. However, they reflect light to a greater or lesser degree depending on their physical properties. One reliable explanation for the different properties of various kinds of black materials is the surface roughness where more various features can be seen if one uses Scanning Electron Micrograph (SEM). Also, we can estimate the reflectance by shining the light on a material in the visible wavelength regime by eye inspection. However, it becomes hard to judge in the infrared wavelength regime without a measuring tool. Here, we introduce the reflectivity of various black materials measured at laboratory in near-infrared.

We measured reflectivities of black materials using monochromator after white light source. The monochromator is optimized for the near infrared from 0.7 to 2.1

$\mu\text{m}$  with grating. As shown in the schematic diagram of Fig. 2, the monochromatic light pass through an 82 Hz chopper synchronized with a lock-in amplifier to eliminate other frequencies treated as noise. This chopped light is reflected into a test sample with the incident angle of  $45^\circ$  and enter a single chip detector made of Indium Antimonide (InSb). The  $45^\circ$  was selected since it is the most optimized angle to arrange the position of each instrument without disturbing each other as well as minimizing the stray light via scattering event. Also, we enclosed the system with black plate to block the randomly existent stray light which is invisible to human eye in the infrared wavelength regime. To compute the reflectances and compare them with each other, we also measured the reference light reflected from the flat mirror. Finally, the reflectance of a black material at every 20 nm wavelength step is calculated by dividing the value measured from the black material with that from the flat mirror. The position of a test sample was close enough to the monochromatic light for the high signal to noise ratio by gathering the amount of light as much as possible.

We obtained amplified signals with reasonable signal to noise ratio via lock-in amplifier for the each test sample shown in Fig. 1. As shown in a schematic diagram of Fig. 2, detected signal goes into lock-ins and is amplified by manually set gain which ranges from mA to pA. Tested materials presented in this paper have been done with pA gain set to filter out reasonable signal level from noise while flat mirror was enough with mA gain. Since the gain levels are different between the mirror and other test samples, normalization factor to the pA level has been multiplied for each result. Then, we divided the result of the test samples with that of the mirror to calculate their reflectivities as described in equation A.1.

$$Reflectance = \frac{B_{sample}}{B_{mirror}}, \quad (\text{A.1})$$

Here,  $B_{sample}$  is the reflected signal of a test sample, and  $B_{mirror}$  is that of the

flat mirror for the reference. If reflecting performance of a test sample is same as the flat mirror, their ratio would show just unity. On the other hand, reflectance gets lower if a black material absorbs more lights compared with the result from the flat mirror. Figure A.1 shows the result reflectance of all the test samples. They shows flat spectrum over whole wavelength ranges. The laserblack shows distinctly low reflectivity comparable with velvet. Between the two, laserblack is chosen for the baffle coatings due to the ragged surface of velvet black.

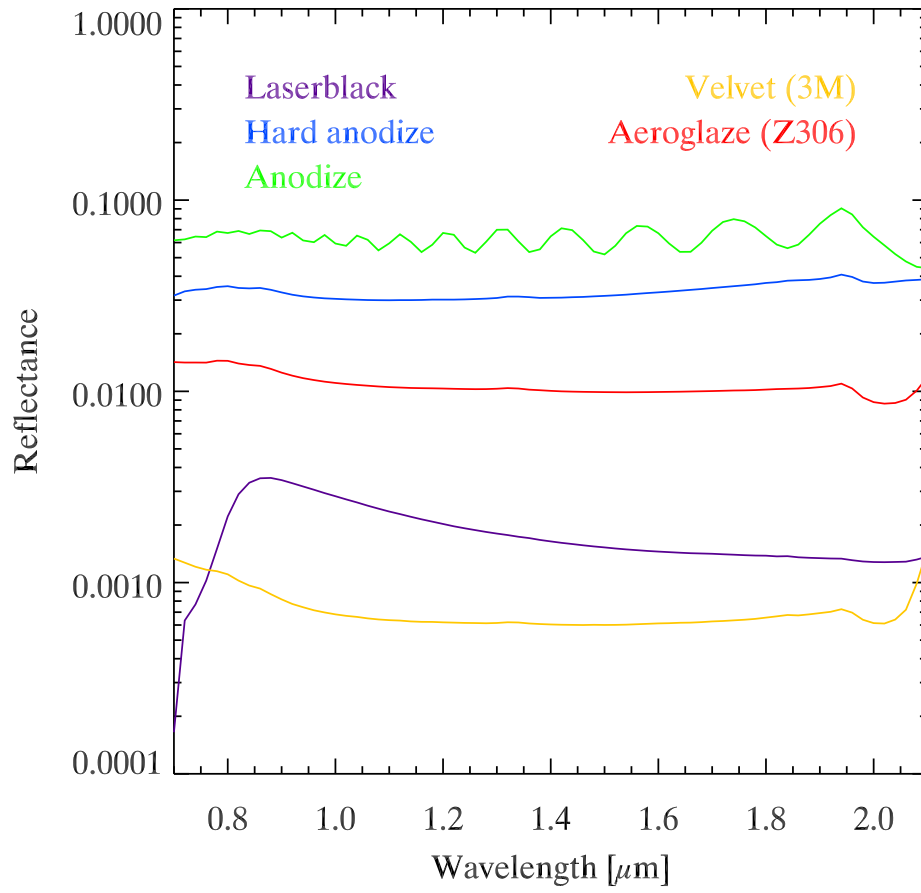


Figure A.1 Reflectance measurements of various kinds black materials. Each sample is drawn with each color. The unity in vertical axis indicates the perfect reflection.

## 요 약

우주배경복사는 관측적 한계 또는 복사를 만드는 물리적 기작의 특성으로 인해 개별로 인식되지 않고 우주 전 하늘에 대해서 균일하게 퍼져있는 빛을 말한다. 모든 파장에 대해 우주배경복사를 관측할 수 있는데, 파장별로 복사를 내는 기작이 구별되어진다. 본 논문은 근적외선에서 우주배경복사를 관측하고 이를 분석해 우주배경복사(이하 근적외배경복사)의 기원과 그 물리적 기작에 대해 연구한 결과이다.

근적외배경복사는 별의 핵융합 과정이나 블랙홀로 주변 물질들이 빨려들어 갈 때 방출되는 것으로 알려져 있다. 하지만 관측적 한계로 인하여 근적외배경복사의 기원과 밝기분포등은 제대로 알려져 있지 않다. 현재 외부은하만이 그 기원으로 알려져 있는데 이들은 근적외배경복사 밝기에 최대 약 20 % 정도만을 차지하므로 나머지 80 %의 에너지를 밝히는 것이 이 연구의 최종 목표이다.

근적외배경복사의 밝기는 우리은하와 지구대기에서의 밝기보다 어둡기 때문에 지구 대기를 벗어나 관측하는 것이 유리하다. 따라서 사운딩로켓이나 인공위성에 망원경을 실어 우주에서 관측을 수행하며 고감도의 검출기가 필요하고 오랜 시간의 노출이 요구되어진다. 이렇게 관측된 밝기에서 기원이 알려지지 않은 근적외배경복사의 영향만을 추출하려면 우리 은하와 외부 은하의 빛을 제거해야 한다. 우리은하의 전경원에는 태양빛이 태양계에 분포하고 있는 먼지 입자들에 의해 산란되어 보이는 황도광, 성간 물질에 의해 산란된 별빛, 우리 은하에 분포하는 별빛이 있다. 이러한 관측적 한계에도 불구하고 근적외배경복사를 관측하기 위한 시도들이 이루어져왔다.

초기 COBE/DIRBE, IRTS/NIRS 망원경을 이용한 근적외배경복사 밝기는 관측과 이론으로 추산된 외부은하의 총 밝기보다 약 2배에서 8배까지 밝았다. 이후에 AKARI/IRC, HST/NICMOS 등의 우주망원경으로  $0.5\mu\text{m}$  부터  $4.0\mu\text{m}$ 까지의 파장대역에서 근적외배경복사의 밝기를 성공적으로 측정하였다. 또한, 공간적인 밝기분포 정보를 담은 공간요동 연구도 수행되어졌고 근적외배경복사의 존재를 뚜렷하게 확인할 수 있었다. 하지만 기존연구에서  $1\mu\text{m}$  근처의 절대밝기 관측이 이루어지지 않았고, 또 1도 보다 큰 각도스케일에서의 공간요동 연구가 미흡했다. 우리는 위의 두 가지 측면에서 근적외배경복사의 관측과 연구를 수행하였다. 첫째로 절대밝기 연구를 위해서 우리는

미국, 일본과 협력하여 CIBER 사운드로켓을 제작 및 발사했다. 로켓에는 총 4대의 망원경이 실렸는데, 모두 근적외배경복사 관측을 목표로 한 것이다. 2009년부터 2013년까지 총 4번에 걸친 발사관측이 이루어졌고,  $1\mu\text{m}$  근처에서의 절대밝기 연구를 위해 저분산분광기(LRS)가 사용되었다. 하지만 마지막 4번째 발사에서 얻어진 데이터의 처리과정에서 절대밝기 변환에 문제가 있음을 알게 되었다. 절대밝기 동정은 발사전 실험실에서 수행했으므로 이미 관측이 끝나 망원경을 회수할 수 없는 상황에서 재측정은 불가능했다. 우리는 LRS에서 관측된 우리은하 내 밝은 별들을 측광하였고 이들 밝기와 다른 연구를 통해 알려진 밝기를 비교해 절대밝기를 검증할 수 있었다. 이 과정에서 총 105개의 우리은하 내 밝은 별들을 측광하였고 개개 별들에 대한 근적외스펙트럼을 얻을 수 있었다. 이 결과는 근적외선에서의 별의 기작 연구에 기여할 것으로 기대된다. 한편, 별의 밝기 비교를 통하여 우리는 3번째 발사에서 얻었던 절대밝기 동정결과를 4번째 발사의 데이터를 계측하는데 사용할 수 있었고, 최종적으로  $0.8\mu\text{m}$  부터  $1.7\mu\text{m}$  사이에서 근적외배경복사의 절대밝기를 성공적으로 측정하였다.

CIBER로켓에 실린 또 다른 두 대의 망원경은 이미징 카메라(Imager)로 각각 I와 H 밴드 필터가 장착되어 있다.  $2^\circ \times 2^\circ$ 의 넓은 시야를 가지고 있는 이들 망원경을 이용하여 근적외배경복사의 공간요동 관측을 수행하였다. 연구 결과 각도스케일 1도 이하에서 기존의 다른 연구들과 같이 근적외배경복사에 의한 공간요동을 보였다. 또한, 각도 스케일이 커짐에 따라 요동의 크기도 커지는 것으로 관측되었는데, 우리는 이것에 주목하여 더 큰 각도스케일 ( $> 1^\circ$ )에서 공간요동이 어떤 양상을 보일지에 대해 연구하였다. 본 연구를 위해 우리는 IRTS/NIRS 데이터를 사용하였고 2도부터 20도 사이의 공간요동을 얻을 수 있었다. 기존의 다른 연구와 비교한 결과 근적외배경복사의 공간요동이 약 1도 부근에서 가장 크게 나타났고 그보다 더 큰 스케일에서는 일정하게 감소한다는 것을 밝혔다. 이 결과는 기존 연구에서 예측하지 못한 것으로 추후 더 다양한 파장과 각도스케일에서의 관측연구뿐만 아니라 근적외배경원을 설명하기 위한 새로운 모델의 필요성을 시사한다.

**주요어:** 우주 배경 복사 — 적외선: 확산 배경 — 적외선 자료 처리 — 방법: 분광분석

**학 번:** 2011-30127

